Title
Ion Probe Measurements of Comet Dust: Investigating Oxygen Isotope Heterogeneity in the Solar System

Author
Snead, Christopher Jorge

Publication Date
2016

Peer reviewed|Thesis/dissertation

UNIVERSITY OF CALIFORNIA

Los Angeles

Ion Probe Measurements of Comet Dust: Investigating Oxygen Isotope Heterogeneity in the Solar System

A dissertation in partial satisfaction of the

requirements of the degree of Doctor of Philosophy

in Geochemistry

by

Christopher Jorge Snead

2016

ABSTRACT OF THE DISSERTATION

Ion Probe Measurements of Comet Dust: Investigating

Oxygen Isotope Heterogeneity in the Solar System

by

Christopher Jorge Snead

Doctor of Philosophy in Geochemistry

University of California, Los Angeles, 2016

Professor Kevin D. McKeegan, Chair

The abundances of the stable isotopes of oxygen vary in terrestrial materials in ways that can be explained by mass-dependent fractionation. Refractory inclusions and chondrules in meteorites, however, have oxygen isotopic compositions that are suggestive of a mixing between isotopically separated reservoirs. Understanding the processes that produced ^{16}O-rich and ^{17,18}O-rich reservoirs has been a major objective of cosmochemical research for several decades. One complication of investigations into the nature of oxygen isotope heterogeneity has been the alteration of chondritic components on asteroidal parent bodies, which modify the original isotopic signatures of primordial dust. Comets accreted in distal cold regions of the solar nebula, and dust from comets probably experienced minimal parent body processing relative to

asteroidal samples. Much of the dust collected in the stratosphere likely has cometary origins, but until the return of samples from NASA's Stardust spacecraft, definitive links to comets had not been established. Stardust successfully returned particles from a known comet 81P/Wild 2, but the silica aerogel collectors severely altered the oxygen isotope compositions of the fine-grained dust component. Impacts of Wild 2 dust into aluminum foils produced craters that retained material as a melt residue, providing an opportunity to measure the oxygen isotopic composition of coarse and fine-grained components of comet dust.

This dissertation describes oxygen isotope measurements of Wild 2 impact crater residues via Secondary Ion Mass Spectrometry (SIMS). Hypervelocity experiments that simulated the collection conditions of Wild 2 dust were preformed using minerals of known oxygen isotope composition; the resulting craters were used to develop analytical techniques, to assess modification to the oxygen isotope composition due to hypervelocity capture, and as standards for oxygen isotope measurements of Wild 2 craters. This dissertation also describes the oxygen isotope measurements of interplanetary dust particles with hydrated mineralogy, in an attempt to observe ^{17,18}O-enriched water that is predicted to be a consequence of some proposed mechanisms for producing observed oxygen isotope heterogeneity. Relationships between interplanetary dust particles, comet dust, and carbonaceous chondrites are examined, and implications for models of comet formation and oxygen isotope heterogeneity are discussed.

The dissertation of Christopher Jorge Snead is approved.

David Clifford Jewitt

Edward Donald Young

James E. Larkin

Kevin D. McKeegan, Committee Chair

University of California, Los Angeles,

2016

Table of Contents

List of Figures

List of Tables

Acknowledgments

The work of this dissertation would not have been possible without the samples provided by NASA Johnson Space Center's Astromaterials Curation Facility, or the foil crater standards provided by Anton Kearsley at the Natural History Museum. Mark Burchell was extremely generous with his expertise and use of the light gas gun facility at the University of Kent at Canterbury.

Rita Economos and Ming-Chang Liu were extremely helpful with tuning and operation of the IMS-1270 for the analyses reported in this study, and Veronica Heber offered invaluable guidance and encouragement, especially with the hydrated IDP project. Patrick Boehnke's expertise with statistical analysis greatly contributed to the interpretation of results.

Much of the work of this dissertation is the product of collaboration with Lindsay Keller and Scott Messenger, whose expertise with transmission electron microscopy and NanoSIMS analyses contributed immensely to the success of the work reported in this dissertation. I am especially grateful to Lindsay Keller for stimulating many ideas and directions of research, and for mentoring me for the years preceding and during my graduate studies, and to Scott Messenger and Keiko Nakamura-Messenger for offering invaluable advice and encouragement, as well as the use of their cosmic dust facilities.

Andrew Westphal has been amongst the most influential of mentors of my academic development. My involvement with Stardust began as a research project in Andrew's laboratory

seventeen years ago, and he has guided and encouraged me as teacher and advisor since my undergraduate years. I am immensely grateful for his years of counsel and guidance.

I would like to acknowledge my extreme gratitude to my committee members, who have been outstanding resources of knowledge pertaining to my dissertation research as well as my development as an educator. The opportunity to participate in an observing session at Keck Telescope with David Jewitt was a highlight of my graduate career. Dave Jewitt and James Larkin have been extraordinary educational mentors who have helped me to grow as an effective communicator of science to the public. Ed Young has been a perpetually enthusiastic resource of knowledge about early solar system processes and oxygen isotope heterogeneity.

Finally, I would like to express my gratitude to my advisor and committee chair, Kevin McKeegan, for his dedication, expertise, encouragement and enduring support of my research and education over the years. His commitment to my education and research has made the success of this dissertation research a reality I could not have personally imagined.

CHRISTOPHER SNEAD

EDUCATION

2003	B.A., Physics, University of California at Berkeley, Berkeley, CA.
2010	M.A, Geochemistry, University of California Los Angeles, Los Angeles, CA.
2016	C.Ph, Geochemistry, University of California Los Angeles, Los Angeles, CA.

RESEARCH AND TEACHING EXPERIENCE

2016	Teaching Fellow, Office of Instructional Development, U.C.L.A.
2007-present	Graduate Student researcher, Dept. of Earth Planetary and Space Sciences, U.C.L.A.
2008, 2012-2013	Graduate Student Instructor, Dept. of Earth and Space Sciences, U.C.L.A.
July 2004-2007	**Staff Research Assistant**, Space Sciences Laboratory, U.C. Berkeley. Involved in the extraction and analysis of cometary particles from the Stardust collector.
August 2003-July 2004	**Junior Specialist**, Space Sciences Laboratory, U.C. Berkeley. Developed techniques for the extraction and analysis of extraterrestrial particles captured in aerogel, including the use of MEMS devices and micromanipulation techniques.
January 2001-August 2003	**Laboratory Assistant**, Space Sciences Laboratory, U.C. Berkeley.

AWARDS

October 2013	Academic Senate Committee Distinguished Teaching Assistant Award
September 2012	Department of Earth and Space Sciences Excellence in Teaching Award

SELECTED PUBLICATIONS

1. Snead, C.J., et al., *Oxygen Isotope Measurements of Simulated Wild 2 Impact Crater Residues.* Meteoritics & Planetary Science, 2011. **46**: p. A217-A217.
2. Joswiak, D.J., et al., *Kosmochloric Ca-rich pyroxenes and FeO-rich olivines (Kool grains) and associated phases in Stardust tracks and chondritic porous interplanetary dust particles: Possible precursors to FeO-rich type II chondrules in ordinary chondrites.* Meteoritics & Planetary Science, 2009. **44**(10): p. 1561-1588.
3. Stephan, T., et al., *TOF-SIMS analysis of cometary matter in Stardust aerogel tracks.* Meteoritics & Planetary Science, 2008. **43**(1-2): p. 233-246.
4. Marty, B., et al., *Helium and neon abundances and compositions in cometary matter.* Science, 2008. **319**(5859): p. 75-78.
5. Graham, G.A., et al., *Applied focused ion beam techniques for sample preparation of astromaterials for integrated nanoanalysis.* Meteoritics & Planetary Science, 2008. **43**(3): p. 561-569.
6. Westphal, A.J., et al., *Synchrotron-based organics and mineralogical survey of three stardust tracks.* Meteoritics & Planetary Science, 2007. **42**: p. A163-A163.
7. Brownlee, D., et al., *Comet 81P/Wild 2 under a microscope.* Science, 2006. **314**(5806): p. 1711-1716.
8. McKeegan, K.D., et al., *Isotopic Compositions of Cometary Matter Returned by Stardust.* Science, 2006. **314**(5806): p. 1724-1728.
9. Zolensky, M.E., et al., *Report - Mineralogy and petrology of comet 81P/Wild 2 nucleus samples.* Science, 2006. **314**(5806): p. 1735-1739.
10. Flynn, G.J., et al., *Elemental compositions of comet 81P/Wild 2 samples collected by Stardust.* Science, 2006. **314**(5806): p. 1731-1735.
11. Borg, J., et al., *Synchrotron X-rays in situ analysis of extraterrestrial grains trapped in aerogel.* Advances in Space Research, 2006. **38**(9): p. 2068-2074.
12. Ishii, H.A., et al., *Rapid extraction of dust impact tracks from silica aerogel by ultrasonic microblades.* Meteoritics & Planetary Science, 2005. **40**(11): p. 1741-1747.
13. Westphal, A.J., et al., *Aerogel keystones: Extraction of complete hypervelocity impact events from aerogel collectors.* Meteoritics & Planetary Science, 2004. **39**(8): p. 1375-1386.
14. Westphal, A.J., et al., *Small hypervelocity particles captured in aerogel collectors: Location, extraction, handling and storage.* Meteoritics & Planetary Science, 2002. **37**(6): p. 855-865.

Chapter 1: Introduction

Formation of the Solar System:

The solar system began ~4.6 billion years ago with the gravitational collapse of a dense molecular cloud core of gas and dust. The contraction of this cloud core compressed and heated hydrogen gas until nuclear fusion of hydrogen into helium provided photon pressure that hydrostatically balanced further gravitational compression. The newly formed Sun was enshrouded in a disk of residual gas and dust called the solar nebula; it is from this nebula that the planets would eventually form. Understanding the nature of this primordial environment may provide important insights into terrestrial and giant planet formation and perhaps the conditions under which life arose. Petrographic and geochemical examination of chondritic meteorites originating from asteroidal parent bodies has provided a wealth of information about the chronology of early solar nebula processes (Davis and McKeegan 2014), initial elemental abundances (Lodders 2003), and the evolution of solid material in the protoplanetary disk (Ciesla and Charnley 2006). Cosmic dust collected in the Earth's stratosphere and micrometeorites recovered from Antarctic ices may derive from parent bodies not represented in meteorite collections, and have become increasingly important resources for understanding protoplanetary and protosolar environments - especially as microanalytical techniques have improved.

Oxygen in the Solar System:

Oxygen is the most abundant chemical element in the Earth's crust, and the third most abundant

element (after hydrogen and helium) in the solar system. It is a major constituent of most oxides, silicates, carbonates, phosphates and sulfates; due to oxygen's large ionic radius, many minerals can be thought of as lattices of close packed oxygen spheres, with the other elements located at interstitial sites within the close-packed lattices. Three stable isotopes of oxygen exist as a result of differing nucleosynthetic processes that occur in stellar envelopes of stars. The most abundant of these isotopes is ^{16}O (~99.76%) followed by ^{18}O (~0.20%) and ^{17}O (~0.04%). Differences in oxygen isotope abundances are measured relative to a standard and expressed in delta notation, where:

$$\delta^{18}O = \left[\frac{\left(\frac{^{18}O}{^{16}O}\right)_{sample}}{\left(\frac{^{18}O}{^{16}O}\right)_{SMOW}} - 1 \right] \times 1000$$

$$\delta^{17}O = \left[\frac{\left(\frac{^{17}O}{^{16}O}\right)_{sample}}{\left(\frac{^{17}O}{^{16}O}\right)_{SMOW}} - 1 \right] \times 1000$$

in units of per mil (‰). SMOW is Standard Mean Ocean Water and the reference upon which most O-isotopes are compared.

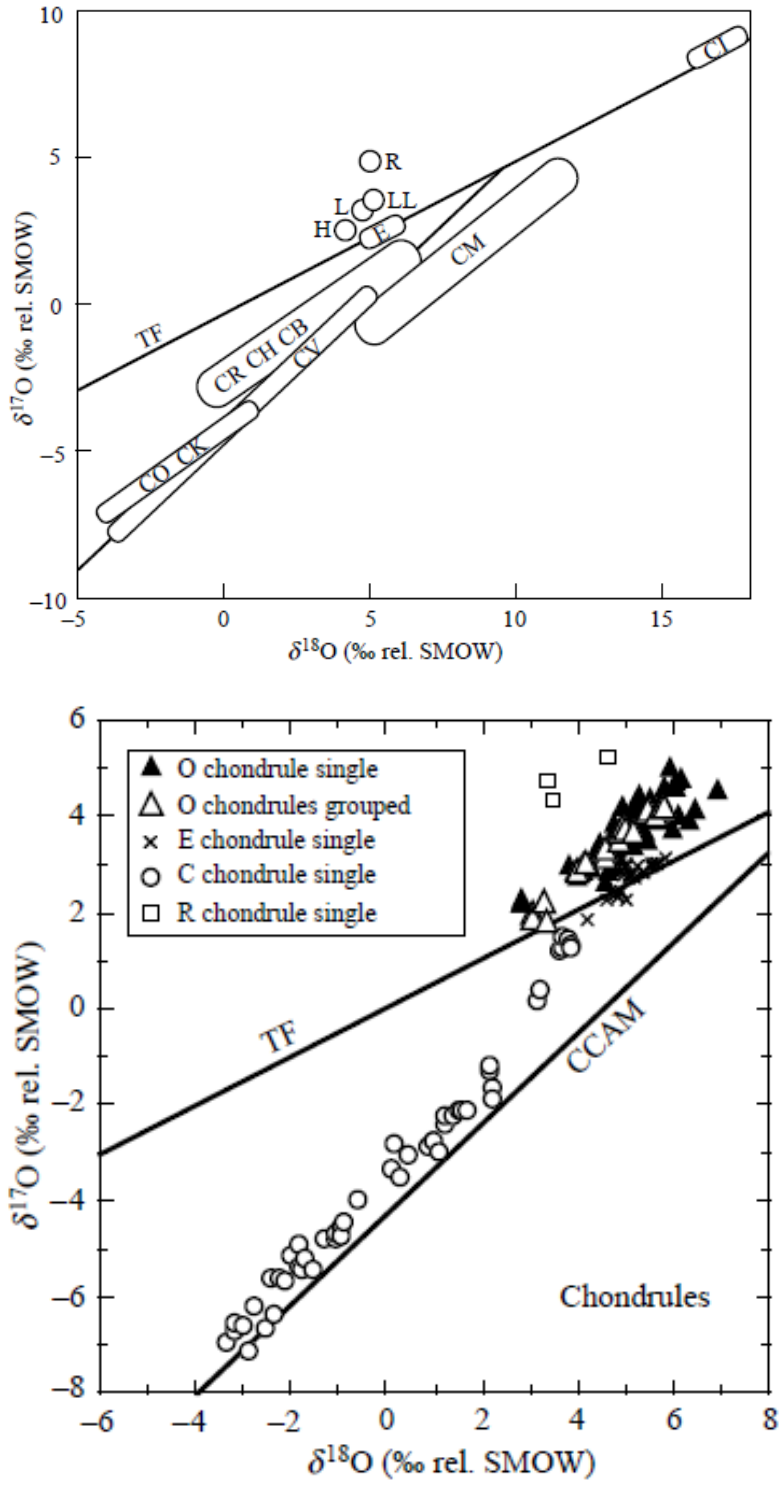

Figure 1.1: Oxygen isotopic compositions of chondrite groups and of individual chondrite components. Terrestrial Fractionation (TF) and Carbonaceous Chondrite Anhydrous Mixing (CCAM) lines are shown for reference (Clayton 1993).

Oxygen Isotope Fractionation:

Because of mass differences between the three stable oxygen isotopes, oxygen isotopologues can have slightly different kinetic and/or bonding properties that cause a mass-dependent fractionation. The nature of this mass-dependent fractionation is such that most materials subject to this process lie on a mass fractionation line with a slope of 0.52 (for terrestrial materials) when plotted on a graph of $\delta^{17}O$ vs. $\delta^{18}O$ (figure 1.1).

Oxygen Isotope Compositions of the meteorites and the Sun:

In contrast to terrestrial materials, meteorites have oxygen isotope compositions that diverge from the terrestrial fractionation (TF) line. The chondrite groups have distinctive oxygen isotope compositions, with the exception of the CO, CK and CV groups which overlap somewhat (Clayton 1993; Clayton, Grossman, and Mayeda 1973). The main sources of these discrete values include variations in oxygen isotope compositions and abundances of chondrules, parent body processing of the chondrites, and variations of the O-isotope composition of the matrix. Understanding how each of these factors contributes to bulk oxygen isotope values of chondrites can provide some insight into the environments in which they formed. Examination of refractory components within meteorites reveals that Calcium Aluminum-rich Inclusions (CAIs) fall along a line with a slope closer to 1, referred to as the Carbonaceous Chondrite Anhydrous Minerals (CCAM) line. This line has been interpreted as representing mixing between a ^{16}O-rich reservoir and a ^{16}O-poor reservoir. How such reservoirs arose and were maintained in the early solar system has been the subject of debate for decades.

Proposed Sources of Oxygen Isotope Heterogeneity in the Solar System:

Initially, nearby supernova injection of material into the early solar nebula was suggested as a way to generate the oxygen isotope heterogeneities preserved in the meteorite record (Clayton, Grossman, and Mayeda 1973; Clayton and Mayeda 1977). In this scenario, the solar dust and gas were well-homogenized and assumed to be near terrestrial values, and a nearby supernova (perhaps resulting from a massive star formed from the same dense molecular cloud as the Sun) polluted the early solar nebula with ^{16}O-rich material. However, such excesses were not found to correlate with similar excesses in other light isotope rock forming elements associated with oxygen, such as Si and Mg in fluorination experiments of CAIs (Fahey et al. 1987). Galactic Chemical Evolution (GCE) has also been proposed to explain oxygen isotope heterogeneity (Timmes, Woosley, and Weaver 1995). Primary isotopes such as ^{16}O are produced in early generations of stars composed of H and He only (i.e. low metallicity stars); secondary isotopes can only be produced if pre-existing primary isotopes are present (e.g. proton capture by ^{16}O during hydrogen burning to produce ^{17}O). GCE results in a linear increase of ^{16}O and an exponential increase of ^{17}O and ^{18}O over time (Clayton 1988; Meyer et al. 2008). Some ^{16}O produced in earlier generations of low-metallicity stars can be temporarily sequestered in dust leading to an oxygen reservoir distinct from the gas in the dense molecular cloud from which the sun formed. This scenario predicts a ^{16}O-rich composition for the dust and a ^{16}O-poor composition for the sun. This prediction is inconsistent with measurements of solar wind returned by NASA's Genesis mission (McKeegan et al. 2011).

Mass-independent chemical fractionation of ozone has been used to explain anomalous oxygen fractionation in the Earth's stratosphere (Thiemens and Heidenreich 1983), and similar

effects have been suggested as a potential source of the oxygen isotope heterogeneity of the solar system (Thiemens 1992; Thiemens 1996). Ozone forms by the dissociation of O_2 to form atomic oxygen, which then reacts with an O_2 molecule to form a vibrationally excited O_3 molecule:

$$O + O_2 \leftrightarrow O_3^*$$

The O_3 dissociates back to O_2 and O unless vibrational energy is removed by a nonreactive collision with some other molecule M:

$$O_3^* + M \rightarrow O_3$$

In isotopologues of O_3 where the location of the heavy isotope results in an asymmetrical mass distribution, the vibrational energy can be redistributed throughout the molecule via a greater number of available vibrational and rotational states, resulting in a longer mean lifetime for such species, and as a result more opportunities for stabilizing collisions. The resulting effect is an equal enrichment in ^{17}O and ^{18}O in ozone. This symmetry-dependent fractionation effect is not necessarily restricted to ozone, and could be relevant in other triatomic molecules as well (e.g. SiO_2). It has been proposed that similar effects for SiO_2 are the source for the enrichment of ^{17}O and ^{18}O in planetary materials relative to the Sun. These processes would occur at sufficiently high temperatures that SiO gas would be stable. This mechanism does not address how reservoirs would be spatially separated in such a way as to explain the difference between solar and planetary oxygen compositions; and unlike ozone, dissociation experiments for the relevant reactions have not yet been conducted to measure the $^{17}O/^{18}O$ resulting from SiO_2-SiO reactions.

Isotope-specific photodissociation of the CO molecule (i.e CO self-shielding) has been suggested as a mechanism for producing a non-mass dependent enrichment of ^{17}O and ^{18}O (Clayton 2002a). CO self-shielding occurs when a stellar UV source interacts with CO molecules, which absorb the light at a specific wavelength and dissociate. The slight mass differences between $C^{16}O$, $C^{17}O$ and $C^{18}O$ cause those isotopologues to dissociate at different wavelengths of UV light. Since the ^{16}O is much more abundant than ^{17}O and ^{18}O, its associated wavelength of UV is attenuated rapidly, whereas the wavelengths associated with the heavier isotopologues can travel much deeper into the CO gas reservoir. The result is a preferential enrichment of atomic ^{17}O and ^{18}O, which react with abundant hydrogen to form water ice. This process may occur in the dense molecular cloud core, with nearby young stellar objects providing the UV source (Yurimoto and Kuramoto 2004); as the cloud core collapses, the ^{16}O-poor water ice and the ^{16}O-rich CO gas are incorporated into the solar nebula, maintaining spatial and/or temporal heterogeneity. CAIs, the first solids to condense, incorporate the ^{16}O-rich value of the gaseous environment. As time passes, icy grains migrate into the disk plane and inward, where they eventually cross a snow line and evaporate, liberating their ^{17}O and ^{18}O enrichments which are incorporated into other solar system solids. Another possible site for the self-shielding mechanism is in the young solar nebula, perhaps on the disk surface (Lyons and Young 2005). In this scenario, the UV source can either be the sun in its T-Tauri phase, or another nearby young stellar object. In either case, enriched oxygen would be incorporated into solar system solids, which are constantly exchanging O-compositions with the surrounding gas due to frequent heating processes (such as chondrule forming events).

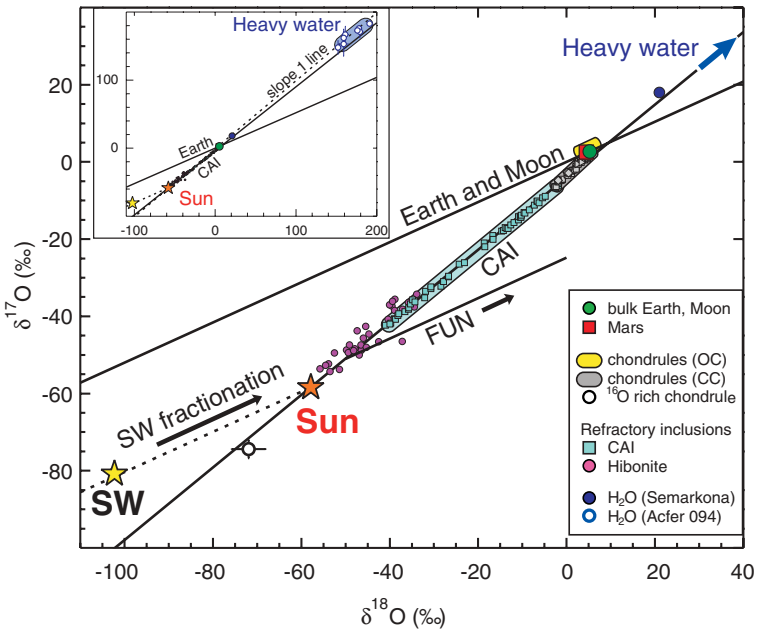

Fig. 1.2: Oxygen isotope composition of various solar system materials analyzed (McKeegan et al. 2011)

CO self-shielding models make potentially testable predictions about the oxygen isotope compositions of the Sun, primordial dust and comet ices. One such prediction is that the oxygen isotopic composition of the sun should be ~ -50‰; measurements of solar wind returned by the NASA Genesis mission are consistent with this prediction (McKeegan et al. 2011). Self-shielding models also predict comets should have a water ice composition of +50-200‰ for molecular cloud self-shielding (Yurimoto and Kuramoto 2004) and +300-1000‰ for disk irradiation self-shielding (Lyons and Young 2005). Choi inferred a value of initial H_2O of $\delta^{18}O$ = 21‰ and $\delta^{17}O$ = 17.5‰ from SIMS measurements of Semarkona magnetite, and Sakamoto reported $\delta^{17,18}O$ values of 180‰ in a poorly characterized Fe-Ni-S phase in Acfer 094 (Sakamoto et al. 2007); but to date evidence of a ^{16}O-poor reservoir remains rare. The ESA Rosetta mission made an in-situ measurement of the oxygen isotope composition of ice in comet 67P/Churyumov–Gerasimenko, with a $\delta^{18}O$ of - 102 ± 100‰ and $\delta^{17}O$ of -34 ± 235‰ (Altwegg

et al. 2015). These values do not support the self-shielding prediction, although the error bars are extremely large.

One additional self-shielding prediction is that primordial dust (i.e. dust predating solar system formation) should be on average ^{16}O-rich, indistinguishable from solar composition. Comets that accreted in the Kuiper Belt region may contain primordial dust that escaped processing during solar system formation (see below). Much of the 40,000 tons of interplanetary dust that the Earth accretes each year (Zook 2001) must have originated from active or disaggregated comets (Nesvorny and Jenniskens 2010). Chondritic Porous Interplanetary Dust Particles (CP-IDPs) collected in the stratosphere exhibit many properties that are consistent with astronomical and spacecraft observations of comets: amorphous silicate features, Mg-rich crystalline grains, high porosity, and predominantly submicron grain size (Bradley 1991; Bradley, Brownlee, and Veblen 1983). A cometary origin for CP-IDPs has also been inferred from their high concentrations (relative to meteorites) of grains identified as presolar due to their extremely large isotope anomalies (Messenger et al. 2003). Despite evidence suggestive of a cometary parent body, the precise origin of CP-IDPs remains unknown, and no samples with a definitive cometary origin were available for laboratory analyses until the return of dust from comet 81P/Wild 2 collected by the NASA Stardust mission.

Comets:

Overview

Comets are kilometer-sized bodies consisting of refractory solids, carbonaceous material and condensed gases that sublimate upon close encounter with the sun, producing a gravitationally unbound diffuse atmosphere (coma), and tails of dust and gas. The presence of condensed CO_2, CO, CH_4 and NH_3, has been interpreted as comets having accreted at temperatures below ~30K; as such, comets are thought to contain more pristine material than their asteroid counterparts, upon which significant aqueous alteration, thermal metamorphism and collisional shocks have resulted in processing of primordial components. Comets tend to derive from two regions of the solar system. Long period comets are located in a spherical cloud (Oort 1950; Weissman 1996a) 10^4-10^5 astronomical units (AU) in diameter, and are occasionally perturbed out of their orbits by nearby passing stars and fall into the inner solar system region on highly elliptical orbits with periods ≥ 200y (Weissman 1996b). Short period comets originate from the Kuiper Belt, a trans-Neptunian region of the solar system (Jewitt and Luu 1993; Luu and Jewitt 2002; Trujillo, Jewitt, and Luu 2001) that also includes the larger (≥1000 km) dwarf planets Pluto, Eris and Sedna. Kuiper Belt comets and Oort cloud comets may have accreted in similar regions of the early solar system, with the latter group being scattered via giant planet migration or other chaotic early solar system processes. Some smaller Kuiper Belt objects experience scattering from Neptune and develop very short (≤ 20y) period orbits that are gravitationally bound to Jupiter; several of these Jupiter Family Comets (JFCs) have been visited by spacecraft over the past two decades, providing detailed compositional information from in-situ measurements and physical samples returned to Earth.

Structure and Composition:

The interiors of comet nuclei may be highly variable in their ratios of dust to gas; however most nuclei are coated in a veneer (or evaporative rind) of refractory dust and organic material, and are thought to contain greater abundances of condensed volatile material with increasing depth from the surface (Brownlee 2005). Spacecraft observations and measurements have determined densities for Comet 9P/Tempel 1, 81P/Wild 2, 19P/Borelly and 67P/Churyumov-Gerasimenko between 0.3-0.6 g/cm^3, indicating high porosities and low tensile strengths for these JFCs. Comets have albedos of 0.04-0.06, making them the darkest objects in the solar system. Their low albedos are likely the result of residual organic refractory material that became concentrated on comet surfaces during escape of volatile gases. The fragility of comets causes them to be easily disaggregated by tidal forces at perihelion or during encounters with Jupiter; these spontaneous disintegrations of JFC nuclei are prolific dust producing events, and have been suggested as the source of 90% of zodiacal cloud dust (Nesvorny, 2010). While meter-sized samples of the asteroid belt survive atmospheric entry and are recovered as meteorites, samples of comet dust accreted by the Earth appear to be restricted to μm to mm sized grains that are collected in the stratosphere and in Antarctic ices.

Stratospheric Interplanetary Dust Particles:

The term Interplanetary Dust Particles refers to a specific class of meteoritic material that has been collected in the stratosphere by U2 and ER2 aircraft in a program initiated by Don Brownlee in 1974 (Brownlee 1985b). Particles are collected on clean, plastic substrates coated with a thin layer of silicone oil; captured particles are removed and sorted in the cosmic dust

laboratory at NASA's astromaterials facility at Johnson Space Center. Particles of up to 500 μm have been recovered, but particles are typically 5-15 μm in diameter (Bradley 2010). Much of the material retrieved from collectors consists of volcanic ash and debris from solid rocket engines. Particles suspected to be of extraterrestrial origin are sorted into two classes: particles that have chondritic abundances (within a factor of three) for twelve major elements (designated "cosmic"), and particles consisting of single mineral grains including olivines, pyroxenes, and Fe-Ni sulfides with small amounts of adhering fine-grained chondritic material (designated "possibly cosmic"). The particles with chondritic abundances are generally further classified into two groups: IDPs with high porosities that consist of mostly anhydrous minerals (CP IDPs), and IDPs with low porosities consisting of more hydrated silicates (CS IDPs). IDPs are occasionally observed that exhibit morphologies or mineralogies that lie between these two classifications. While meteorites are derived largely from specific regions of the asteroid belt near mean-motion resonances with Jupiter (Gladman et al. 1997), IDPs are thought to be more representative samples of Solar System bodies than meteorites because they sample nearly all dust-producing sources >1 AU from the Sun.

Chondritic Porous IDPs have been the subject of most research, as they exhibit features that have not been observed in meteorites (Brownlee 1985a). One unique characteristic of these CP IDPs is that they have compositions that closely match the bulk compositions of CI chondrites, but on a much finer scale than has been observed in other unequilibrated meteoritic material. The carbon abundance of CP IDPs is typically ~3-6x that of the most C-rich carbonaceous chondrites (Thomas et al. 1993). Another characteristic feature of anhydrous IDPs is a high abundance of presolar silicate material. NanoSIMS instruments have been used to make isotope

maps of IDPs and identify inclusions with large $\delta^{17}O$ excesses of up to 3000‰; such anomalous compositions suggest a circumstellar origin (Messenger et al. 2003). Circumstellar silicate abundances have been estimated to be as high as 5500 ppm in CP IDPs (Messenger et al. 2003). Other features such as glasses embedded with metals and sulfides (GEMS) and enstatite whiskers are not observed in other meteoritic materials. Bulk oxygen isotopic compositions of CP IDPs show small ^{16}O excesses and depletions typical of carbonaceous chondrites (Aleon et al. 2009). The unique properties of the chondritic porous IDPs have led many researchers to suggest a cometary origin for these particles (Brownlee 1985a). There have also been arguments dynamically linking CP-IDPs to short-period comets based on inferred atmospheric velocities from He release studies (Brownlee et al. 1995). However, with the exception of Stardust, no definitive sample of a comet exists in collections. With the successful return of Wild-2 samples by the Stardust collection, the opportunity exists, for the first time, to directly compare known cometary samples with collections of IDPs suspected to have a cometary origin.

Chondritic-smooth IDPs are low porosity objects whose mineralogy is dominated by aqueous alteration products such as Mg-rich phyllosilicates (smectite and serpentine group) and Mg-Fe carbonate minerals. Their hydrated mineralogy combined with low atmospheric entry velocities have been used to infer an origin largely from asteroidal sources. Spectroscopic studies show that the types and abundance of organic matter in CS IDPs is similar to that in CP IDPs (Flynn et al. 2003). Although CS IDPs show broad similarities to primitive carbonaceous chondrites, only a few particles have been directly linked to specific meteorite groups such as CM and CI chondrites based on the presence of diagnostic minerals (Bradley and Brownlee 1991; Keller, Thomas, and McKay 1992; Rietmeijer 1996).

Many CS IDPs however, have carbon contents that greatly exceed that of known meteorite groups suggesting that they represent samples of more primitive parent bodies than meteorites (Keller, Thomas, and McKay 1993; Snead et al. 2012; Thomas et al. 1992). It is now recognized that many large, dark primitive asteroids in the outer main belt, as well as some trans-Neptunian objects, show spectroscopic evidence for aqueous alteration products on their surfaces (De Bergh et al. 2004; Fornasier et al. 2014; Takir and Emery 2012). Some CS IDPs exhibit large bulk D enrichments similar to those observed in the cometary CP IDPs (McKeegan, Walker, and Zinner 1985). Rare "hybrid" IDPs occur that represent CP IDP materials that have partly reacted with aqueous fluids to form hydrated minerals typical of CS IDPs (Keller, Thomas, and McKay 1992; Rietmeijer 1991; Nakamura, Messenger, and Keller 2005; Nakamura-Messenger, Clemett, et al. 2011). Experiments have shown that the anhydrous mineralogy of CP IDPs is highly reactive in the presence of aqueous fluids with extremely rapid reaction kinetics (Nakamura-Messenger, Clemett, et al. 2011). While hydrated minerals in comets have not been unambiguously identified to date, the presence of the smectite group mineral nontronite has been inferred from infrared spectra obtained from the ejecta from comet 9P/Tempel 1 during the Deep Impact mission (Lisse et al. 2006). Recent observations of low temperature sulfide minerals in Stardust mission samples suggest that limited aqueous activity may have occurred on comet Wild-2 (Berger et al. 2011). All of these observations, taken together, suggest that the high-carbon hydrated IDPs are abundant and important samples of primitive solar system objects not represented in meteorite collections.

NASA Stardust Mission:

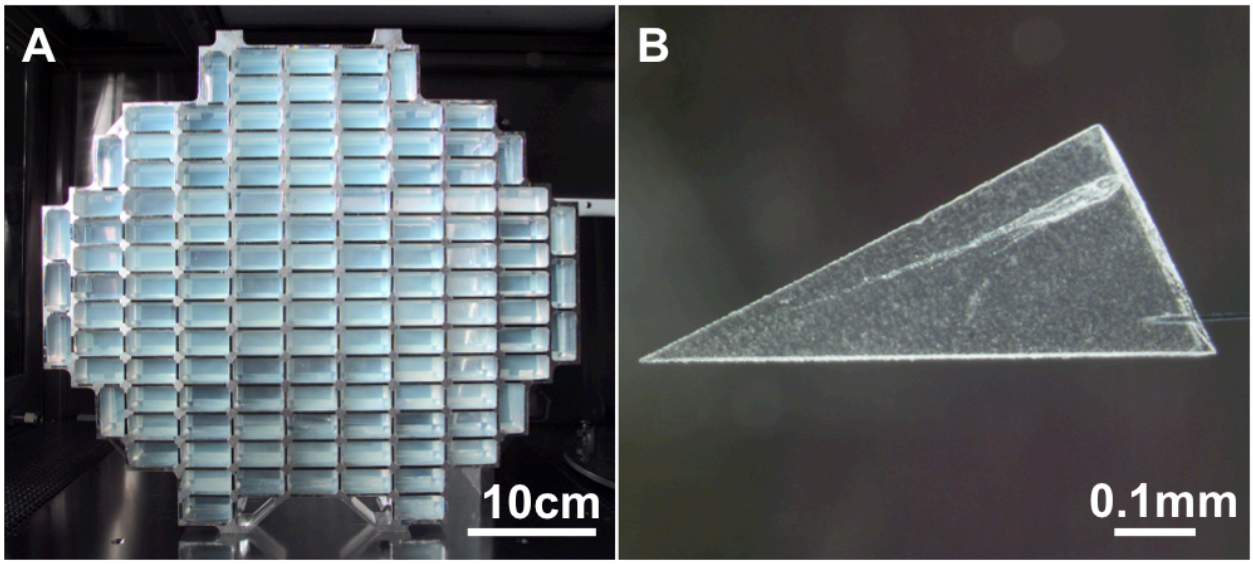

Fig. 1.3: A) The Stardust collector tray B) Extracted aerogel track containing Wild 2 dust particles (image credit: NASA Jet Propulsion Laboratory)

Mission Overview:

The Stardust mission, part of NASA's Discovery program, successfully achieved its primary objective of collecting and returning dust from comet 81P/Wild 2. Wild 2 is a 4.5 km dia. Jupiter family comet that likely accreted ~4.5 billion years ago in the Kuiper Belt region of the solar system. Through a series of planetary counters (most recently with Jupiter in 1974), Wild 2 acquired a six-year orbit that crosses into the inner solar system, providing access to materials that have remained unaltered since the comet's formation. The Stardust spacecraft intercepted comet Wild 2 on January 2, 2004 at an encounter velocity of 6.1 km/sec and a distance of 234 km from the nucleus; it flew through the dust tail with a deployed sample collector comprised of 126 tiles of silica aerogel encased in an aluminum frame, and collected approximately 300μg of particles. In addition to the silica aerogel, aluminum foil placed around the tiles to aid in their removal from the frame provided a complimentary collecting medium. 1039 cm^2

of aerogel and 152 cm^2 of Al foil were exposed to Wild 2 dust during the encounter (Horz et al. 2006). The spacecraft returned to Earth on January 15th, 2006, with the sample return capsule landing at the Utah Test and Training Range. The sample return capsule was transferred to a designated receiving and processing laboratory at the Johnson Space Center Astromaterials Curation Facility, where successful collection of Wild 2 dust was confirmed. Before samples were removed from the collector for preliminary analyses, detailed photodocumentation and cataloging of the sample tray were performed by the Stardust curators.

Selected Results:

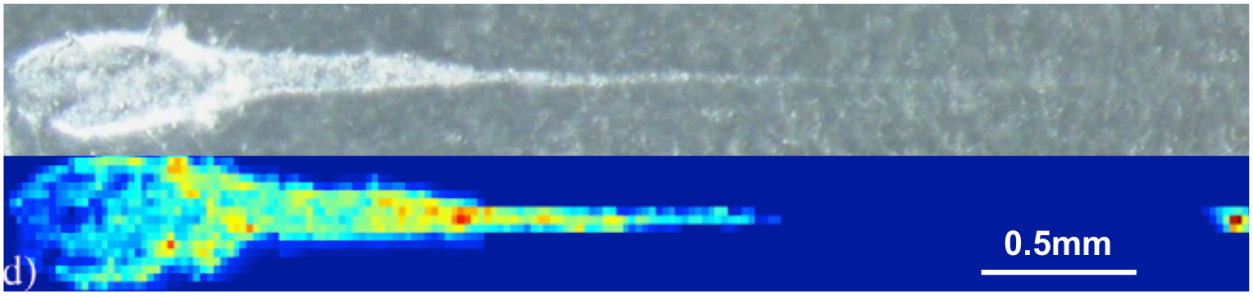

Fig. 1.4: Optical and Fe synchrotron images of track C2044,0,43. (Courtesy SSRL)

Preliminary examination of the sample collection revealed a diversity of impact features, both in the aerogel cells and on the surrounding foils (Horz et al. 2006). Light gas guns at the University of Kent and at Johnson Space Center had been previously utilized to perform calibration experiments by firing a diverse suite of projectiles into aerogel and into aluminum foil targets at Stardust encounter velocities (Kearsley, Burchell, Horz, et al. 2006; Kearsley, Burchell, Wozniakiewicz, et al. 2006). Impacts into aerogel by dense projectiles of homogeneous composition form long, carrot-shaped features; more complex, lower density materials produce features with more bulbous, radish-shaped morphologies. When compared against the light gas

gun results, Wild 2 dust encountered by the Stardust collection was diverse in both size and in structural integrity. Many impact features were characterized by a bulbous cavity lined with dark, fine-grained material, with one or more root-shaped tracks penetrating deeper into the aerogel. This diversity of impactors was also observed in the Al foils, with some features exhibiting overlapping craters and depressions and others resembling classic, bowl-shaped depressions. Most of the mass encountered by the spacecraft was contained in a few large impacts (Horz et al. 2006). Synchrotron X-ray Fluorescence analyses suggest that 65% - 90% of the collected grain mass resides in the upper bulbous portion of the carrot and bulb shaped aerogel tracks, and 10% - 35% of the mass is contained in the terminal particles located at the end of the tracks (Flynn et al. 2006). Crystalline material in the upper portion of an impact feature is almost always observed to be in submicron sized grains, with almost all bulbous features containing one or more stylus features containing larger crystals. This has led to a model of captured Wild 2 dust as aggregates of loosely fine grained (~10nm) material and occasional larger (> 1μm) mechanically robust grains.

A result of major importance in the understanding of comet formation was the identification of large (>1μm) high-temperature crystalline silicates, Fe-Ni sulfides and Fe-Ni metal in many of the tracks. Condensates such as Low Iron, Manganese Enriched (LIME) forsterite and osbornite (TiN) have been observed, as well as several calcium-aluminum inclusions (CAIs) and particles consistent with chondrule fragments in Stardust samples. The presence of these large, high-temperature phases in a sample that accreted in the outer solar system is strong evidence of efficient, large-scale radial mixing in the early solar system, rather than annealing of amorphous interstellar silicates (Zolensky et al. 2006). A definitive estimate of the proportion of crystalline

to amorphous material has not been obtained, as capture into silica aerogel severely altered the fine-grained components of Wild 2 dust. Features resembling GEMS found in CP-IDPs were observed in aerogel tracks; however most (if not all) such features were the result of the mixing between melted fine-grained dust and molten silica aerogel during the hypervelocity capture process. At least one particle with hydrated mineralogy has been reported (Berger et al. 2011); however evidence for aqueous alteration of Wild 2 dust remains extremely rare.

Ion probe analyses of Stardust samples did find an isotopically anomalous presolar grain, but the overall abundance of such circumstellar grains is far lower than expected. This is contrary to early predictions that modeled comets as large aggregates of presolar grains (hence the mission name); these predictions seemed to be supported by high presolar grain abundances in anhydrous porous interplanetary dust particles (IDPs), which are believed to have a cometary origin (D. Brownlee 1985). However, destruction of fine-grained material during theaerogel capture process likely introduced a strong sampling bias. Experiments firing Acfer 094 into aerogel at Stardust encounter velocities have shown that >90% of O-rich presolar grains are destroyed during the capture process (Floss et al. 2013).

There have been ~10-15 oxygen isotope measurements made on terminal particles found at the end of aerogel tracks, or along track walls (McKeegan et al. 2006; Nakamura et al. 2008; Nakamura-Messenger, Keller, et al. 2011; Nakashima, Ushikubo, Joswiak, et al. 2012; Ogliore et al. 2015). Thus far, these measurements have revealed surprising similarities to anhydrous minerals in carbonaceous chondrites. One particle from Track 25 of the collector contains refractory materials similar to those found in calcium-aluminum rich inclusions common in

carbonaceous chondrites (McKeegan et al. 2006). The relationship between this particle and the CAIs found in meteorites is further supported by an oxygen isotope value of -40‰, measured on the IMS 1270 at the UCLA SIMS lab. Other such ^{16}O-rich values have been found in measurements of olivine terminal particles. Most measurements on Wild 2 dust solids, however, reveal oxygen isotope values that are closer to the intersection between the CCAM line and the TF line.

Limitations of Oxygen Isotope Measurements of Dust Extracted from Aerogel:

The measured O-isotope compositions have been interpreted as evidence for large-scale radial migration of dust components from the inner solar nebula to the accretion regions of Jupiter-family comets. If this interpretation is correct, what these studies have so far not achieved is a measurement of the average oxygen isotope composition of the dust component of material that formed and accreted in the distal cold regions of the nebula (well beyond the snow line). For instance, in some carbonaceous chondrite types (e.g. CV type chondrites), the matrix component, which is analogous to the fine-grained CP-IDP material, is a strong contributor to the bulk oxygen isotope composition. Hypervelocity capture into aerogel resulted in fine-grained material (analogous to CP-IDP material) that was melted and intimately mixed with the SiO_2 capture medium. Thus the oxygen isotope measurements made so far have been biased in favor of the robust single mineral olivine and pyroxene grains that represent particles that were transported from inner solar system regions, as well as Fe-Ni metals and sulfides. Hypervelocity capture into Al foil substrates produce impact craters which capture material from the impactor without significant oxygen contamination, allowing for analysis of both the coarse and fine-grained components of the Wild 2 dust.

Thesis Objectives:

This thesis describes the Secondary Ion Mass Spectrometry (SIMS) measurements of twelve Stardust impact crater residues, with the goal of obtaining an average oxygen isotope composition of Wild 2 dust. Residues from crater impacts preserve both the coarse (>1μm) crystalline dust component and the fine-grained (<1μm) component of Wild 2 dust with equal efficiency and less background contamination than material extracted from silica aerogel tracks. Precision SIMS analyses of crater residues have not been previously reported, and potential effects of hypervelocity capture on oxygen isotope compositions must be understood in order to make meaningful interpretations of ion probe measurements of Wild 2 craters. This thesis also presents results of SIMS measurements of analogue crater residues of known initial oxygen isotope composition produced via light gas gun experiments. These lab-produced crater residues were used to develop sample preparation and analysis procedures in preparation for the analysis of Stardust residues, as well as for standards to correct for instrumental mass fractionation and matrix effects during Stardust crater measurements. Finally, this thesis discusses the oxygen isotope compositions, as measured via SIMS, of five carbon-rich hydrated interplanetary dust particles, their relationship to their anhydrous counterparts, and implications of results for models of early solar system evolution.

Chapter 2 of this thesis describes the experimental methods used, including an overview of the Cameca IMS-1270 instrument and analytical conditions used for 3-oxygen isotope measurements of the craters and the hydrated IDPs. Chapter 3 presents details of techniques developed for the SIMS measurements of impact crater residues, including production of simulated analogues using a suite of minerals of known oxygen isotope composition. Results of the SIMS

oxygen isotope measurements of these standard mineral residues are reported, and the implications for analysis of the Stardust craters are explored. Chapter 4 presents a description of the samples analyzed for this study, including results of scanning electron microscope (SEM) and energy dispersive spectrometry (EDS) analyses for the Stardust crater residues, and electron microprobe analyses for the hydrated IDPs. Chapter 5 will present results for the SIMS oxygen isotope measurements of the Stardust crater residues and for the oxygen isotope measurements of the hydrated IDPs. Chapter 6 discusses the relationship of Wild 2 dust to primitive meteorites, anhydrous and hydrated IDPs, and Antarctic micrometeorites; implications for models of oxygen isotope heterogeneity and for comet formation and accretion will be explored. Concluding remarks are presented in Chapter 7.

Chapter 2: Experimental Methods

Secondary Ion Mass Spectrometry:

The oxygen isotope compositions reported in this study were obtained via secondary ion mass spectrometry (SIMS) by using the UCLA Cameca IMS-1270 ion microprobe. In SIMS analysis, a focused primary ion beam is used to sputter a localized (~10μm) region of a solid sample. Some fraction of the sputtered material emerges from the sputtered area as ionized species; these secondary ions are accelerated through a hole in the extraction plate, shaped by transfer optics and injected into a double focusing mass spectrometer. Ions emerging from the spectrometer are measured with counting detectors or Faraday cups; alternatively because the instrument is also an ion microscope, an image may be formed and amplified on a channel plate. A thorough description of SIMS instrumentation and analyses can be found in McKeegan (1987), and a cursory discussion will be given here as it pertains to analytical conditions and sample constraints for our measurements.

SIMS Overview:

Primary Column: For analysis of oxygen ions, a cesium ion primary beam is utilized. Cesium carbonate is vaporized and ionized via contact with a tungsten plate heated to 1100°C; the resulting ions are accelerated out of the source due to a potential difference of +10KV between the ionizer and an extraction plate. Spurious ion species are filtered from the beam as it passes through the primary beam mass filter (PBMF). A series of electrostatic lenses (L1-L4) and

deflectors shape and focus a ~0.5-3nA primary beam prior to impact with the sample surface.

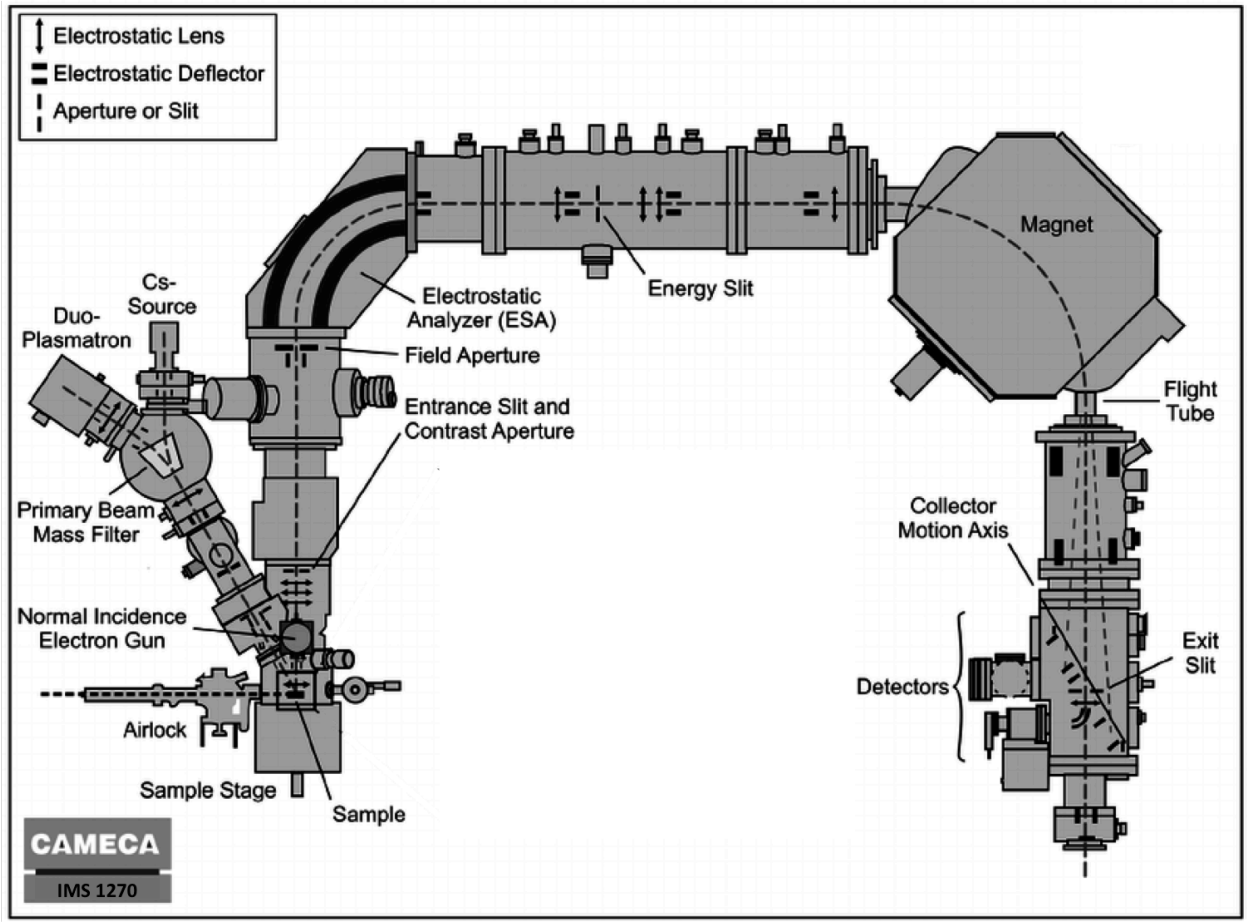

Fig. 2.1: Schematic of Cameca IMS-1270 series ion microprobe (image credit: Wisconsin Secondary Ion Mass Spectrometer Laboratory).

Transfer Section: The focused primary ion beam passes through a hole in the extraction plate and impacts the sample surface with an energy of 20KeV, causing a collision cascade on the sample surface. This cascade causes the ejection of electrons, neutral and ionized atomic and molecular species from the top several monolayers of the sample surface. The ion beam is focused to sputter material from a localized (20-30µm) region of the surface, or can be rastered via deflectors over an area up to ~15-25µm wide. The sample is held at -10KV and forms a uniform electric field with the grounded extraction plate. Negatively charged secondary ions are

accelerated in this field through a central hole in the extraction plate; the distortion of the uniform accelerating field near the extraction hole acts as a diverging lens for the ions. Any sample surface topology will also distort this field, causing mass-fractionation artifacts; therefore the samples must be very flat for precision isotope analyses (Kita et al. 2009). The increasing concentration of Cs^+ ions implanted into the sample surface changes the ionization fraction and the efficiency at which material is sputtered; this changing sputter yield is not constant amongst elemental and isotopic species. After some time, the rate at which Cs^+ ions are implanted is the same as the rate at which Cs^+ ions are sputtered, and equilibrium is reached. Typically, samples are pre-sputtered for a period of several minutes to ensure that isotopic data are only collected after sputtering equilibrium has been achieved. The sputtering of negative ions and electrons by the Cs^+ primary beam causes sample charging; electrons are resupplied to the sample surface via electron flood gun to compensate for this sample charging effect (Slodzian 1980). Diverging secondary ion paths form a virtual image plane that contains information about ion points of emission, and a virtual crossover plane that contains information about the angular and energy distributions of ions over the entire sputtered area. These virtual planes are converted into real image and real crossover planes via electrostatic lenses in the transfer section.

Mass Spectrometer: The mass spectrometer consists primarily of an electrostatic analyzer and a magnetic prism that, in conjunction, act in a manner analogous to an optical achromat lens, focusing ions in both energy and in angle. Ideally, a monoenergetic, collimated beam of ions would enter a magnetic field of an electromagnetic sector and experience a cyclotron force such that all ions with a mass to charge ratio q/m would be deflected along the same path. In practice, however, sputtered secondary ions are neither collimated nor are they monoenergetic. The

electrostatic analyzer, which generates a static electric field between concentric electrodes, disperses ions of differing kinetic energies such that, in combination with an electrostatic lens, compensates for the energy dispersion of the magnetic prism. The ESA/spectrometer lens/magnetic prism combination also acts to focus ions with angular dispersion, resulting in a doubly focused ion beam of a specific q/m emerging from the magnetic prism.

Detection System: For isotope analyses, ions traveling along the axial path are diverted by an electrostatic analyzer (ESA) to into a mono-collection detection system and are quantitatively measured by either an electron multiplier or a Faraday cup. Faraday cups (F.C.s) collect incoming ions and measure the current delivered via an operation amplifier with a feedback resistor of 10^{10} – 10^{11} ohms. Faraday cups have a high background that is associated with thermal instability in the resistor; therefore, for precision isotope measurements, F.C.s are best utilized with ion count rates count rates $>10^6$ c.p.s. Background and yield corrections must be applied to the F.C. raw count rate. Electron multipliers work by converting ion impacts onto a dynode into secondary electrons, which in turn strike other dynodes in succession, causing a cascade until an electrical current pulse of typically ~5 to 10 nsec duration is suitably amplified for measurements. This method is extremely sensitive to low ion count rates; however electron multipliers have certain limitations. Ion count rates higher than 10^6 c.p.s. severely compromise the ability for the dynodes to recover; as such, EMs are typically limited to count rates $< 1x10^6$ c.p.s. The dynodes and counting system also have a non-zero recovery time, during which any incoming ions will not be counted; therefore a detector dead time correction must be applied to the raw ion count rate. In addition to the axial mono-collection system, The UCLA IMS-1270 is equipped with a multi-collector detection system that enables the simultaneous counting of

secondary ions with mass differences from ~1/210 to 1/12, and can work either in conjunction with or independently from the axial detector. Electron multipliers and Faraday cups are mounted on motorized trolleys that can be positioned along the mass focal plane relative to the axial position. Either electron multipliers or Faraday cups can be mounted at any of the five trolley positions (L2, L1, C, H1, and H2); two permanently mounted faraday cups are also fixed to the innermost and outermost trolleys and are designated L'2 and H'2. For all analyses reported in this work, the trolleys were configured with electron multipliers in the L2, L1 and H2 positions and with Faraday cups in the L'2, C, H1, and H'2 positions.

SIMS Analytical Conditions:

Stardust craters were analyzed for oxygen isotopic composition using the UCLA Cameca IMS-1270 ion microprobe in two different analysis modes: spot mode and raster mode. In spot mode, craters were analyzed using a 0.5nA, 20KeV, cesium primary beam defocused to ~25μm; more focused beams drilled through the residue before sputtering equilibrium was reached in the analysis region. In raster mode, a focused 5μm beam rastered over a 15x15μm area was used in place of the defocused primary beam; dynamic transfer optics were used to present a stationary beam at the entrance of the mass spectrometer. In both modes, normal-incidence electron flooding was used for charge compensation. Because the secondary ion signal will necessarily vary during a measurement, acquisition of precise data requires simultaneous counting of the 3 oxygen isotope beams (i.e., multi-collection). A 2 electron multiplier and 1 Faraday cup detector configuration produced the most precise results, given our ^{16}O count rates of ~$1x10^8$ c.p.s.

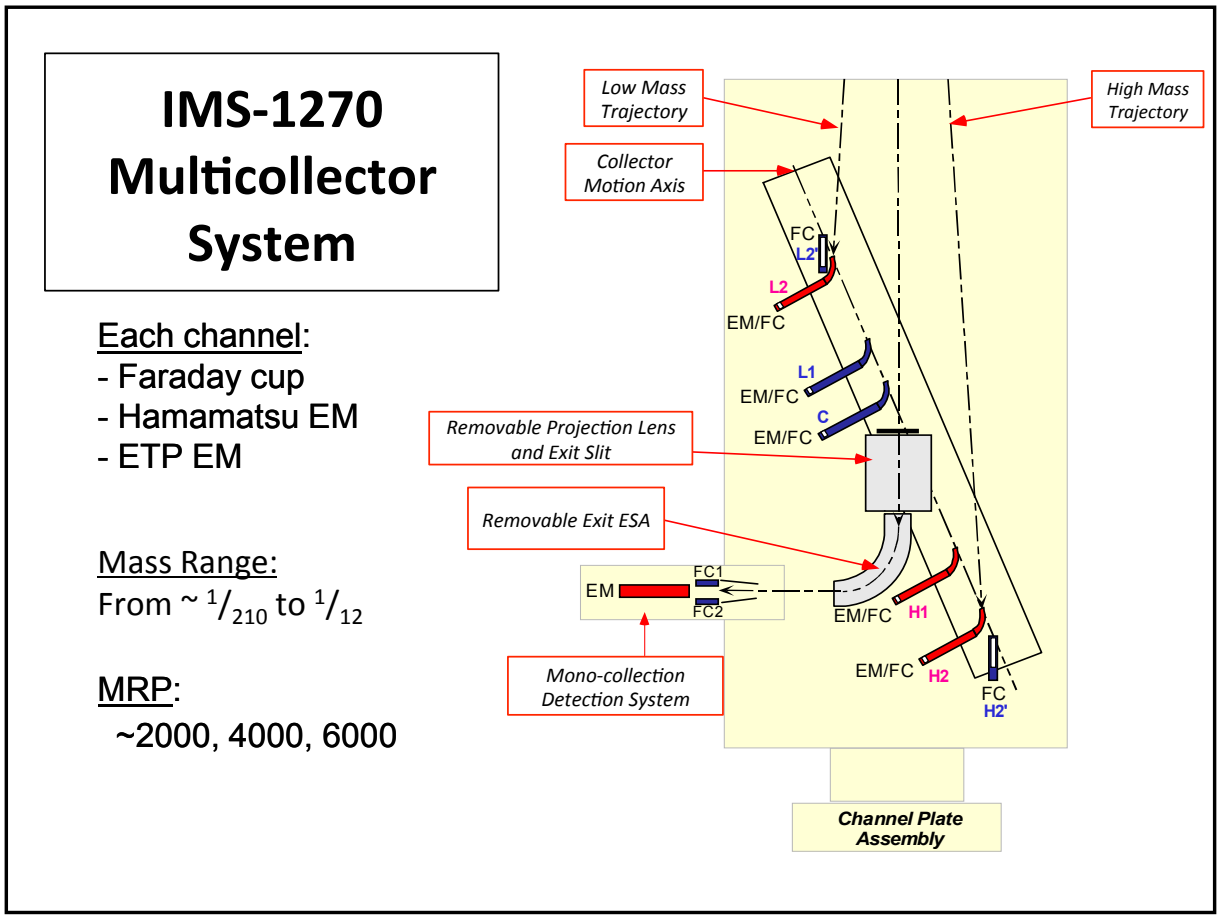

Fig. 2.2: Schematic of the IMS-1270 Multi-collector system. A Faraday cup is mounted on the C trolley, and an electron multiplier is mounted on the H2 trolley.

A mass resolving power of 6000 was used to separate the interfering $^{16}OH^-$ peak from the $^{17}O^-$ signal.

Data Analysis: The raw data from the ion microprobe measurements is output in a series of analysis cycles. Crater analyses were counted for 300-400 cycles of 5 seconds per cycle; IDP analyses were counted for 15 cycles of 10 seconds per cycle. Background and detector yield corrections are applied to data acquired on C Faraday cup:

$$\left(\frac{Raw\ counts}{detector\ yield}\right) - background$$

Deadtime corrections are applied to data collected on electron multipliers:

$$C_o \cong C_m(1 + C_m\tau)$$

where C_o is the true count rate, C_m is the measured count rate, and τ is the detector deadtime (τ = 30 nanoseconds for the axial EM, and τ = 65 nanoseconds for the multicollector H2 multicollector EM). The ratios of $^{18}O/^{16}O$ and $^{17}O/^{16}O$ and the $\delta^{18}O$ and $\delta^{17}O$ are determined for each analysis cycle; ratios and delta values are then averaged and standard errors are calculated. Because of the fragile nature of the crater residues and the unknown depth of the material remaining, we chose not to employ an arbitrary presputter; instead, all of the sputtered ions were counted. After applying background, yield and deadtime corrections, we performed a change-point analysis (R Development Core Team 2013) on our data in order to determine when the sample attained sputtering equilibrium; data points collected prior to the change point were excluded.

Isotope ratios are corrected for instrumental mass fractionation (IMF) internally by calibration against mineral standards of known isotope composition. The ion yield of a particular element is dependent on the matrix in which it resides; therefore standards are chosen to match the mineralogy of the unknown sample as closely as possible to correct for such matrix effects. The H2 electron multiplier encountered consistently high counts, resulting in aging that would

manifest as a linear decrease in the IMF correction factor. Each analysis of an unknown sample was bracketed by measurement of mineral standard, and a correction factor was estimated based on a liner fit of the $^{18}O/^{16}O$ IMF factor vs. time. The IMF factor associated with the $^{17}O/^{16}O$ ratio was constant over the course of an analysis session due to the comparatively low $^{17}O^-$ ion count rate encountered by the axial EM. Errors associated with the corrections were propagated into the errors associated with measurement (Lyons 1991):

$$\sigma_f = f\sqrt{\left(\frac{\sigma_x}{x}\right)^2 + \left(\frac{\sigma_y}{y}\right)^2}$$

where x is the isotope ratio and y is the correction factor. For Wild 2 crater measurements, Instrumental mass fractionation was corrected by analysis of lab-produced impact residues of San Carlos olivine described below, as well as a single crystal of San Carlos olivine, both of which were mounted on the same 1" disk as the Stardust crater.

Other Analytical Techniques:

Scanning Electron Microscopy: After the receipt of allocated of foils from NASA's Johnson Space Center Astromaterials Curation Facility, impact craters were located visually under 20-40x magnification, and then imaged and analyzed for chemical composition via scanning electron microscopy (SEM) and energy dispersive spectrometer (EDS). The elemental analysis and mapping of each crater provided information about the distribution of the residue as well as compositional information for appropriate mineral standard matching. Four craters from the

initial allocation were imaged, profiled and analyzed for chemical composition using a FEI Nova FESEM equipped with a Thermo Fisher Scientific Noran 7 EDS detector at the UCLA Dept. of Material Science and Engineering, and a using a JEOL 5900 LV SEM and a Bruker XFlash quad EDS detector at the Natural History Museum in London. Nine craters from subsequent allocations were analyzed using a Tescan Vega 3 SEM equipped with and EDAX EDS detector at the UCLA Department of Earth, Planetary and Space Sciences.

Electron Microprobe Analysis: Chemical abundances for the allocated hydrated interplanetary dust particles (IDPs) were determined using a CamecaSX-100 electron microprobe equipped with five wavelength dispersive spectrometers (WDS) and one energy dispersive spectrometer (EDS).

Transmission Electron Microscopy: Hydrated IDPs and particles from one Stardust crater (C2049N,1) were analyzed using a JSC JEOL 2500SE scanning and transmission electron microscope (STEM) equipped with a Noran thin-window energy-dispersive x-ray detector and a Gatan Tridiem imaging filter for energy-filtered imaging and electron energy-loss spectroscopy (EELS). The TEM measurements provided information about the mineralogy of the grains, their nm-scale compositions and microstructures and petrographic relationships.

NanoSIMS: D/H and oxygen isotope compositions were obtained for a ~70nm thin section of hydrated IDP C35 using a Cameca 50L Nanoscale Secondary Ion Mass Spectrometer (NanoSIMS) at the Astromaterials Research & Exploration Science facility at NASA's Johnson Space Center. The principle of NanoSIMS operation and analysis are similar to those describe

for the IMS-1270; however, the primary optics and the secondary extraction optics are co-axial, allowing for normal incidence ion beam sputtering (and therefore smaller probe size).

Sample Preparation:

Ultramicrotomy: Samples that were analyzed by transmission electron microscopy were prepared by ultramicrotomy. Blocks of hardened resin cylinders capped with truncated pyramids (often referred to as bullets) were prepared using a four-component epoxy (EMbed-812, Electron Microscopy Sciences, supplier). This epoxy was prepared by mixing 5ml of EMbed-812 and 8 ml of Dodecenyl Succinic Anyhdride (DDSA) components into one mixture (mixture A), and combining 8ml of EMbed-812 and 7ml of Nadic Methyl Anhydride (NMA) into a second mixture (mixture B). The hardness of the final resin can be varied by combining mixture A and mixture B in variable proportions; for our experiments, an A:B ratio of 1:4 was utilized. Once mixtures A and B were combined, 0.5ml of DMP-30 accelerant were added. The resin was then poured into polyethylene molds and cured at 60°C for at least 24 hours. Each particle was then transferred to the apex of a cured resin bullet using a glass needle, fixed in place and covered using a drop of uncured Embed-812, and cured for 24 hours at 60°C. Alternatively, hydrated IDPs were embedded in drops of molten sulfur atop epoxy bullets in order to preserve their organic compositions. The bullets topped with the particles to be analyzed were then sliced into 70nm sections using an ultramicrotome - a specialized instrument that consists of a mechanical arm that advances forward in a circular motion in submicron increments. An adjustable chuck is placed at the end of the arm, and the epoxy bullet is clamped in this chuck. As the chuck advances, the tip of the resin bullet passes over a diamond knife that is attached to an aluminum

water-filled reservoir, slicing a 70nm section that floats atop the water. Each circular advance of the mechanical arm produces another section attached to the previous slice, eventually resulting in a ribbon of 10-20 slices. A stereomicroscope mounted to the ultramicrotome is used for examination and manipulation of the sections. Cross-sections of the particle typically appear after 50-100 sections are sliced. The particle-containing ribbons are lifted from the water-filled reservoir on specialized copper grids designed for use in TEM analyses. Particles were not completely sectioned; in the case of the hydrated IDPs, modest heating liberated the particles from their sulfur embedding substrates.

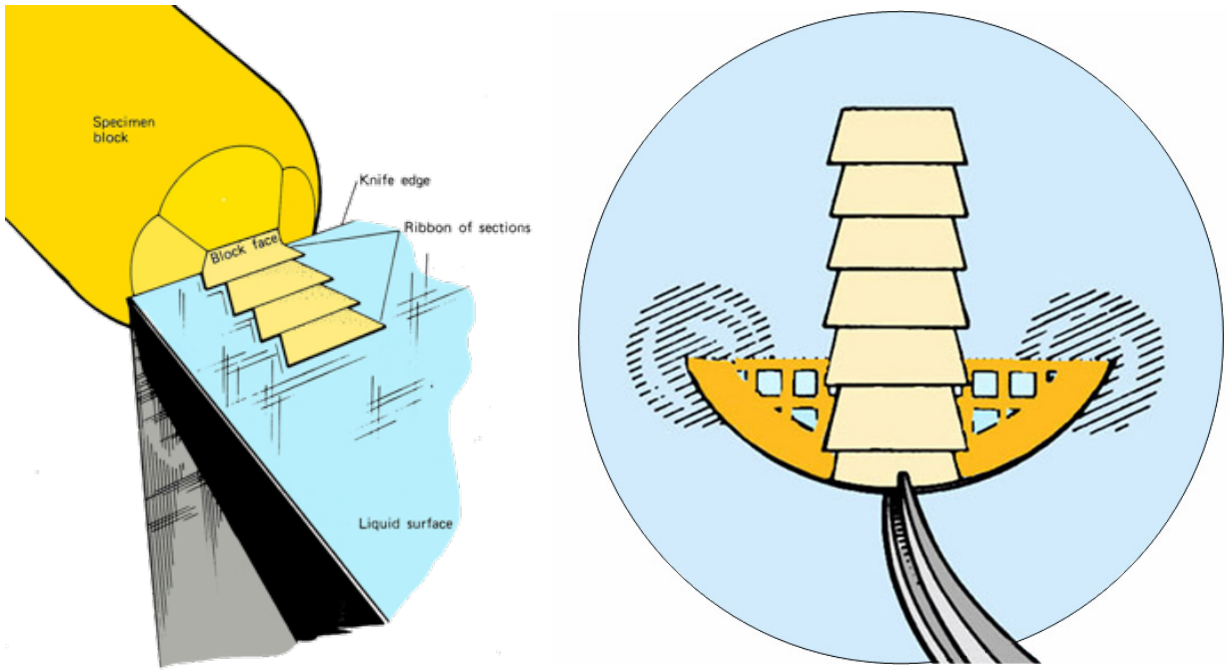

Fig. 2.3: Ultramicrotomy procedure. Embedded particles are sectioned into 70nm slices via diamond knife and placed on copper TEM grids. (image credit: Keiko Nakamura-Messenger)

Ion probe mounts: All ion probe mounts in this study were machined from 1" diameter T6061 aluminum round bar stock (McMaster-Carr, supplier) into $^{1}/_{8}$"- $^{3}/_{16}$" thick blank disks. Epoxy was avoided in mount construction in order to minimize sample contribution to the $^{16}OH^{-}$

interference. Front (i.e beam facing) surfaces were hand ground using water with a succession of increasingly finer grit SiC paper: 600 (P1200), 800 (P1500), 1200 (P4000), and then hand polished using polishing pads embedded with 3µm, 1µm and 0.25µm water-based diamond suspensions. In order to secure samples to the ion probe mount, 99.9999% pure indium shot (ESPI metals, supplier) was used in place of epoxy. Indium is sufficiently malleable at room temperature to act as a viscous fluid under pressure; yet it exhibits a rigidity that allows it to be polished flat. These unique mechanical properties make it an adequate, low-hydride background substitute for epoxy. Indium's conductivity also makes it desirable for use in negative ion analyses that require the electron flood gun.

Standard and Tuning Mounts: Two standardization and tuning mounts were manufactured specifically for the oxygen isotope measurements reported in this study. These will subsequently be referred to as mount #3 and mount #4. Each mount was machined from a round of T6061 aluminum into 1" diameter × $^{1}/_{8}$" thick disks. For mount #4, six through holes with diameters of $^{1}/_{16}$" were drilled $^{1}/_{4}$" from the disk center in 60° intervals using a rotary table fixed to a milling machine; this ensured that all measurements were made equidistant from the mount center, minimizing variations between mineral standards due to edge effects (Kita et al. 2009). For mount #3, eight $^{1}/_{16}$" dia. holes were drilled in 45° intervals $^{1}/_{4}$" from the disk center. Seven of these holes were drilled through the entire disk thickness; the eighth hole was plunged ~80% of the thickness of the disk; a #80 bit was used to drill a 340µm clearance hole for use in tuning of the electron gun. In both mounts, an additional $^{1}/_{16}$" diameter hole was drilled through center. On the front (i.e. ion beam facing side) of the disk, the through holes were partially enlarged by plunging the cutting edge of a $^{1}/_{8}$" drill bit (or mount #3) or a $^{3}/_{16}$" drill bit (for mount #4) to a

depth of $^{1}/_{32}$" for mount 3 and $^{1}/_{16}$" for mount 4. The fronts of these mounts were then sanded flat using grit 400 (P800) silicon carbide paper. After disks were cleaned, the tapered holes were filled with indium metal. This was accomplished by slicing the teardrop-shaped indium shot into fragments that approximately matched the taper profiles, and then by manually pressing the pieces into the holes with tweezers. The disks were then placed face down onto a flat aluminum plate; 1/16" steel dowel pins held in a pin vise were used to further compress indium from the back of the mount, ensuring all void spaces were eliminated. Once the standard mounts were filled with indium, mineral standards were placed into each of the holes. For mount 3, grains of the following minerals were pressed into each of the seven circumferential indium-filled wells: San Carlos olivine, San Carlos pyroxene, Durango apatite, Eagle Station olivine, Afrique magnetite, Burma spinel, and benitoite. For mount 4, the grains of the following minerals were pressed into five of the six circumferential indium-filled wells: San Carlos olivine, Burma spinel, Afrique magnetite, Madagascar hibonite, and chlorite; a fragment of NIST 610 glass was pressed into the sixth well. The mineral standards were pressed such that the top 25-50% of the grain protruded above mount surface. The protruding portions of the grains were ground flush with the Al disk surface using grit 400 silicon carbide paper. The front of the mount was then ground and polished using the techniques described above. After the mounts were polished, 1000 mesh copper grids were pressed into the central, indium-filled holes; these were used for instrumental tuning prior to stable isotope analyses.

Crater Residue Mounts: Standard mineral and Wild 2 impact craters were flattened (using techniques described in Chapter 3) and mounted onto 1" diameter × $^{1}/_{4}$" thick aluminum disks that were machined using techniques similar to those described above. The center of each disk

contained a single polished crystal of the matching mineral standard (e.g. San Carlos olivine for craters shot with San Carlos olivine powders). Approximately $^{1}/_{8}$" from the disk center, two-stepped holes were drilled into the side opposite the polished mineral standard (i.e the backside of the disk) using a $^{1}/_{16}$" dia. drill and a #74 drill (0.0022") dia. drill to penetrate the last 100μm of the Al disk. Indium was then placed into each hole, and partially pressed from the back such that an indium negative meniscus could be observed from the smaller, front-facing hole; flattened craters were then placed onto the meniscus. A 1" round thin section slide was mechanically fixed to ion probe mount, and each indium-filled well was pressed from behind until the indium completely surrounded the flattened craters. Mounting operations were performed in a class 1000 laminar flow bench, using a Wild M5A stereomicroscope.

Hydrated IDP Mounts: The IDP mount used for the 2012 SIMS analysis session was prepared at Johnson Space Center's Astromaterials Curation Facility using the sample preparation methods first reported in the Ph.D thesis of (McKeegan 1987). A 5mm x 5mm by 125μm thick piece of cleaned, high purity Au foil was pressed onto a 1" diameter aluminum mount that had numerous deep, narrow channels cut into the central portion of the disk. Three IDPs were pressed onto this mount; unfortunately, one of the IDPs (L2079C19) was lost in transit from Johnson Space Center to UCLA. To ensure subsequent IDPs were not lost in transit, several modifications were made to the mounting procedure. A $^{1}/_{8}$" diameter disk was punched from a sheet of 0.25mm thick, 99.9975% pure Au foil (Alfa Aesar, supplier). The disk of Au foil was then annealed at ~800°C and then quenched in order to remove any work hardening resulting from the foil manufacturing process. After annealing, the Au disk was immersed in a 29M HF acid bath overnight. Despite the high nominal purity of the gold, numerous bright specks have been observed in an oxygen

ion image of the foil surface. While McKeegan removed this contamination by sputtering the top several μm of the foil with an argon ion milling machine, HF cleaning proved to be an equally effective (and perhaps more widely available) method of removing surface contamination. The annealed and HF-cleaned Au foil disk was then mounted on a 1" aluminum disk that was manufactured, ground and polished in a similar manner to the Al blanks used for the standard, tuning and crater mounts. Prior to pressing, a shallow, $^{1}/_{8}$" diameter well was carefully machined into the Al probe mount via lathe to a depth comparable to the thickness of Au foil; numerous deep scratches were made on the bottom of the shallow well with a hobby knife. The Au foil disk was pressed into the machined well using a polished stainless steel anvil and an arbor press. Once the foil was fixed onto the mount, a clean, 250 mesh copper TEM grid was placed on the surface of the gold and pressed using the same apparatus; once removed, an array of 250 x250 μm square mesas remained, providing a convenient coordinate system for particle placement and location during ion probe analysis (Fig. 2.4).

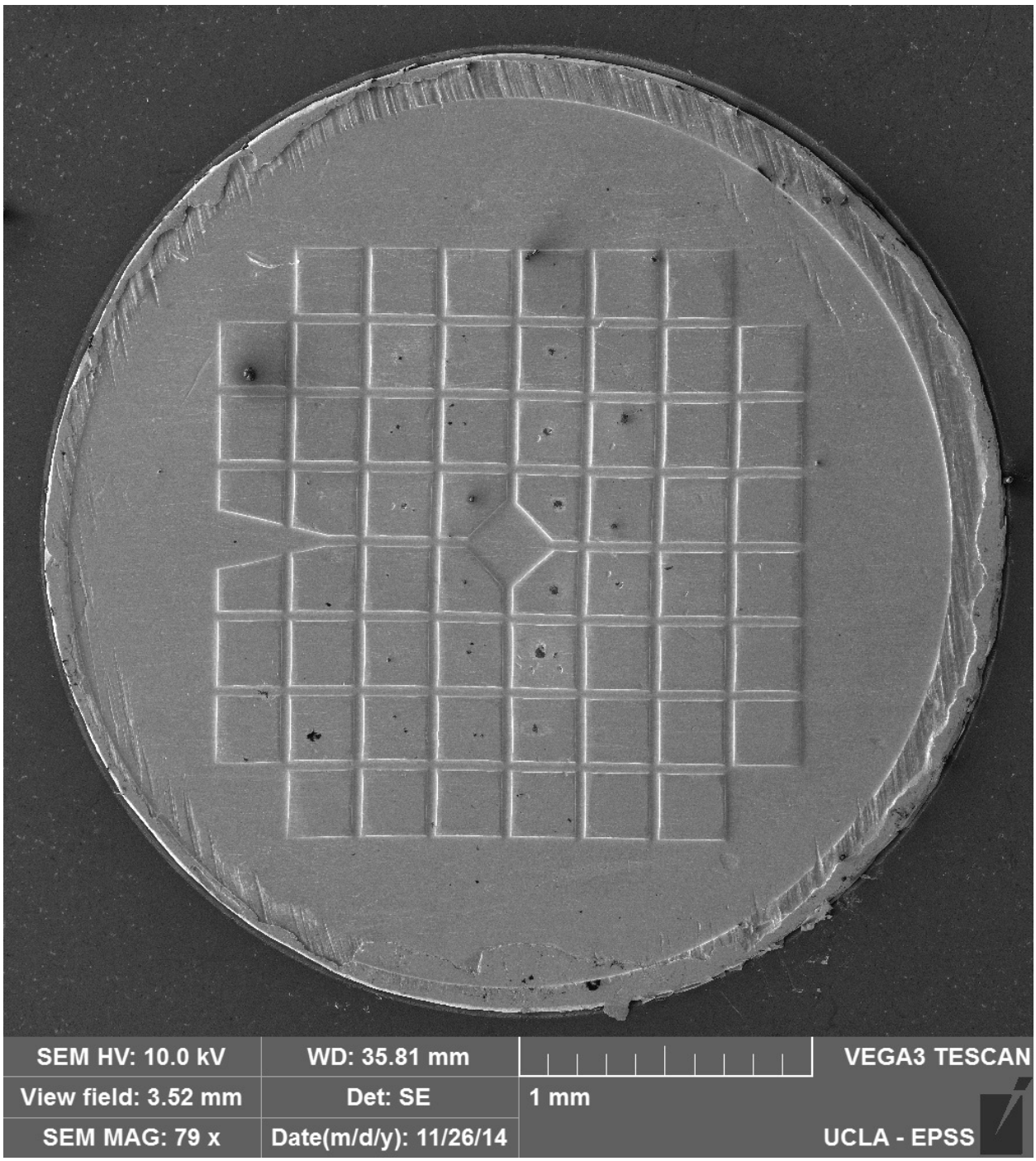

Fig. 2.4: Secondary electron image of IDP mount. Particles in this image are standard mineral grains and located at approximate centers of TEM grid depressions.

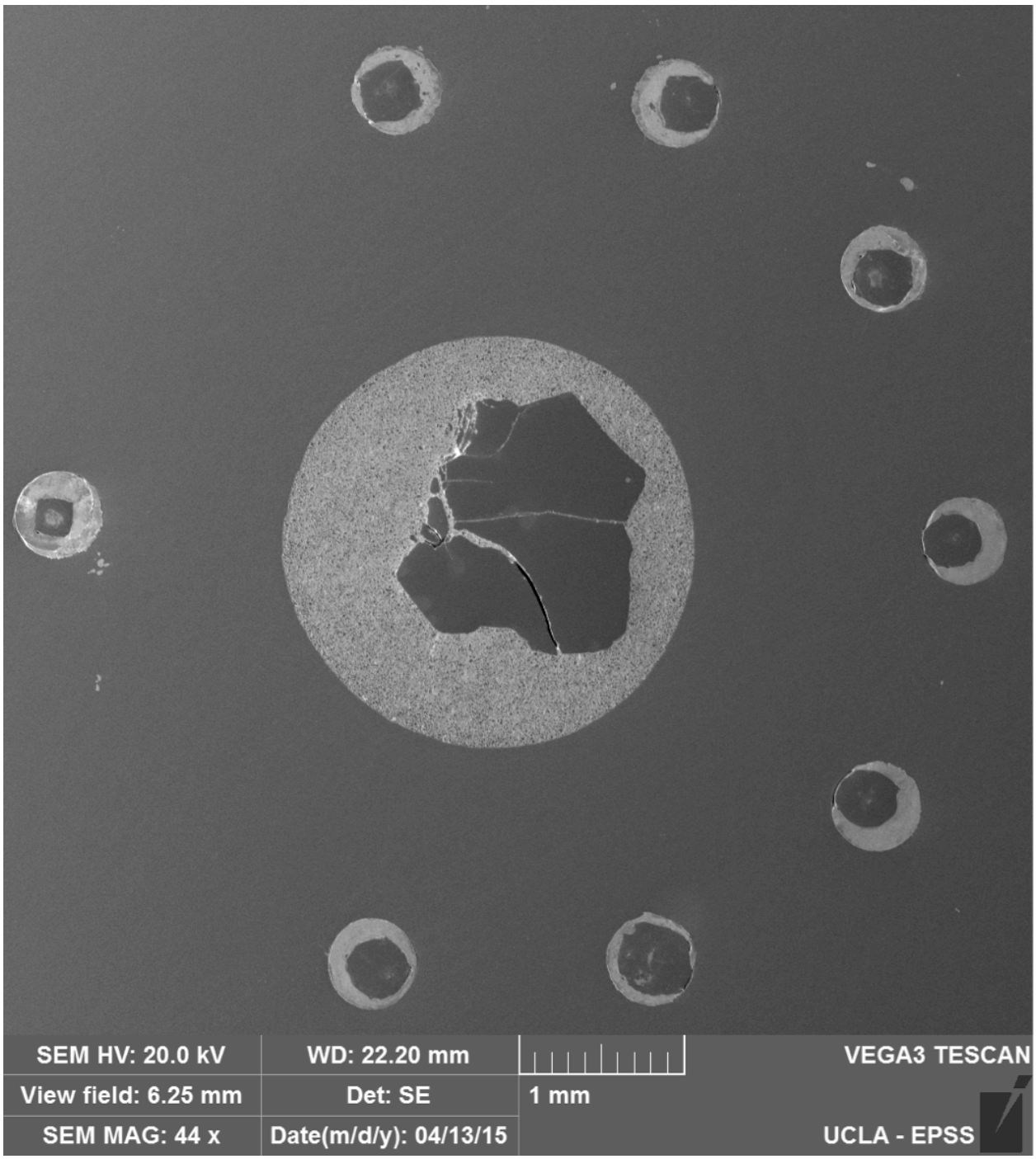

Fig. 2.5: SEM image of C2102N,1 crater residue mount. Seven flattened foils containing San Carlos olivine residues surround a polished San Carlos olivine crystal; the flattened Stardust crater is mounted in an eighth hole, isolated from the standard craters.

Chapter 3: Hypervelocity Impact Experiments

Introduction: Material from hypervelocity (> 2-3 km s^{-1}) projectiles that cause impact craters in foils can be partially retained in the form of residue deposited along crater walls (Kearsley, Burchell, Horz, et al. 2006). These residues have been extensively studied on simulated hypervelocity shots and on exposed space hardware. Specifically, test shots were used to relate crater morphology to projectile density (Kearsley et al. 2007; Kearsley et al. 2008); the impacts were also used to calibrate a variety of analytical techniques, including transmission electron microscopy of cross sections of crater residues, Raman spectroscopy, time of flight secondary ion mass spectrometry (TOF-SIMS) (Burchell et al. 2008; Leitner et al. 2008; Leroux et al. 2008). Such experiments are essential for understanding and interpreting results obtained from measurements of Wild 2 samples. Calibration tests of particles fired at Al foils at ~6.1 km/sec have revealed a high level of survivability of impactor material; in many cases, original crystalline material is observed within crater residue. Focused ion beam (FIB) sample preparation technology has allowed cross-sections of craters containing residues to be removed and thinned to electron transparent TEM sections for mineralogical analysis via electron diffraction (Leroux et al. 2008). Such FIB cross-sections also provide a means to estimate the volume of residues provided within the crater.

Modeling Crater Residue Volume: Despite these comprehensive calibration experiments, what had not been previously demonstrated was whether such residues would preserve the oxygen isotopic composition of the impactor without modification due to kinetic fractionation effects, or

that such residue would be analyzable via SIMS. To understand the level of precision that could potentially be obtained by measuring the residues of impact craters in the Stardust foils using SIMS, I modeled the mass of material available for analysis as a function of crater diameter. Previous hypervelocity experiments have demonstrated that a soda lime glass sphere with a density of 2.4 g/cm^3 will form an impact crater with a diameter roughly four times the diameter of the projectile. For silicate materials, and at velocities comparable to the Stardust encounter velocity, the portion of the projectile that is retained within the crater post-impact is anywhere from 25-60%; for my calculations, I assumed 42% of the original impactor survives. From this modeled impactor mass, and assuming a forsterite composition, I determined the number of impactor oxygen 17 and 18 atoms that are present within a given crater size. By calculating the number of ions needed to be counted for a given precision, and taking into account ion probe counting efficiencies that are typical for the IMS 1270, the crater size needed for a given precision can be determined. Based on this calculation, there are 63 craters that would contain enough material for a $\delta^{17}O$ measurement with a precision greater than 2‰. In practice, material in actual samples may be more or less abundant than these calculations indicate, and some craters may have been the result of impact by sulfide or Fe metal grains which would not be useful for oxygen isotope measurements; but to a first approximation, this calculation indicated that precision O-isotope measurements of crater residues were possible using the IMS 1270, given the samples available.

Light Gas Gun Experiments: While precision oxygen isotope measurements of available Stardust craters were theoretically possible, there were still many unknown parameters to be investigated, including (but not limited to): matrix effects, isotope fractionation due to crater

topological effects, and possible kinetic isotope fractionation due to hypervelocity capture. Therefore, a crucial first step was to make $\delta^{17}O$ and $\delta^{18}O$ measurements of lab-produced impact crater residues created by firing a suite minerals with known initial oxygen isotope compositions into analogous foil targets at Stardust encounter velocities (~6 km/s). The analogue hypervelocity craters used in this study were produced at the light gas gun facility at the University of Kent at Canterbury (Burchell et al. 1999).

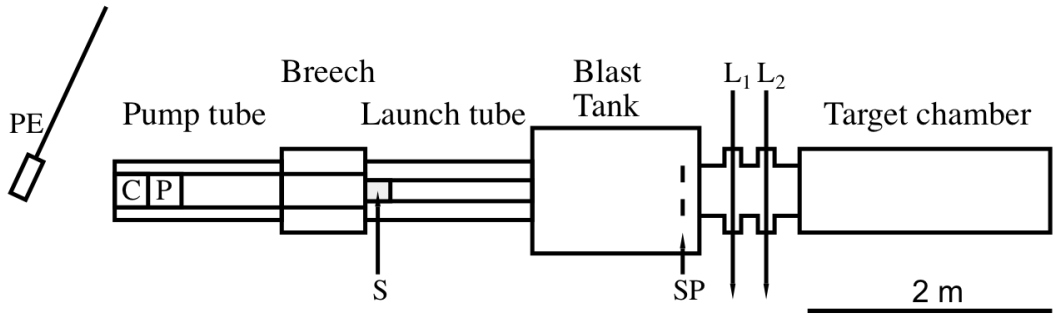

Fig. 3.1: Schematic diagram of the University of Kent light gas gun. (Burchell et al. 1999)

Foil targets shot with San Carlos olivine ($[Mg,Fe]_2SiO_4$) and olivine from the Admire pallasite were provided by Anton Kearsley in order to conduct preliminary SIMS experiments. I also visited the gun facility in 2011 to produce additional standard residues; crystals of Burma spinel ($MgAl_2O_4$), Afrique magnetite (Fe_3O_4) and olivine from the Eagle Station pallasite were ground into powders with grain sizes of ~10-100μm via agate mortar and pestle. Each powder was loaded into a four piece nylon sabot and shot into 1x1 cm^2 Al foil targets at ~6 km/sec. A portion of the spinel and magnetite powders were also shot into polished aluminum ion probe mounts to confirm observed fractionation effects were due to individual crater topology rather than large scale foil roughness.

The operation of the light gas gun is as follows: a powder charge is ignited, and accelerates a piston that compresses hydrogen gas contained in a pump tube; the gas ruptures an aluminum diaphragm and expands into a launch tube, accelerating the nylon sabot. The sabot exits the launch tube and separates in a blast tank, where it encounters a stop plate. The powder continues into a target chamber where it strikes a 1x1cm foil target (Al1145, temper 0 – the same composition as the foils used on the Stardust collector) at normal incidence, producing a buckshot pattern of crater impacts. Projectile velocity is measured independently via occultation of two laser curtains, as well as by deformation of the impact sensor attached to the stop plate. The blast tank and target chambers are cleaned after each shot by flushing them with air through a filtration system capable of trapping particles as small as 0.5 μm. While significant efforts are made to ensure most of the material impacting the foil target is comprised of the powder loaded into the nylon sabot, there exists the potential of contamination from the gun (gun powder residue, material from previous shots, etc.).

We analyzed ~5 craters from each shot using energy dispersive spectroscopy to confirm residues had compositions that matched the corresponding standard mineral. SEM imaging and EDS analysis of craters from the San Carlos olivine shot revealed fine-scale carbon nanotubes lining the craters (Figure 3.2). Carbon nanotubes can exhibit hydrophilic behavior (Wang et al. 2007), potentially complicating suppression of the $^{16}OH^-$ interference at mass 17. In practice, the mass resolution used was sufficiently high that, in combination with use of a liquid-nitrogen cooled trap surrounding the sample holder, the $^{16}OH^-$ was cleanly resolved and less intense than the $^{17}O^-$ peak.

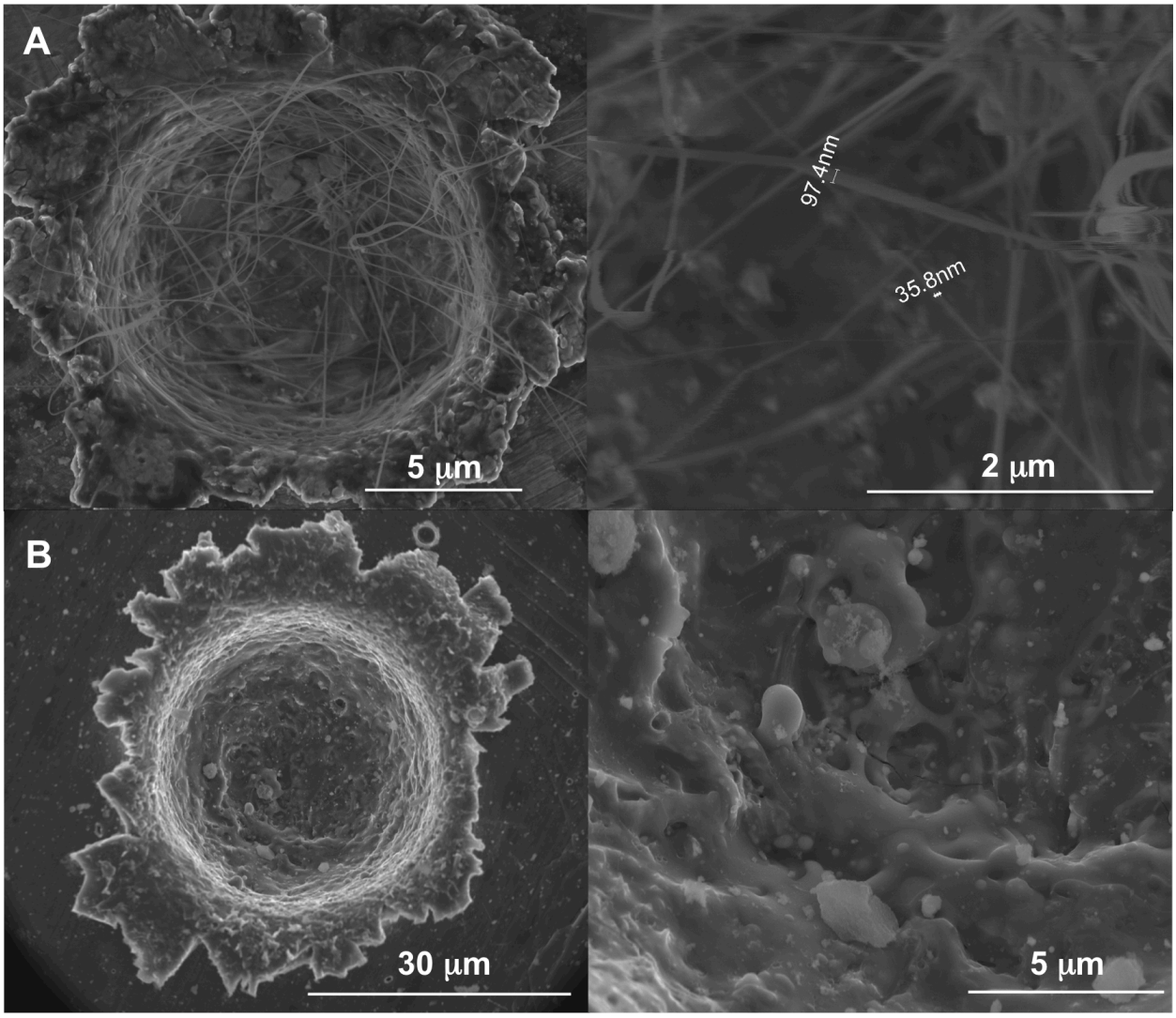

Fig. 3.2: A) Extreme case of carbon nanotube contamination in San Carlos olivine crater shot. B) More typical result of light gas gun shot.

Technique Development: I developed analytical and mounting techniques between February 2011 and November 2013, with 19 standard crater mounts produced and >80 standard craters sputtered.

Crater flattening: Initial experiments were conducted to evaluate the viability of O-isotope measurements of unmodified craters using foils provided Anton Kearsley. A $^1/_4$" diameter disk

was punched from the Admire olivine foil target and mounted on a 1" aluminum ion probe mount. Si and O ion imaging of craters demonstrated successful extraction of ions from the crater cavity; however, fractionation effects varied unpredictably by as much as several percent, and were attributed to the foil surface topology. In an effort to minimize large-scale topographic effects, custom ion probe mounts were made specifically for crater residue analysis. Individual craters with diameters ranging from 20-100 microns were cut from foil targets using a single edged razor blade, producing cubes with widths approximately 3-5x the crater diameter. These were placed in crater residue mounts described above; two such mounts contained San Carlos olivine craters, and a third contained craters from the Admire foil target. Despite this effort, $^{18}O/^{16}O$ oxygen isotope ratios still varied by as much as 35‰ relative to the mineral standard, with ~20‰ variability between individual crater analyses. A fourth mount was made and included eight flattened craters from the San Carlos olivine foil target; craters cut from foil targets were trimmed into inverse trapezoidal prisms (i.e. truncated pyramids) rather than cubes. Each foil prism was then placed between two cleaned circular 1" diameter thin section slides and carefully flattened by applying pressure to the slide edges in a rolling motion. This flattening technique, combined with the trapezoidal prism shape of the foil, resulted in the contents of the crater becoming preferentially raised and exposed without the crater rim obscuring the residue. $^{18}O/^{16}O$ oxygen isotope compositions of residues in this mount varied by 5‰ relative to the San Carlos olivine standard, with comparable reproducibility, demonstrating the necessity to flatten craters for precision oxygen isotope analysis. Two additional mounts containing San Carlos olivine and Admire olivine were prepared in a manner similar to Mount 4 and analyzed during a subsequent ion probe session; $^{18}O/^{16}O$ measurements yielded similar 5‰ variations between the residues and mineral standards.

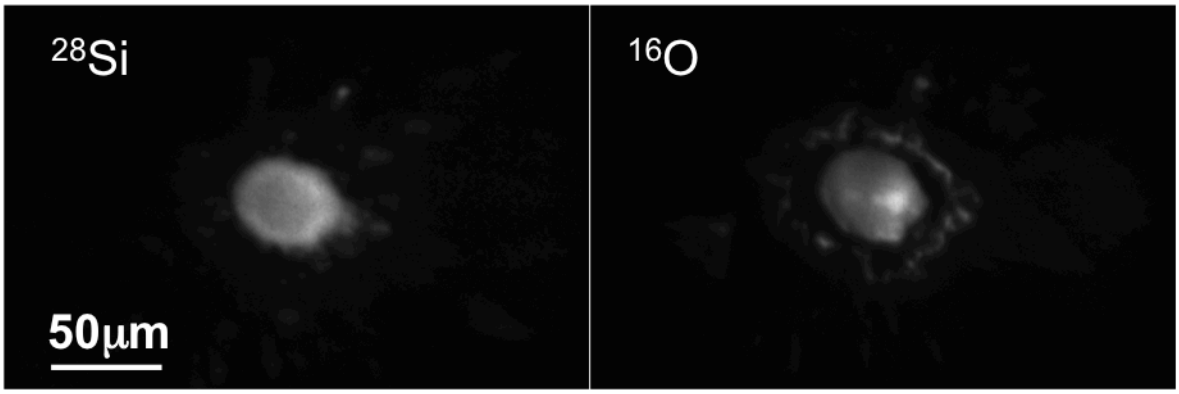

Fig. 3.3: Silicon and oxygen ion images of Admire olivine crater residues.

Preparation of the crater mounts involved placing flattened craters into holes that were pre-filled with indium, covering the mount with a 1" diameter thin section slide, and applying pressure from the backside of the mount such that indium would surround the flattened foil. During this operation, foils would sometimes become dislodged and folded during flattening; other times, the glass slide would shift translationally, dislodging residue and causing deep scratches in the foil surface. Due to these complications during mount preparation, only ~60% of mounted craters were suitable for SIMS on early mounts (mount 1 - mount 7). To ensure a higher success rate in crater mounting, a jig was developed that restricted lateral motion of the thin section slide such that flattened foils could be mounted into the indium-filled holes under a stereomicroscope; this jig improved the foil mounting success rate to 100% (i.e. all foils mounted after Mount 7 were suitable for SIMS analysis).

Analytical conditions: The primary beam current was selected to ensure a stable, consistent count rate during the analysis of the crater residues. Highly focused and intense primary beams sputtered rapidly through the tenuous residue such that sputtering equilibrium could not be

achieved before being completely ablated. The primary beam was initially defocused to sputter a ~30μm area; this condition produced the most precise data for our standard mineral residues. Rastering a focused (5μm), low current (0.5nA) primary ion beam produced the most consistent sputtering conditions for craters, which was preferred over the defocused beam for analysis of fragile, fine-grained Stardust residues despite resulting in a slightly greater dispersion of standard crater isotope values.

Typically material is sputtered for several minutes before data are collected to ensure sputtering equilibrium has been achieved; however, the thickness of impact residues can be variable from crater to crater, and for fine-grained components it is possible to sputter the sample completely during pre-sputtering, before any data is collected. Therefore, for crater residue analyses, we counted all sputtered secondary ions, and sputtering equilibrium was determined via change-point analysis (Team 2013) of the $^{18}O/^{16}O$ ratios.

Detectors were initially configured for measurement of ^{16}O and ^{18}O ions using the L'2 and H'2 Faraday cups. Below count rates of 10^6 c.p.s., thermal fluctuations in the F.C. resistor detrimentally affect precision; since ^{16}O is 500 times more abundant than ^{18}O, primary ion beam intensities had to be sufficiently high (3-5 nA) to produce ^{16}O count rates $>10^9$ c.p.s. from crater residues.

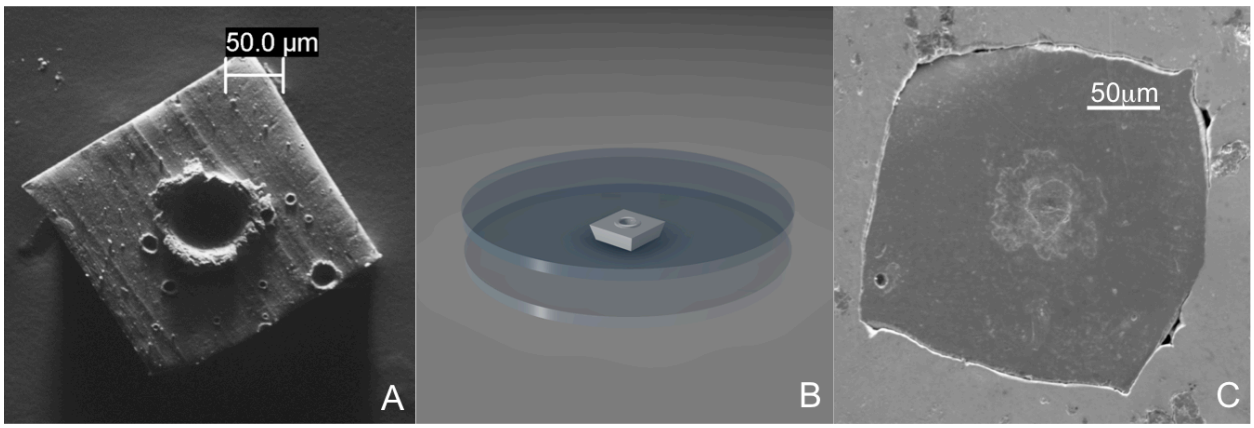

Fig: 3.4: Crater flattening procedure. A) Craters are isolated in prism-shaped blocks of foil. B) Foils are flattened between two 1" thin-section slides. C) flattened foils are pressed into indium-filled well on ion probe mount.

The detector configuration was modified in subsequent analytical sessions with the C Faraday cup positioned at mass 16, the axial electron multiplier at mass 17 and the H2 electron multiplier positioned at mass 18. A 0.5-0.7 nA primary beam was used, resulting in secondary count rates of $1x10^8$ for ^{16}O, $2x10^5$ for ^{18}O and $5x10^4$ for ^{17}O. A count rate of 200,000 c.p.s. was somewhat high for the H2 EM, and aging was observed during analytical sessions; however, this effect was linear in time and could be compensated by standard-sample bracketing.

Results for the oxygen isotope measurements of San Carlos olivine, Burma spinel, Eagle Station olivine and Afrique magnetite residues, made during five analytical sessions from August 2013 to July2015, are shown in table 3.1 and figure 3.5. All residues are fractionated mass-dependently towards lighter isotope values relative to their mineral counterparts. San Carlos olivine and Eagle Station olivine residues were shifted by 1.5-2.5 per mil per amu; Burma Spinel residues exhibited a 3.5-4.5 per mil per amu fractionation, and Afrique magnetite residue compositions were shifted by 3.5-5 per mil per amu. This observed fractionation of the residues

may be a kinetic effect resulting from the hypervelocity capture, vaporization and redeposition of the impacting particles. TEM data of Stardust crater residues and light gas gun experiments (e.g. Leroux 2008) show that silicate material impacting Al foil at 6 km/sec result in peak pressures less than 100GPa; those pressures, combined with the quenching of the residue due to the thermal conductivity of the foil, tend to produce melt glasses with occasional preserved mineralogy, rather than vapor condensates.

Standard Mineral	Analytical Session	$\delta^{18}O_{standard} - \delta^{18}O_{crater}$ (‰)	$\delta^{17}O_{standard} - \delta^{17}O_{crater}$ (‰)
San Carlos olivine	August 2013	3.3 ± 0.2	1.8 ± 0.3
	November 2014	2.8 ± 0.7	0.3 ± 0.5
	April 2015	5.5 ± 1.0	2.1 ± 0.6
	July 2015	5.4 ± 0.9	2.2 ± 0.3
Eagle Station olivine	April 2014	4.1 ± 0.6	1.7 ± 0.7
Afrique magnetite	April 2014	10.2 ± 1.4	3.1 ± 0.6
	November 2014	7.3 ± 1.4	2.1 ± 1.2
Burma spinel	August 2013	7.0 ± 1.7	3.4 ± 0.7
	July 2015	8.6 ± 0.8	3.4 ± 0.3

Table 3.1: Differences between crater residue and mineral oxygen isotope compositions during analytical sessions. Errors reported are 1 s.e.

Another possibility is that the observed shift is the result of a matrix effect between the melt glass and the corresponding unmelted mineral. Matrix effects of up to 5‰ between minerals and glasses have been observed (Eiler et al. 1997), though under conditions of extreme energy filtering. The consistent nature of this fractionation effect for compositionally similar mineral species allows to use the lab-produced impact craters as standards to correct for instrumental mass fractionation effects in our Stardust impact crater standards, as long as the approximate composition of the melt residue is known prior to SIMS analysis.

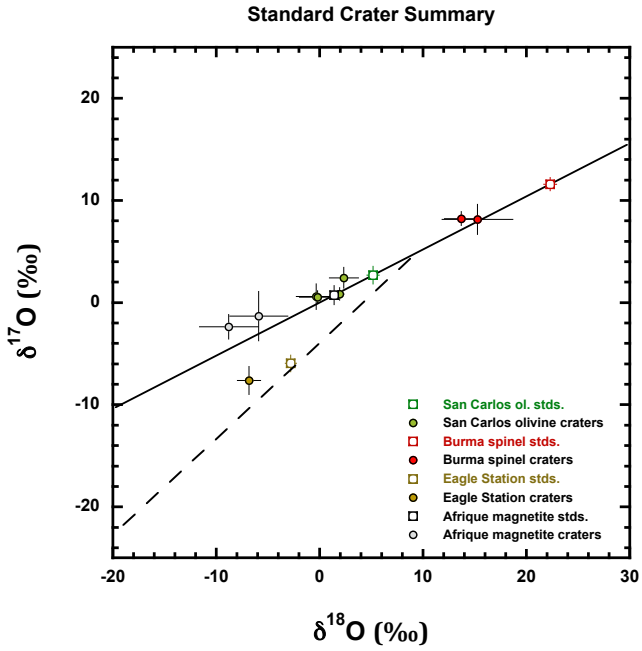

Fig. 3.5: Summary of standard crater residues used to normalize Wild 2 craters

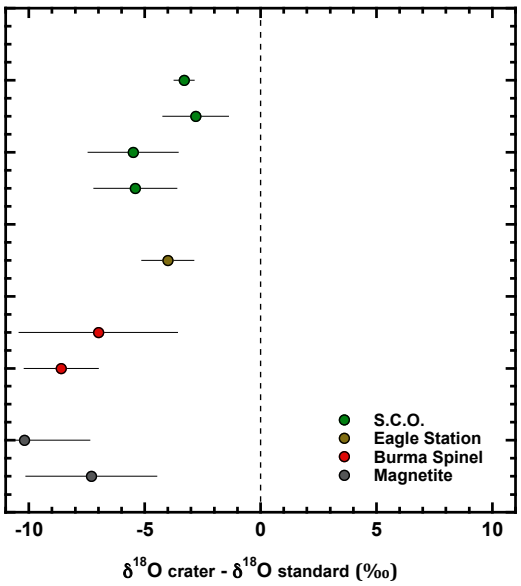

Fig.3.6: $\delta^{18}O$ differences between standard crater residues and mineral counterparts.

Chapter 4: The Samples

Stardust Crater Nomenclature: Stardust foils are named based on their locations relative to associated aerogel tiles in the sample tray, with designations "N" and "W"; for example, C2049N,1 indicates the comet facing foil strip located north of the aerogel tile C2049. The last digit following the direction represents the number of divisions made of the original foil. Larger foils used to mechanically remove the aerogel tiles from the aluminum frame are given a designation "0" identifying them as the primary parent foil. The comet exposed areas of foil were cut from the collector using a custom designed twin rotary cutter, which produced strips of Al foil ~1.7mm wide, and 13-34mm in length from the parent foil prior to aerogel tile removal; these strips of foil are given the designation "1". Subsequent foil divisions are given designations "2", "3", etc. Individual Stardust craters are named after their associated foils, and henceforth the names will refer to the impact craters, rather than the associated foils.

Composition and Morphology: Fifteen foils containing a total of thirteen Stardust craters were received in three separate allocations over a four year period from Johnson Space Center's Astromaterials Curation facility. Craters for this study ranged in diameters from 20-90μm (as measured from the crater top lip), with most being in the 30μm range. Depth measurements as determined by stereo imaging and depth modeling were determined for four of the craters. EDS analyses were performed on all craters, and X-ray maps were obtained for all but two craters (C2122W,4 and C2067N,3). X-ray spectra were dominated by aluminum resulting from the foil substrate. The high aluminum peaks were included in reported spectra, but were subtracted from

compositional totals. Any indigenous aluminum in the crater residue was therefore not obtained, even though Al may have been present in significant quantities in some samples.

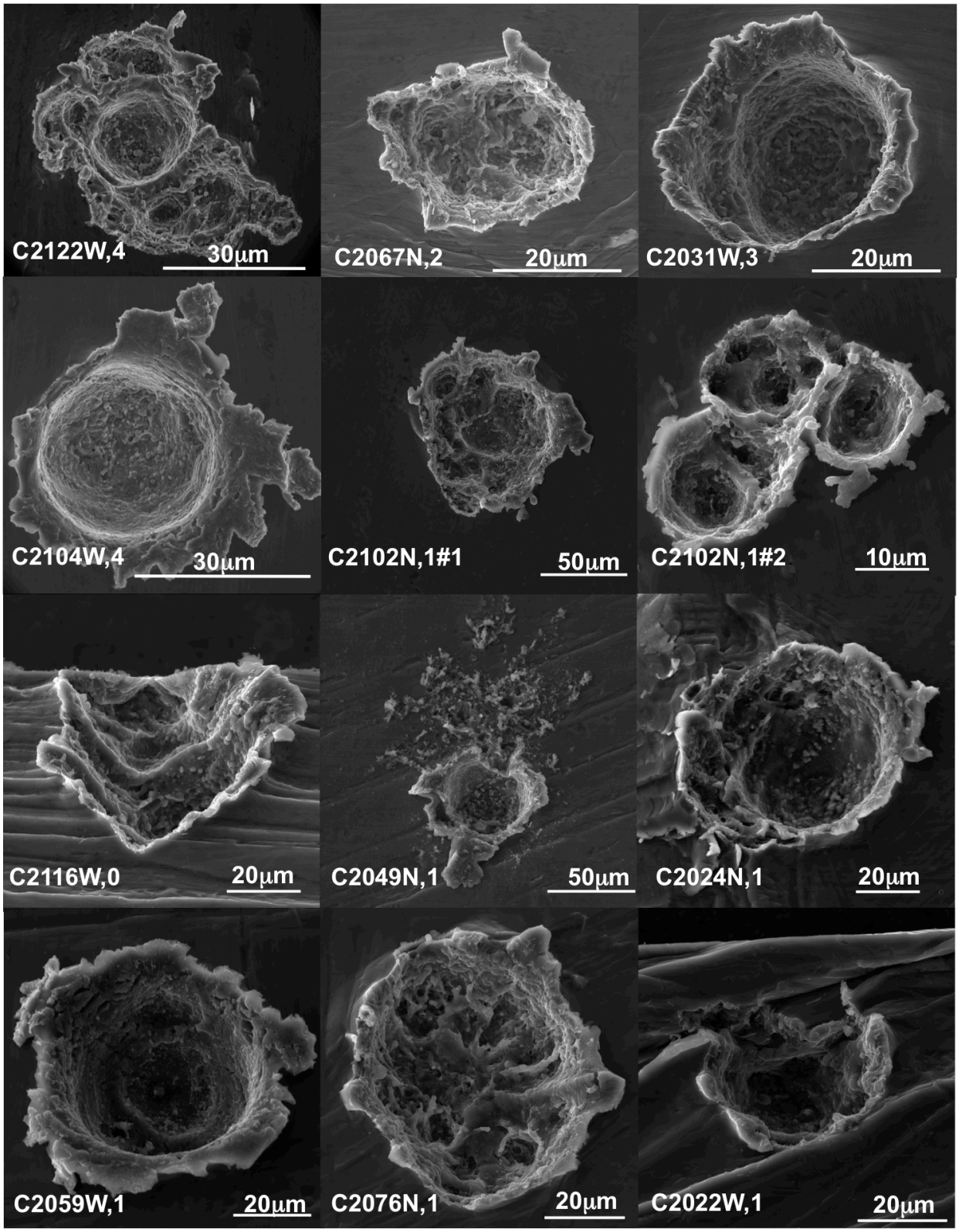

Fig. 4.1: Twelve allocated Wild 2 craters prior to analysis via SIMS

Crater Name	~ Crater Dia. (μm)	~ Projectile Dia. (μm)	~ Particle Mass (ng)	Morphology	Mg/Si	Comments
C2067N,3	25	5	0.2	complex	1.7	Mg-rich olivine
C2122W,4	40	8	0.9	complex	4.8	possible spinel?
C2031W,3	34	6.8	0.5	bowl shaped	2.4	Mg-rich olivine/Ol-Px mix
C2104W,4	40	8	0.9	bowl shaped	n/a	Fe-Ni sulfide, minor Ca-Px
C2102N,1#1	80	16	6.9	complex	1.4	Ol-Px mix plus FeS
C2102N,1#2	10	6	0.4	complex	1.6	Ol-Px mix plus FeS
C2116W,0	n.d.	n.d.	n.d.	complex/simple	2.3	Mg-rich olivine + spinel?
C2049N,1	50	10	1.7	complex	0.5	silica/GEMS rich?
C2024N,1	50	10	1.7	complex/simple	0.9	Mg-rich pyroxene
C2059W,1	60	12	2.9	bowl-shaped	1.6	Mg-rich olivine
C2076N,1	60	12	2.9	complex	1.8	Mg-rich olivine + FeS
C2022W,1	30	6	0.4	bowl shaped	2.9	Mg-rich olivine + spinel?
C2095W,1	110	22	17.8	bowl-shaped	n/a	Pure Fe/Ni metal

Table 4.1: Summary of Wild 2 crater residue physical and compositional measurements

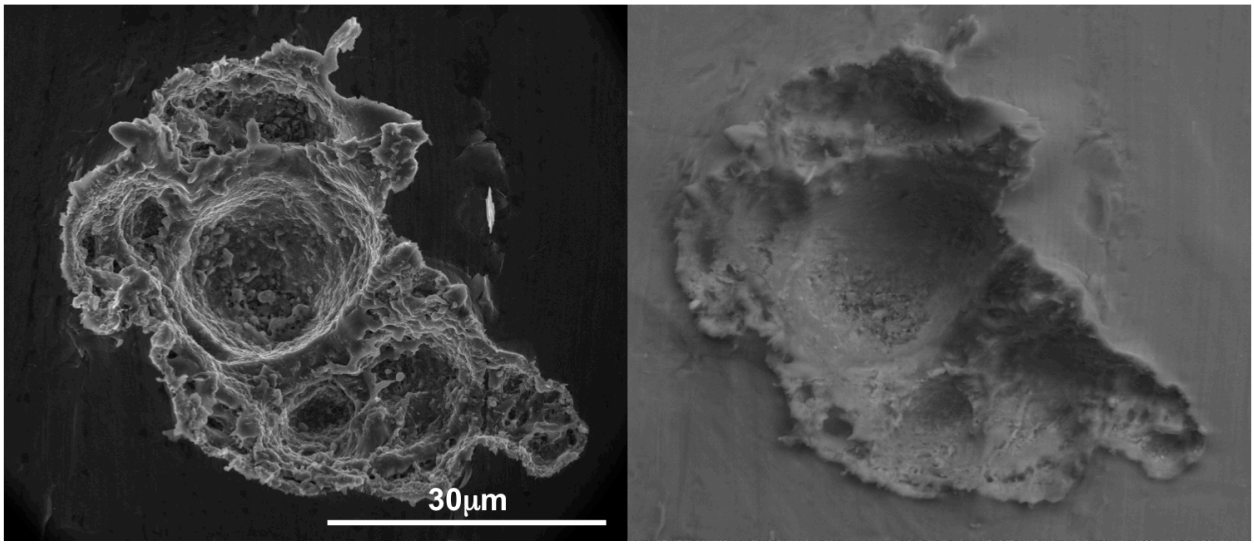

Fig. 4.2: Secondary electron and backscatter image od C2122W,4.

C2122W,4: This foil contained a 40μm wide impact crater with complex morphology, with multiple overlapping impact features dominated by a 20μm diameter, 12 μm deep central bowl-shaped depression; submicron impact craters can be observed nested within larger impact features. Light gas gun experiments (Kearsley et al. 2008) have demonstrated that craters composed of overlapping individual impact features with non-uniform size distributions are

likely produced by weakly bound, high porosity cluster of grains (such as what is observed in CP-IDPs). Impact EDS spot analysis on several areas of this impact feature reveal a composition dominated by Mg, Si, O, Fe and S, with an Mg/Si ratio of ~5, indicating a possible mixture of Mg-rich olivine, spinel, and FeS. EDS maps revealing possible compositional heterogeneity were not obtained for this crater.

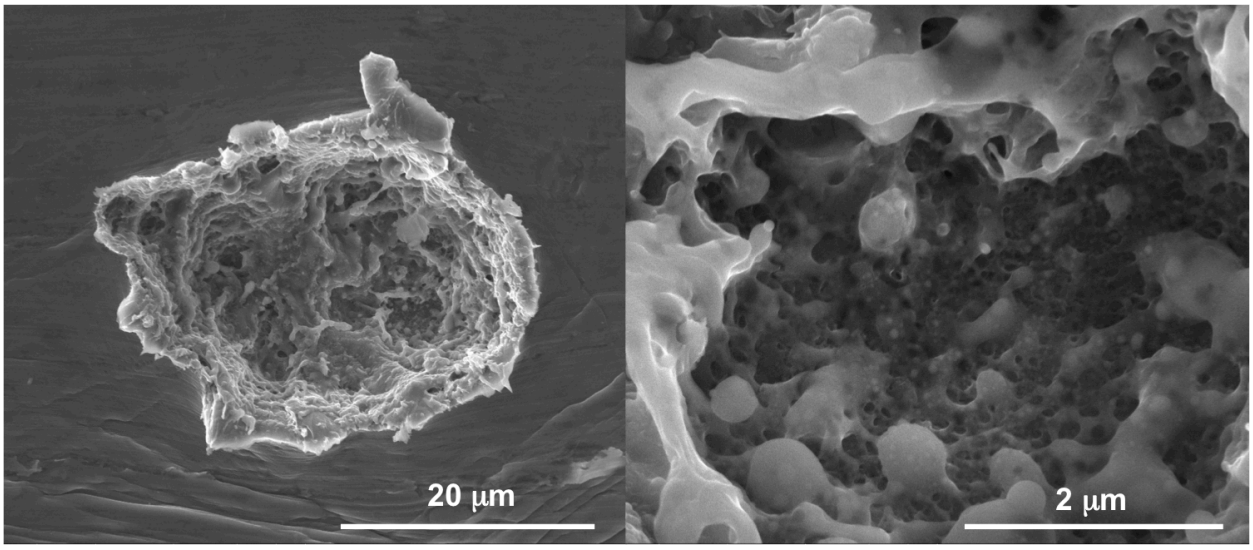

Fig. 4.3: Secondary electron image of C2067N,3.

C2067N,3: A 30μm impact feature with complex morphology was found on this foil. The low crater depth/crater diameter ratio of this feature suggests a low density/high porosity impactor. Melt glass with submicron vesicular structure was abundant on the crater floor; material with preserved mineral structure was not observed. Unlike the feature found in C2122W,4, this crater does not appear to have included large, high-density monomineralic impactors; the feature more closely resembles the laboratory-produced crater resulting from impact by an artificial aggregate particle (fig. 24b of Kearsley 2008). Such structure may indicate a high-porosity impactor dominated by fine-grained material. EDS spot analyses of this crater revealed a Mg/Si ratio of ~2, suggestive of a Mg-rich olivine composition; Fe and S were also present. As

with the crater on foil C2122W,4, spectral maps were not obtained for this crater.

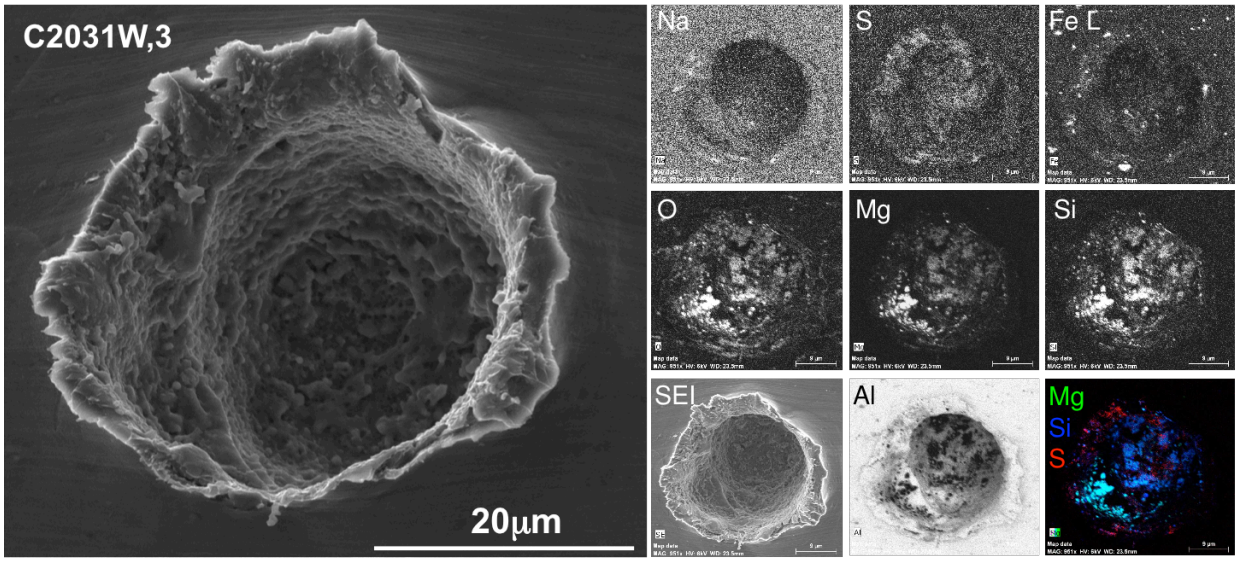

Fig. 4.4: SE image and x-ray maps of C2031W, 3 (image courtesy of Anton Kearsley, NHM).

C2031W,3: This foil contained bowl shaped, 35µm crater with a depth of 35 µm, indicating a relatively high density impactor. The crater appears to contain a shallow shelf to the side of the otherwise bowl-shaped crater. EDS spectra and mapping reveal olivine/pyroxene compositions, with the residue at the bottom of the crater containing lower Mg/Si ratios than the residue located on the shelf of the crater. Fe and S are also present in small quantities. The composition and morphology of this crater may be the result of an impact by a twinned olivine crystal with loosely adhering minor fine-grained material.

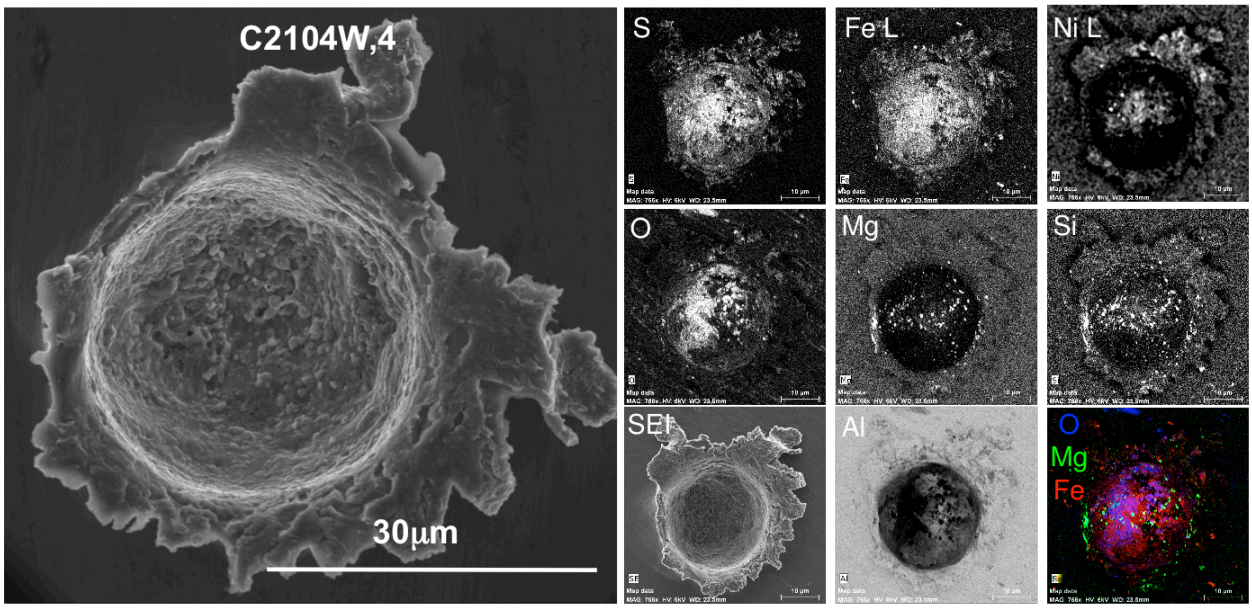

Fig. 4.5: SE image and x-ray maps of C2104W,4 (image courtesy of Anton Kearsley, NHM).

C2104W,4: A deep, 40µm bowl shaped crater was located on this foil. The relatively high crater depth/crater diameter ratio resulted from an impact of a low porosity, high density projectile. EDS maps show a residue dominated by Fe, S, with trace amounts of pyroxene along the crater lip. Oxygen is abundant, and present beyond relation to the Mg, Si, and O spots; elemental maps reveal it is somewhat heterogeneously associated with the Fe-Ni-S residue, and might have been the result of post-capture oxidation of the residue.

C2102N,1: This foil contained two distinct impact features separated by ~300µm. These two craters were previously analyzed via TOF-SIMS for elemental and organic composition, the results of which are reported in Leitner et al. 2008. For consistency, their naming convention has been adopted in this work; that is; the larger crater is referred to as C2102N,1 #1, and the smaller feature is referred to as C2102N,1 #2, with three sub-craters labeled 2.1, 2.2, and 2.3.

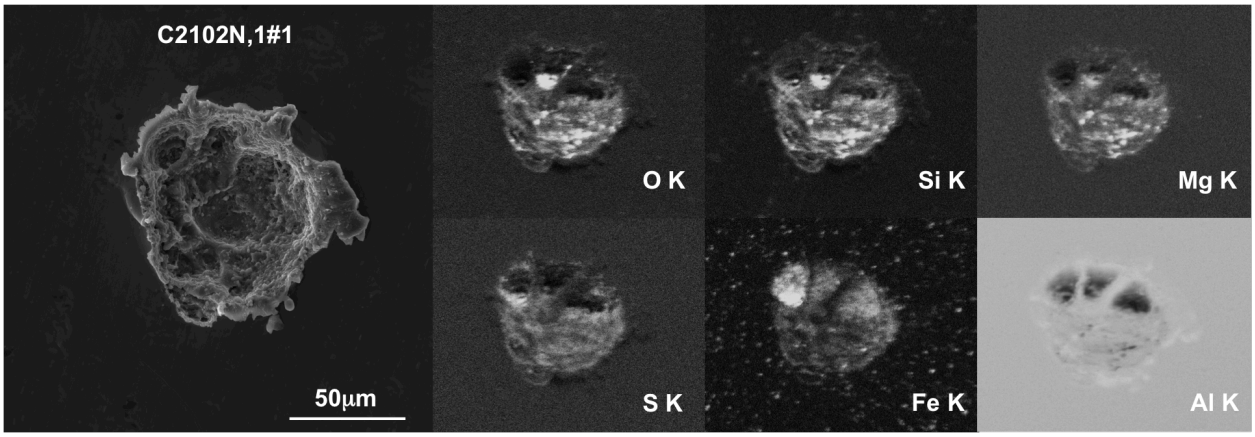

Fig. 4.6: Secondary electron image and X-ray maps of C2102N,1#1.

#1: This crater was the largest analyzed in this study, with an overall diameter of ~80μm. This crater exhibits complex morphology consisting of numerous overlapping depressions. EDS spectra show a residue dominated by olivine/pyroxene composition and Fe and S minor components, with an Mg/Si ratio of 1.2-1.4. EDS maps reveal a compositionally heterogeneous distribution of the crater residue, with high abundances of FeS/Fe metal in one of the larger sub-crater depressions, and abundant Mg, Si, and O residue distributed along the more shallow portion of the crater, as well as in a deep depression adjacent to the Fe/FeS sub-crater. This crater may be explained by impact of a porous aggregate of coarse, dense single minerals and fine-grained material of roughly chondritic composition.

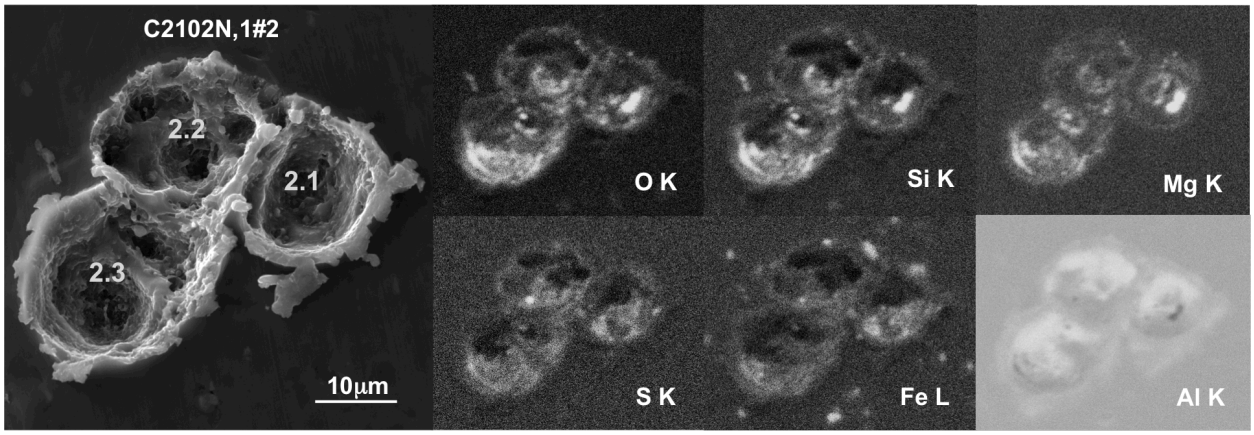

Fig. 4.7: Secondary electron image and X-ray maps of C2102N,1#2.

#2 – The impact feature found on this foil consists of three conjoined craters with diameters of ~10-15 μm each; the individual craters exhibit complex morphologies and overlapping depressions that are suggestive of impacts from smaller sub-fragments of the original projectile. The average Mg/Si ratio for this feature as measured by EDS is 1.6, which is comparable to the ratio determined in the TOF-SIMS analysis (Leitner et al. 2008); strong Fe and S peaks were also observed. Spectral maps show a heterogeneously distributed residue, with concentrations of Mg, Si and O in craters 2.1 and 2.3. This triad of craters was likely formed by a weakly adhering cluster of high density Mg-rich olivines with a minor component of attached Fe/FeS and chondritic composition material.

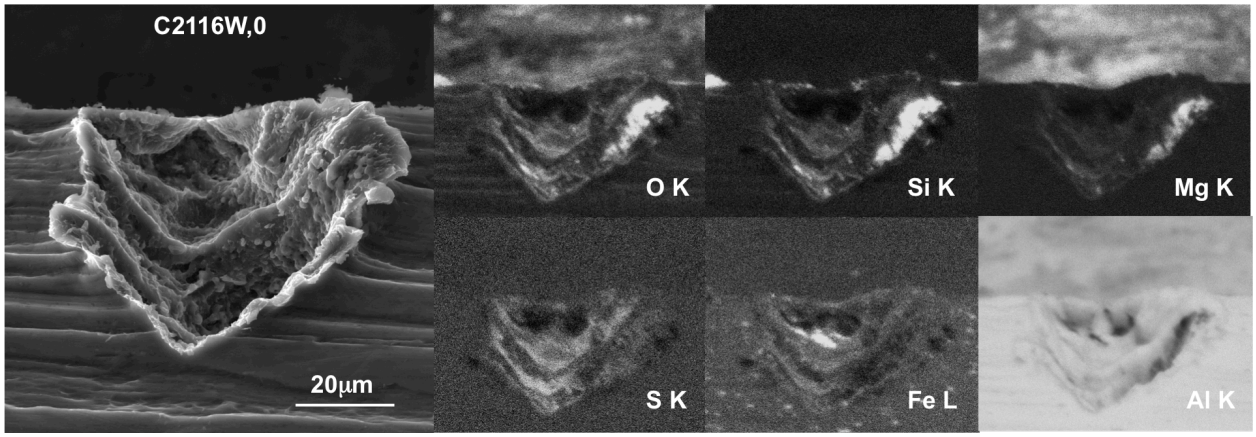

Fig. 4.8: Secondary electron image and X-ray maps of C2116W,0.

C2116W,0: This crater was partially damaged by the foil-cutting process prior to the extraction of the adjacent aerogel cell. Because of this partial damage, morphological features cannot definitively attributed to impactor characteristics. What remains of the crater is approximately 50μm across and has a complex structure. EDS spectra reveal a high Mg/Si ratio of 2.2, with prominent Fe and S peaks. X-ray maps show a heterogeneously distributed residue of silicate material, which is concentrated to one side of the crater; Fe is located deeper towards the central region of the depression. This feature may have been formed by an Mg-rich olivine projectile with adhering Fe/FeS grains and a minor spinel component contributing the excess Mg.

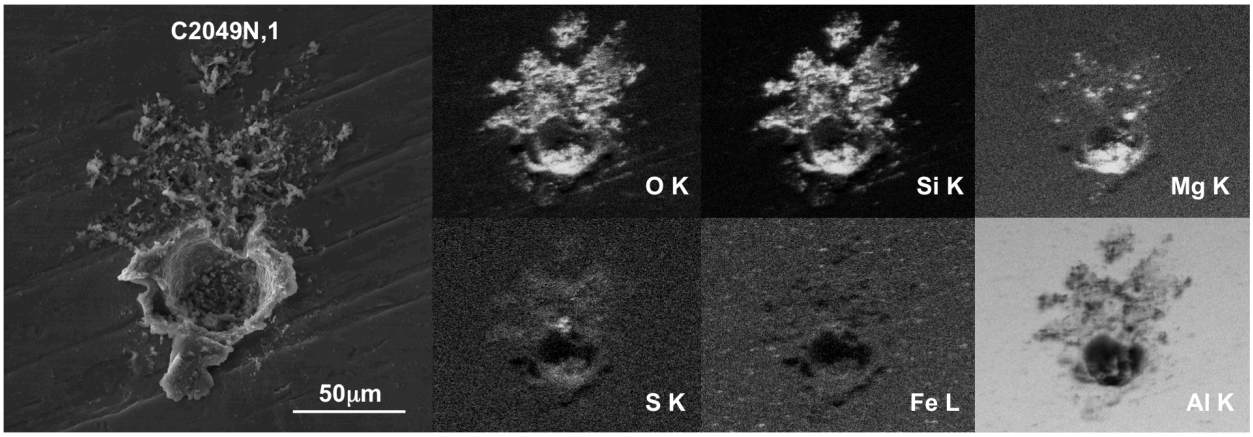

Fig. 4.9: Secondary electron image and X-ray maps of C2049N,1.

C2049N,1: This foil contained an impact feature unique in our allocation. A 50μm crater with a roughly hemispherical shape was immediately adjacent to a field of black, partially melted debris (as observed at 50x under an optical microscope). SEM images revealed numerous particles with fine-grained botryoidal texture; many craters between 1-5μm in diameters were observed in association with the debris field. Both the residue within the craters and the adjacent field have an Mg/Si ratio of 0.4-0.5 and a O/Si ratio close to 1, as measured by EDS; Fe and S are also present in trace amounts. X-ray maps show O, Si and Mg strongly correlated with residue within the bowl-shaped crater; the debris field contains O and Si, with very small amounts of

associated Mg. One S hotspot appears on the top edge of the large crater, on the boundary with the adjacent field (fig. 4.9).

Due to the uniqueness of this impact feature and the destructive nature of SIMS analyses, the crater was bisected into two halves, with the lower portion of the bowl shaped crater being mounted and prepared for oxygen isotope measurements, and the upper portion being preserved for more detailed chemical and possible mineralogical analyses by TEM. If any of the fine-grained particles were only partially unmelted (or perhaps even completely intact), it would represent the only such particles in the Stardust collection, and might provide some insight into whether GEMS grains were present in Wild 2 dust.

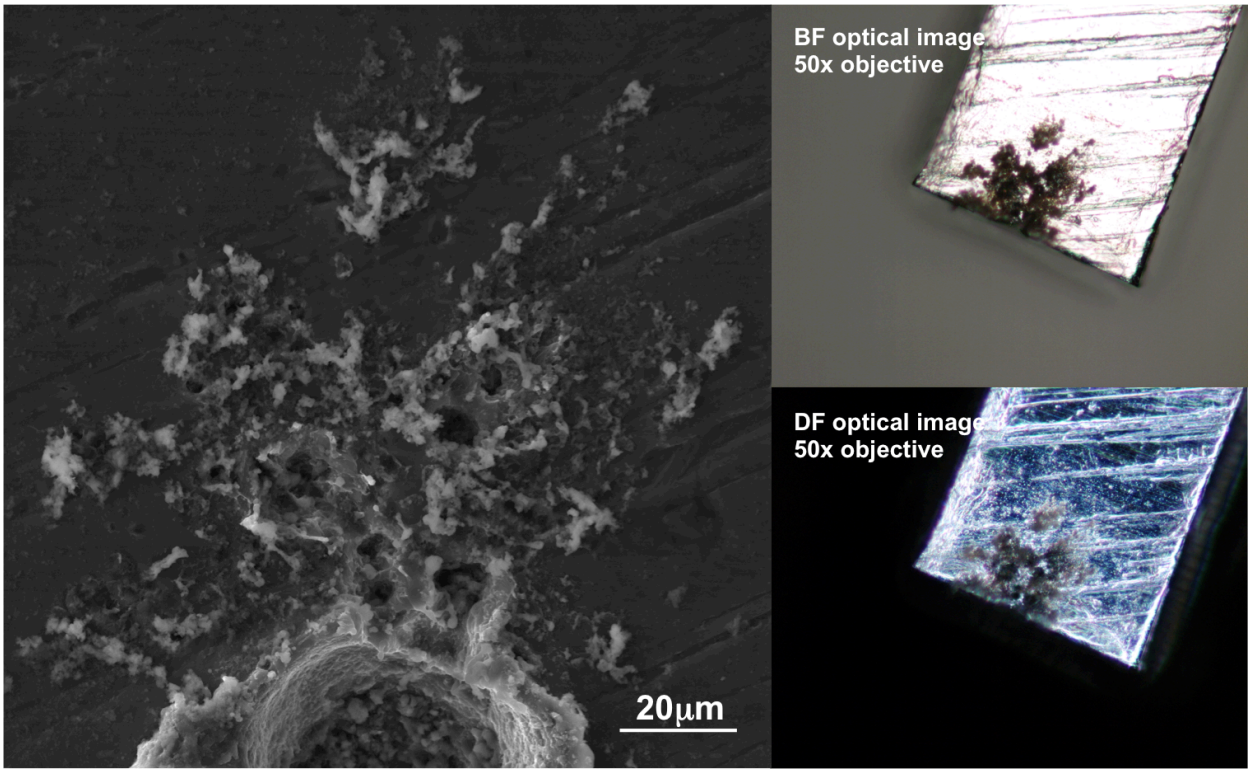

Fig. 4.10: Secondary electron, brightfield optical and darkfield optical images of C2049 upper debris field.

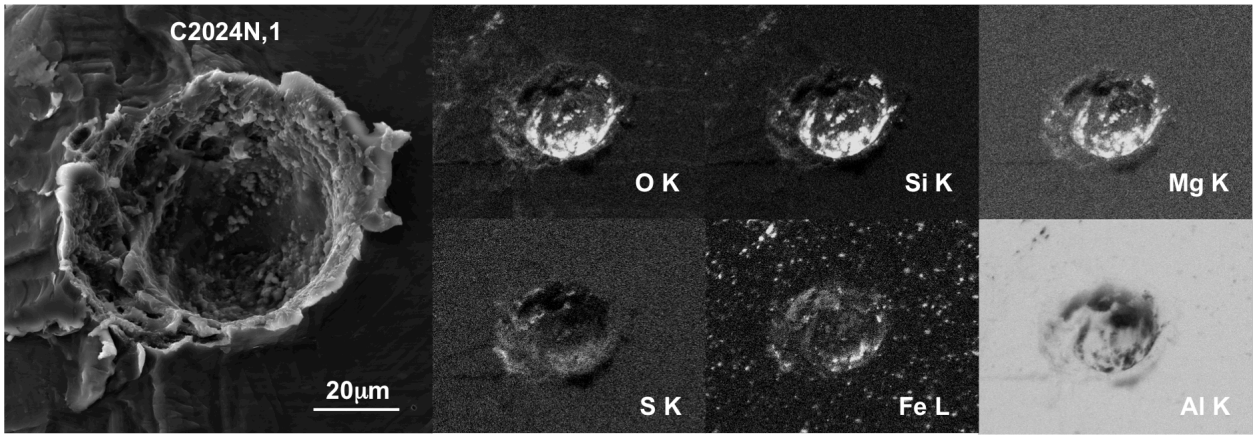

Fig. 4.11: Secondary electron image and X-ray maps of C2024N,1.

C2024N,1: A 50μm bowl shaped impact feature was found on this foil. A few 2-3μm sized craters can be observed along the crater rim, and a slight shelf is observed along one side of the bowl shaped depression. Strong Mg and Si peaks are revealed in the EDS spectrum, with an Mg/Si ratio of 0.9; Na, S and Fe were also present in the residue. X-ray maps show strong correlations between O, Si, Mg, S, and Fe. This crater may have been the result of impact from a predominantly monomineralic Mg-rich pyroxene with trace amounts of adhering fine-grained chondritic material.

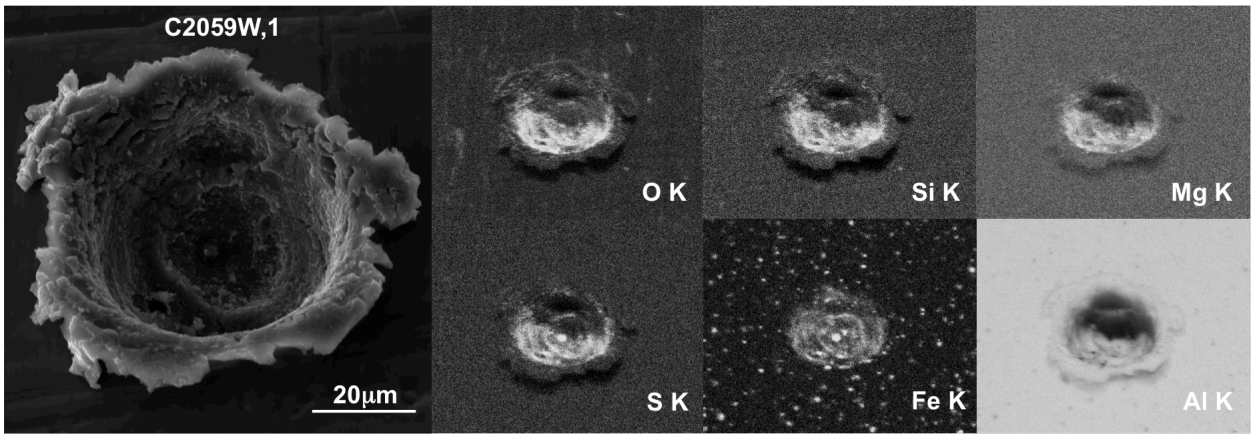

Fig. 4.12: Secondary electron image and X-ray maps of C2059W,1.

C2059W,1: This foil contained a 60µm bowl shaped crater, with at least one smaller 20µm depression observed on the primary crater floor. EDS spectra revealed and Mg/Si ratio of 1.6; Na, S and Fe were also observed in the spectrum. X-ray maps of this feature show a uniformly distributed ferromagnesian silicate residue, with an FeS spot in the center of the nested crater. Based on the EDS analyses and the crater morphology, we speculate this crater resulted from impact with a dust grain of olivine composition and adhering FeS minor components.

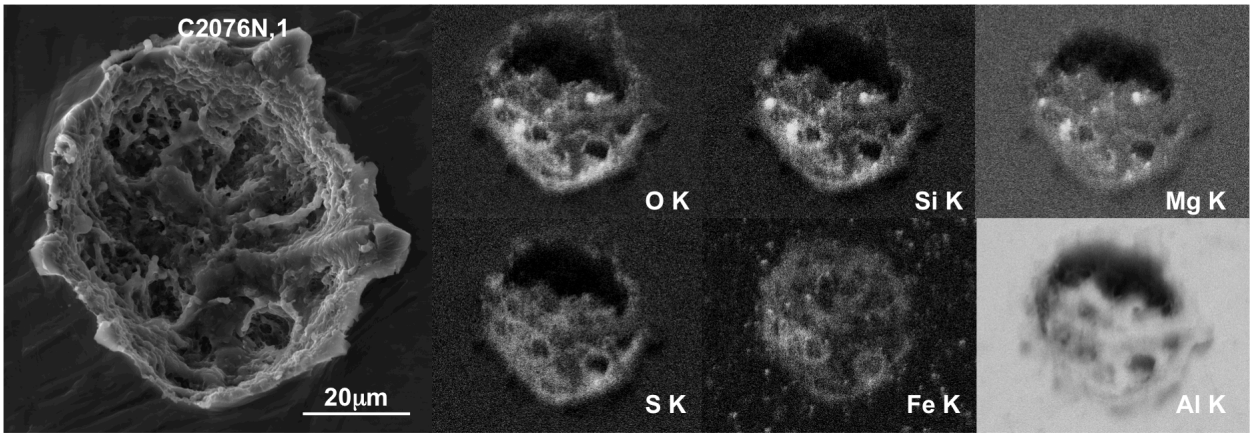

Fig. 4.13: Secondary electron image and X-ray maps of C2076N,1.

C2076N,1: A 60µm wide shallow depression was found on this foil. This feature exhibited complex morphology, and is comprised of numerous overlapping and nested craters. EDS measurements reveal an Mg-rich olivine stoichiometry and abundant Fe and S. X-ray maps show the residue to be relatively homogeneous in its elemental composition. The structure and shallow depth of this feature suggest it was formed by impact from a low density, high porosity projectile with fine-grained olivine and troilite composition.

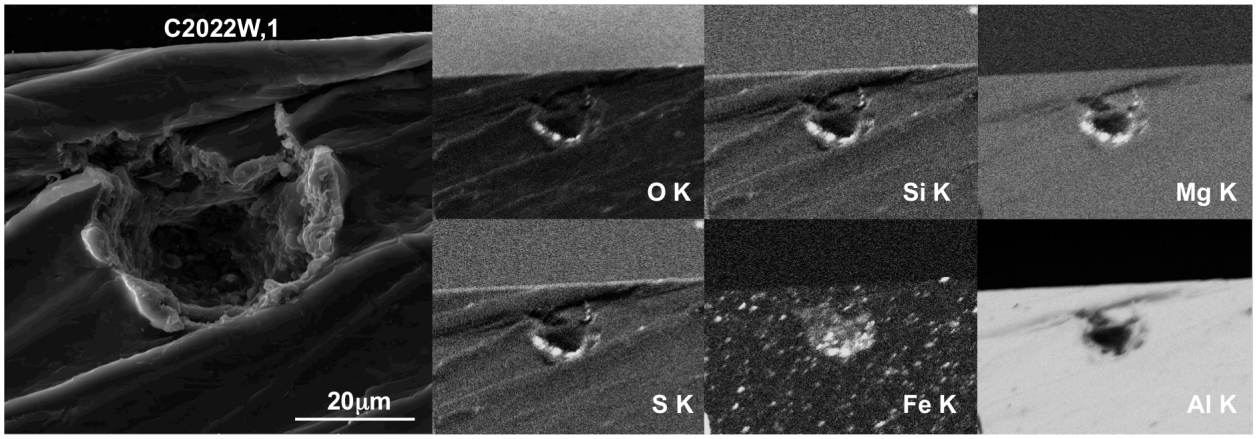

Fig. 4.14: Secondary electron image and X-ray maps of C2022W,1.

C2022W,1: A small, 25μm, roughly bowl-shaped crater was found near the edge of this foil. The feature appears to have been distorted by the rotary wheel cutter prior to aerogel tile extraction. The residue has a an Mg/Si ratio of 2.9 and a prominent Fe peak. X-ray maps of the residue show O, Si, Mg and S along the crater rim, with Fe appearing more abundant towards the crater floor. The depth of this crater and the composition of the residue implies formation via a low porosity, high (>3) density impactor with Fe-metal, olivine and possibly spinel components.

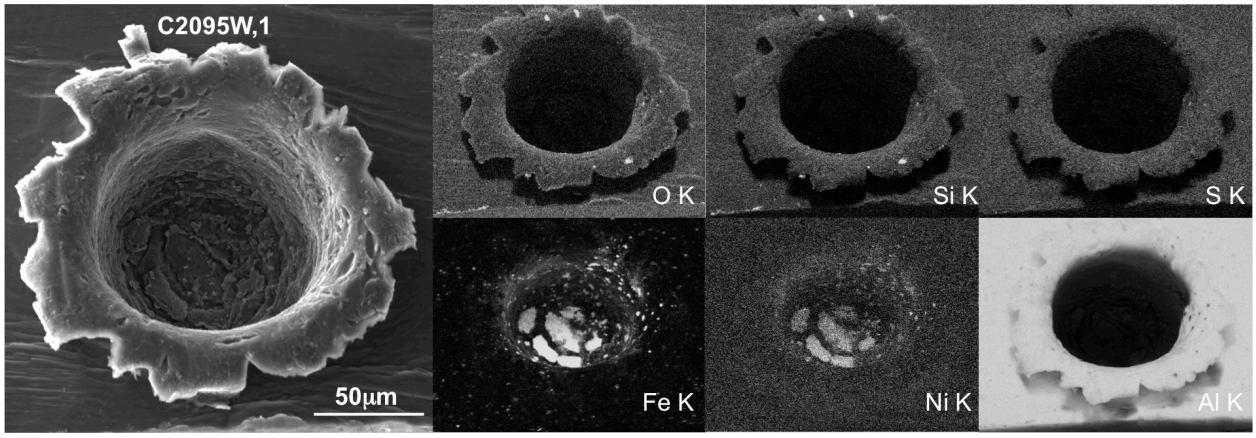

Fig. 4.15: Secondary electron image and X-ray maps of C2095W,1.

C2095W,1: This foil contained a deep, 110μm bowl-shaped feature, indicating formation by a

high density impactor. EDS spectra and maps show a residue with a pure Fe/Ni composition on the crater floor. Since the objective of this study was to obtain oxygen isotope compositions of Wild 2 dust, no further analysis was performed on this crater.

Interplanetary Dust Particle Nomenclature: The first five characters of the IDP names refer to the Collector surfaces from which the particles were retrieved. The L2071 collector (from which one of the IDPs in this study was removed) was exposed for 50 hours between June 30 and July 30, 2008. L2083 collector (the collector from which three particles in this study were retrieved) was exposed for 32 hours between May 6 and May 23, 2010, and L2079 collector (from which one IDP in study was retrieved) was exposed for 16 hours between June 2 and June 23, 2010. All collectors were flown aboard NASA ER-2 or WB-57F aircraft.

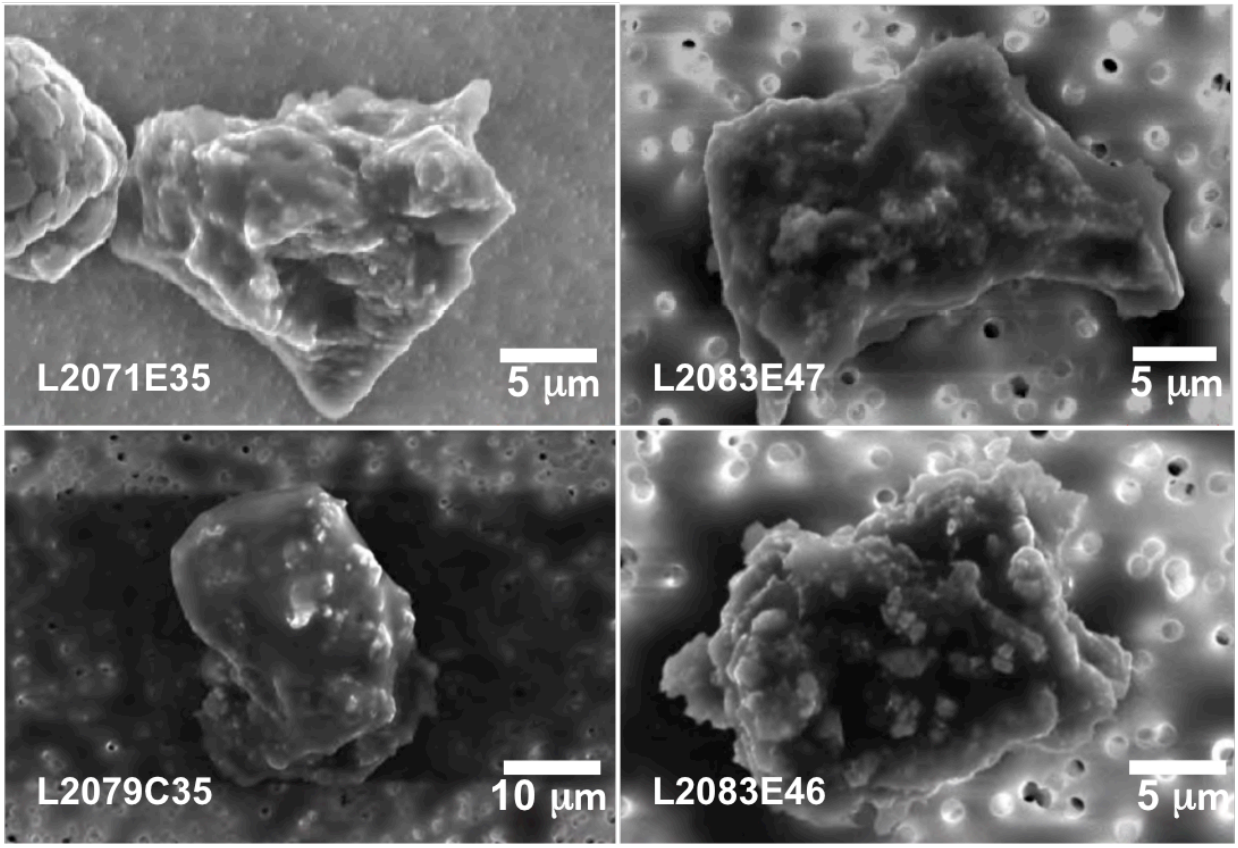

Fig. 4.16: Secondary electron images of four hydrated Interplanetary Dust Particles (image modified from the Cosmic Dust Catalog Volume 18).

	C	O	Mg	Al	Si	S	Ca	Cr	Mn	Fe	Ni
L2083E47	16.36	31.23	8.99	1.15	15.32	3.39	0.50	0.21	0.21	21.65	0.99
L2071E35	7.57	33.00	10.23	1.54	14.22	3.26	0.24	0.24	0.19	28.30	1.22
L2079C19	17.00	28.18	7.05	0.65	11.91	2.57	0.44	0.07	0.13	30.64	1.36
L2079C35	20.15	28.76	11.85	0.68	12.38	5.12	1.64	0.23	0.70	17.62	0.87
L2083E46	22.47	27.68	7.06	0.75	13.43	4.53	1.40	0.16	0.16	21.04	1.33
L2083D46	4.60	23.75	5.07	0.56	6.81	20.87	0.57	0.36	0.34	40.81	1.76
CI	3.48	45.9	9.58	0.85	10.7	5.35	0.922	0.265	0.193	18.5	1.08

Table 4.2: EPMA elemental data for IDPs analyzed in this study, compared with CI compositons.

L2071E47 is a 20µm, irregularly shaped particle exhibiting hydrated mineralogy. TEM examination revealed poorly crystalline phyllosilicates, fine grained Fe-Ni sulfides, and carbon nanoglobules. Magnetite framboids, which are indicative of precipitation from a fluid, are also observed in ~20% of the section. Electron probe microanalysis (EPMA) revealed a composition similar to CI chondrites for major elements, with the exception of carbon, which was slightly greater than twice as abundant as for CI chondrites.

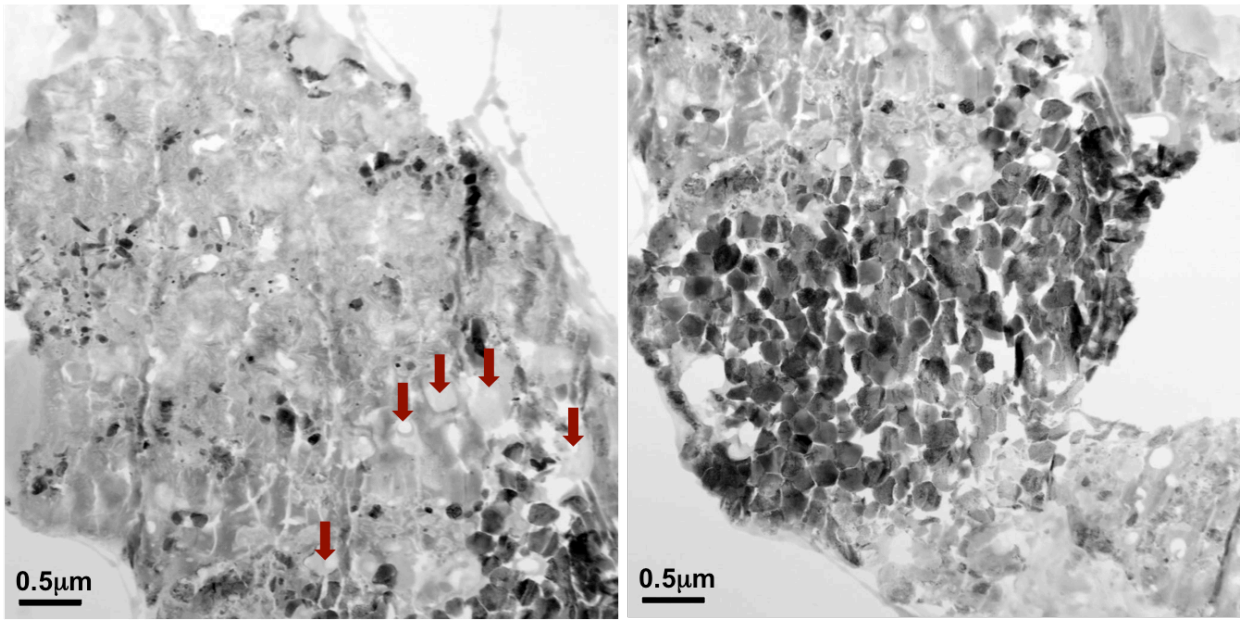

Fig. 4.17: TEM images of L2083E47. Red arrows point to several observed nanoglobules.

L2083E35 is a 20-25µm irregularly shaped particle. TEM analysis of microtomed slices of E35 revealed abundant carbonaceous material, poorly crystalline phyllosilicates and fine-grained Fe-Ni sulfides that are typical of IDPs exhibiting hydrated mineralogy. A magnetite rim on the perimeter of the grain is the result of strong heating during atmospheric entry; some phyllosilicates also exhibit signs of alteration due to heating. EPMA analysis revealed CI-like compositions to within a factor of two, with the exception of carbon, which was five times more abundant than for CI chondrites.

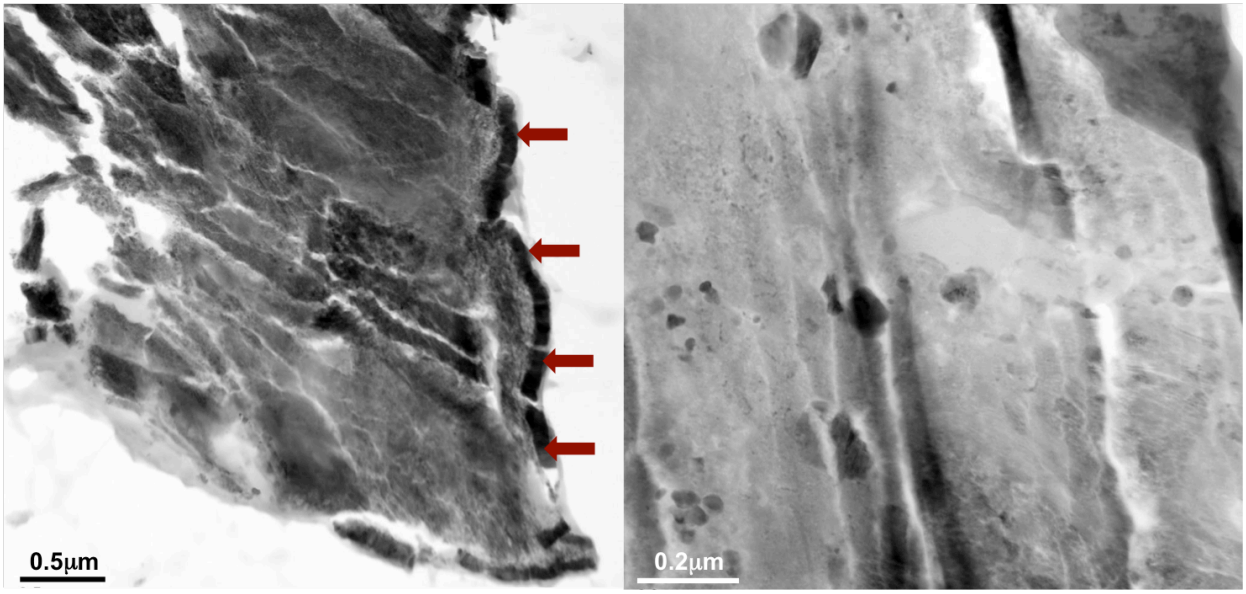

Fig. 4.18: TEM image of L2083E35. Magnetite rim indicates strong heating during atmospheric entry.

L2079C35 is a 30µm irregularly shaped opaque grain with a smooth texture. TEM brightfield and darkfield images reveal numerous carbon nanoglobules, rounded Fe-Ni sulfide grains, and intergrown coarse phyllosilicates with prominent 1nm basal spacing consistent with saponite. One enstatite grain examined showed preserved solar flare tracks, indicating minimal heating due to atmospheric entry. NanoSIMS imaging detected deuterium-rich hotspots in excess of 2000‰ that were associated with nanoglobules; similar D-rich nanoglobules have been reported in the Tagish Lake meteorite, and have been hypothesized to result from outer disk or pre-molecular cloud irradiation processes. EPMA analysis revealed major element compositions of C35 consistent with CI chondrites to within a factor of two, except for manganese, which was four times as abundant as CI chondrites, and carbon, which was almost six times as abundant as CI chondrites.

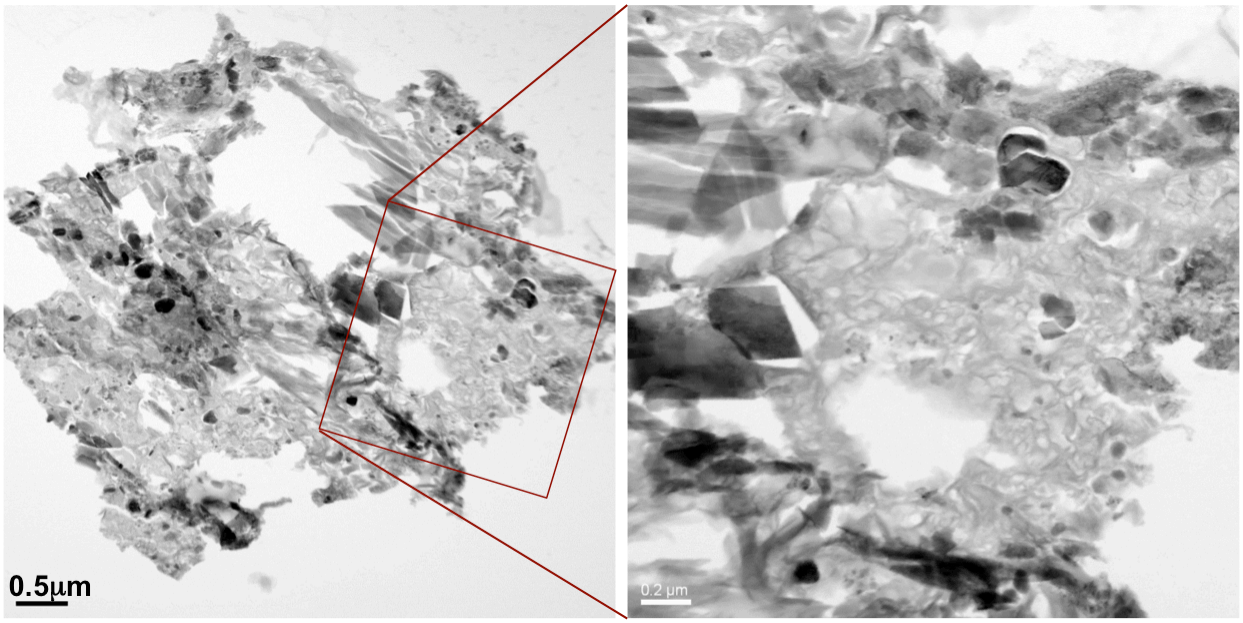

Fig. 4.19: Brightfield TEM image of L2079C35.

L2083D46 is an 18µm irregularly shaped particle with a smooth texture observed in the cosmic dust catalog SEM images. TEM images reveal a mineralogy dominated by a large iron sulfide grain and adhering silicate material with anhydrous mineralogy. EPMA data reveal compositions that are consistent with CI chondrites, except for Fe and S, which are more abundant due to the presence of the large FeS grain.

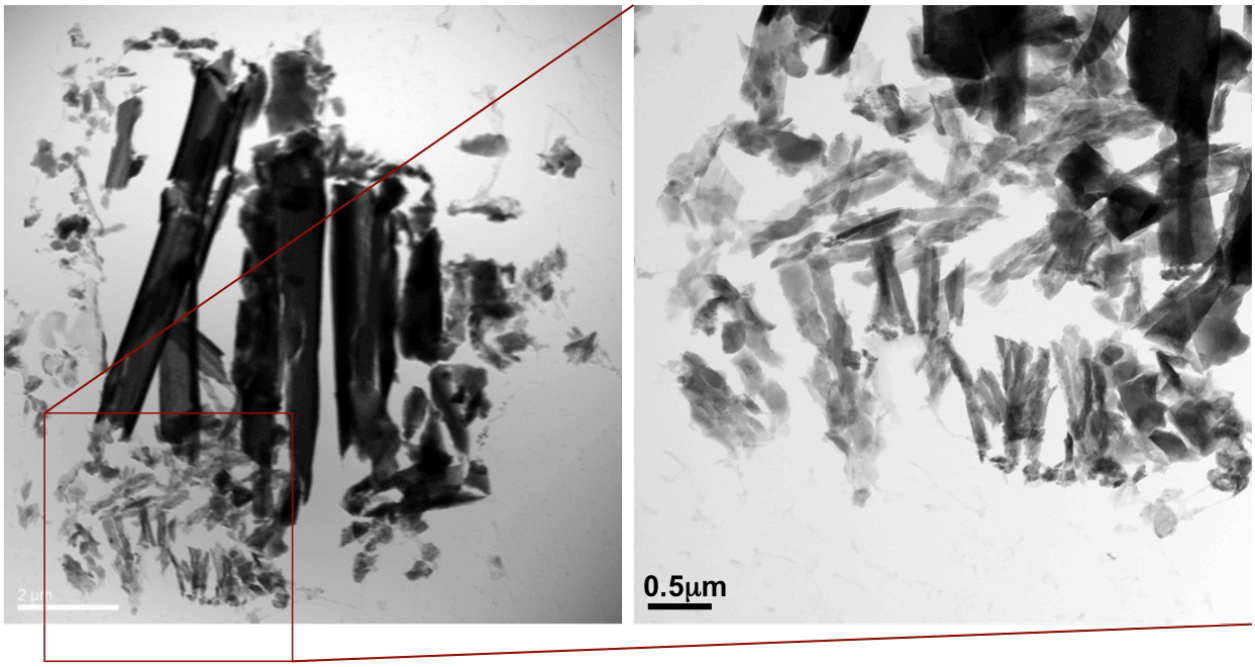

Fig. 4.20: Brightfield TEM image of L2083D46.

L2083E46 is 23µm grain with an irregular smooth texture; TEM brightfield and darkfield images show fine-grained phyllosilicates, carbon nanoglobules, round platy FeS grains, and occasional enstatite grains (Fig. 4.21). EPMA analysis reveal a carbon abundance of 6.5x that of CI chondrites, or over 20 weight percent; other major element abundances are consistent with CI compositions to within a factor of two.

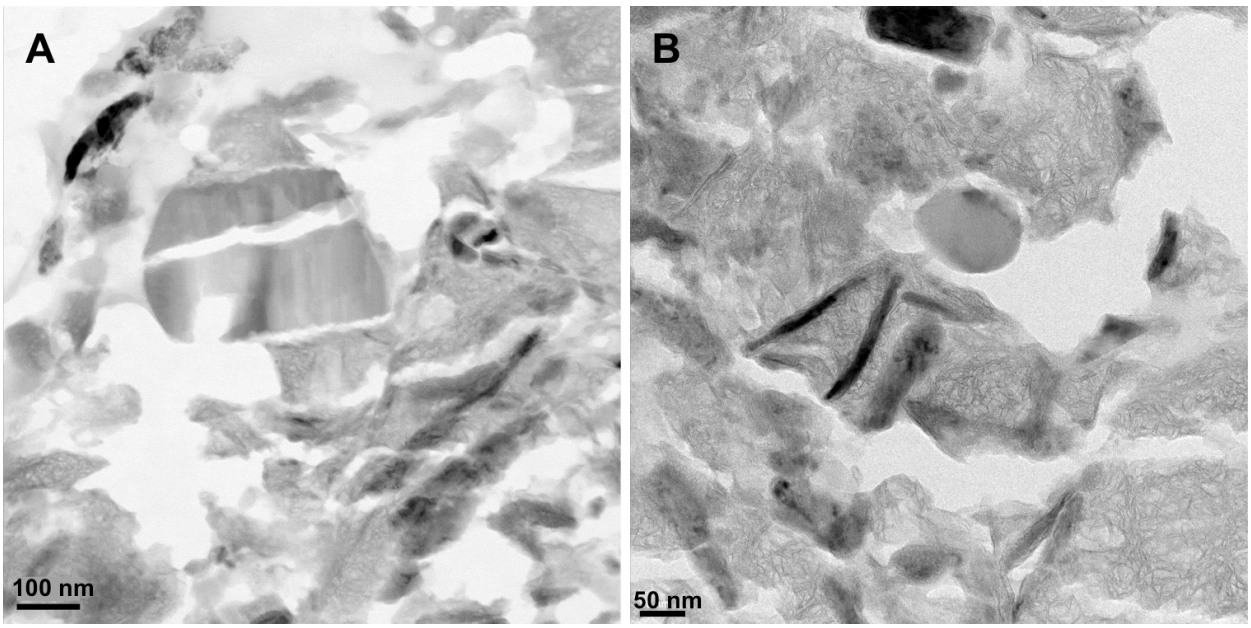

Fig. 4.21: A) Enstatite grain observed in brightfield TEM image of E46. B) Carbon nanoglobule observed amongst phyllosilicate textures in TEM image of E46.

Chapter 5: Results

Wild 2 Craters: The first two allocated craters, C2122W,4 and C2067N,3 were analyzed in August 2013, using the conditions described in the "analytical techniques" section, using a ~30μm defocused primary beam. The oxygen isotope compositions of these craters plotted in a region typical of planetary materials, and some carbonaceous chondrites. This was a surprising result, as the fine-grained components of cometary material were once thought to be a conglomeration of unprocessed interstellar grains containing occasional larger minerals of early solar system condensates (Whipple 1950). One initial concern of such a result was the possibility that a component of terrestrial oxide material from the aluminum contaminated the signal from the fine-grained dust. In subsequent analyses, we analyzed blank foils of flight Stardust foil pieces, mounted in a similar fashion to the Stardust craters. An evaluation of ^{16}O count rate as a function of time revealed a strong distinction between actual residues and oxide layers, which after ~100 cycles represented 0.1% of the residue signal. This is typically on order of the time in which sputtering equilibrium is reached. EDS maps further confirm that the O signal is strongly correlated with Mg, Si, and Fe. We therefore concluded that the oxygen measured in the craters was associated with the comet, and not terrestrial contamination.

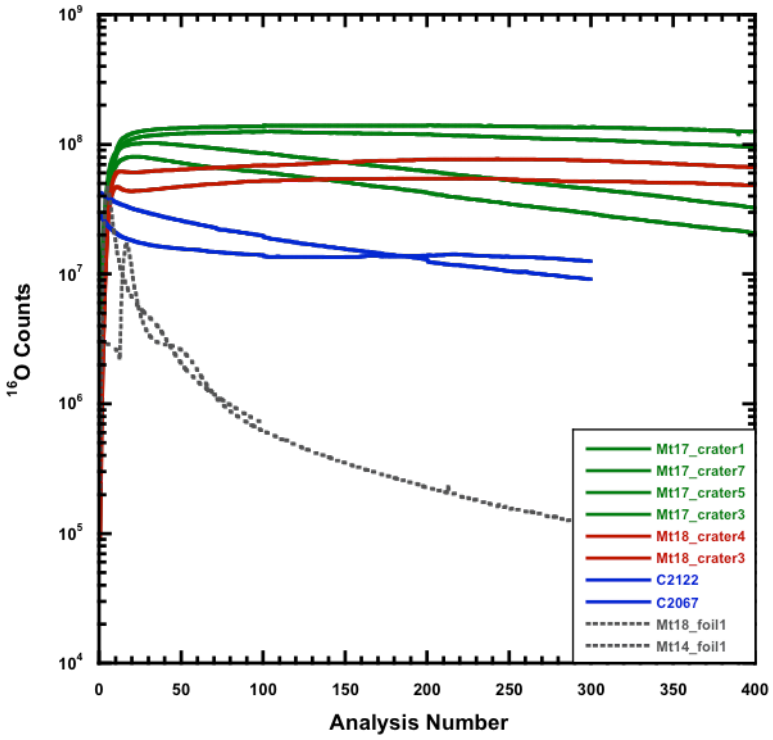

Fig. 5.1: ^{16}O counts plotted against analysis number (time) for crater residues, Wild 2 craters C2122W,4 and C2067N,3 and blank Al foils.

C2031W, 3 and C2104W, 4 were analyzed in November 2014 using a small 15µm raster with a 5µm spot size. C2031W,3 had a Δ^{17}O value of +3.8 permil and was roughly consistent with previous measurements. Examination of crater morphology, as well as SEM analysis and mapping suggest the impactor was a single mineral grain of Mg-rich olivine, with little or no fine-grained adhering material. C2104W,4 also appears to be a single grain impactor; its composition consisted of Fe, Ni, S, and O. The O is not strongly correlated with the rest of the residue, suggesting it might be terrestrial oxidation that occurred post-sample return. Oxygen isotope analysis of the residue revealed values similar to those of C2122W,4 and C2067N,3. However, the ^{16}O count rate decreased in a manner similar to those of oxide layers from our

contamination experiments, indicating that the oxygen signal is probably not associated with cometary oxygen. We include this data in our final analysis of the bulk value, with the caveat that the oxygen in this crater is very possibly post-encounter terrestrial oxidation of an iron-nickel sulfide.

Craters C2102N,1#1, C2102N,1#2, C2116W,0 and C2049N,1 were analyzed in April 2015 using the same analytical conditions as the November 2014 ion probe session. With the exception of C2049N,1, each crater was large enough for us to analyze multiple regions. The flattened craters retained their profiles such that regions of interest identified in the x-ray maps could be targeted for isotope analyses. In the case of C2049N,1, only the bowl-shaped bisected portion was flattened and analyzed via SIMS; the debris field upper portion was preserved for future analyses.

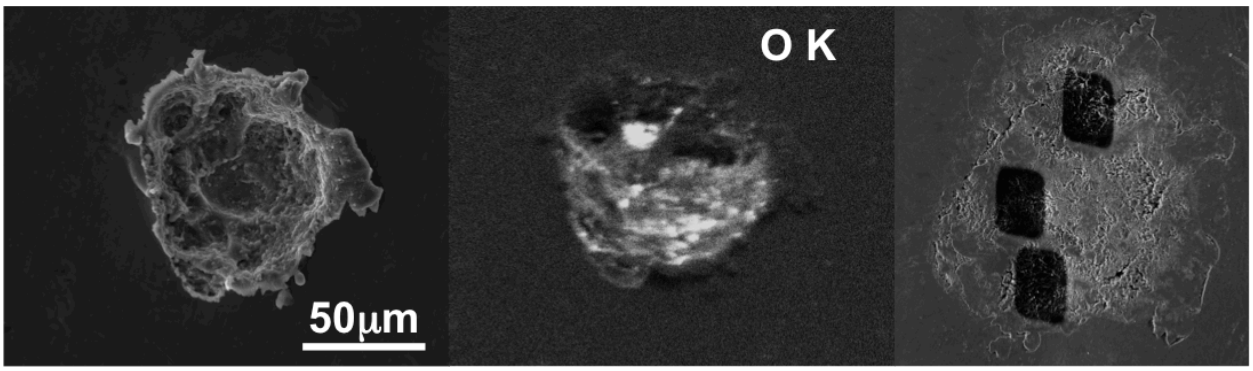

Fig. 5.2: SE image and X-ray map of C2102N,1#1 prior to flattening and SIMS analysis, compared with post-SIMS image of flattened crater showing multiple raster analyses.

C2024N,1, C2059W,1, C2076N,1 and C2022W,1 were analyzed in July 2015 with the same 0.5 nA , 5μm primary beam rastered over a ~15μm area that was utilized in previous sessions (with the exception of the August 2015 session). These four craters were smaller in diameter than craters from the previous allocation; only C2076N,1 was large enough to analyze multiple regions.

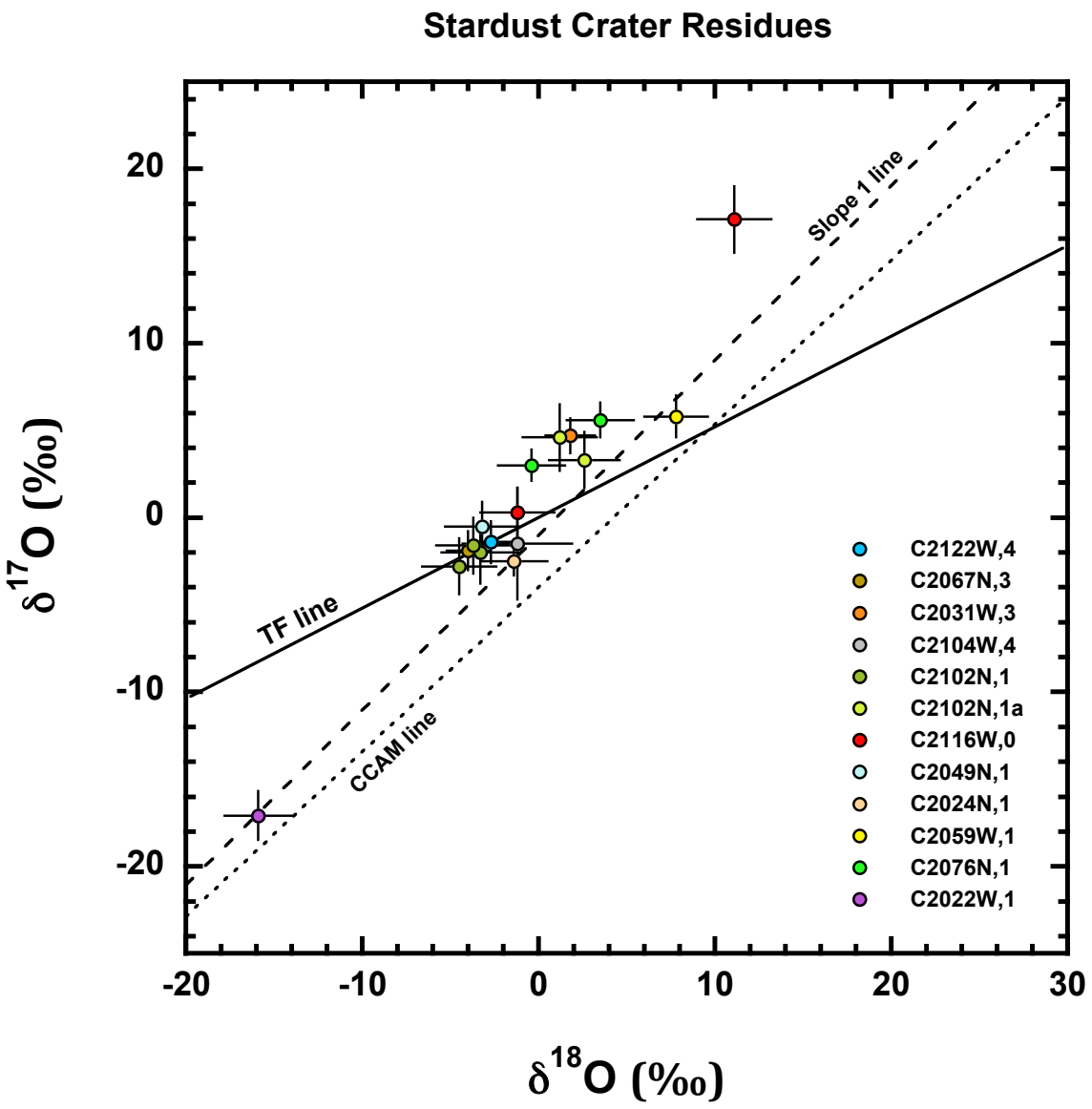

Fig: 5.3: Summary of Oxygen isotope compositions of Wild 2 Crater residues. Error bars are 2 s.e.

	$\delta^{18}O$ (‰)	$\delta^{17}O$ (‰)	$\Delta^{17}O$ (‰)
C2067N,3	-4.0 ± 1.2	-1.9 ± 1.1	-0.2 ± 1.3
C2122W,4	-2.7 ± 1.2	-1.4 ± 1.2	0.1 ± 1.3
C2031W,3	1.8 ± 1.4	4.7 ± 1.0	3.8 ± 1.3
C2104W,4	-1.2 ± 3.1	-1.5 ± 3.2	-0.9 ± 3.6
C2102N,1 #1 raster 1	-4.5 ± 2.1	-2.8 ± 1.6	-0.5 ± 1.9
C2102N,1 #1 raster 2	-3.3 ± 2.2	-2.0 ± 1.8	-0.2 ± 2.1
C2102N,1 #1 raster 3	-3.7 ± 2.1	-1.6 ± 1.6	0.3 ± 2.0
C2102N,1 #2 raster 1	2.6 ± 2.0	3.3 ± 1.6	1.9 ± 2.0
C2102N,1 #2 raster 2	1.2 ± 2.1	4.6 ± 1.9	4.0 ± 2.2
C2116W,1 raster 1	11.1 ± 2.1	17.1 ± 1.9	11.3 ± 2.2
C2116W,1 raster 2	-1.2 ± 2.1	-0.3 ± 1.4	0.9 ± 1.8
C2049N,1	-3.2 ± 2.1	-0.5 ± 1.4	1.1 ± 1.8
C2024N,1	-1.4 ± 1.9	-2.5 ± 0.8	-1.8 ± 1.3
C2059W,1	7.8 ± 1.8	5.8 ± 1.2	1.8 ± 1.5
C2076N,1 raster 1	0.4 ± 1.9	3.0 ± 0.9	3.2 ± 1.3
C2076N,1 raster 2	3.5 ± 1.9	5.6 ± 1.0	3.7 ± 1.5
C2022W,1	-15.9 ± 1.9	-17.1 ± 1.4	-8.8 ± 1.7

Table 5.1: Oxygen isotope values of twelve measured Stardust impact crater residues. Errors are 2 s.e. unless otherwise noted.

TEM Analysis of C2049N,1 Particles: Several individual particles (<5μm) were carefully removed from the debris field of C2049N,1, embedded in epoxy, and ultramicrotomed for analysis via transmission electron microscopy (TEM). All of the sections consisted of Si-O glass with Fe-Ni sulfide and metal inclusions interspersed throughout the section. Mg and Al were present and were heterogeneously distributed within the sections. Si-O glass has been recovered from tracks in aerogel (Tomeoka, Tomioka, and Ohnishi 2008); results of those measurements conclude such glass is most likely a secondary alteration product of impacting cometary particles and melted aerogel. As such, the discovery of such glass on Stardust foil is surprising. If the particles analyzed via TEM have similar origins to Si-O glass found in tracks, it would imply the impacting particle collided with a small piece of adhering aerogel debris before terminating at the foil surface. There are features in some TEM sections which look identical to the

compressed and unmelted aerogel attached to some terminal particles recovered from tracks. Such a chance encounter could explain why fine-grained material survived this collision more intact than other impacts into foils; however, no aerogel debris was observed on the foils prior to analysis, though it may have been dislodged as a result of the collision. Another possibility is that these melted particles represent a glass component that may have been present in the original impacting dust particle, analogous to a GEMS-rich IDP. Future SIMS/NanoSIMS analysis of this debris may better constrain the nature of the particle that produced this unique impact feature.

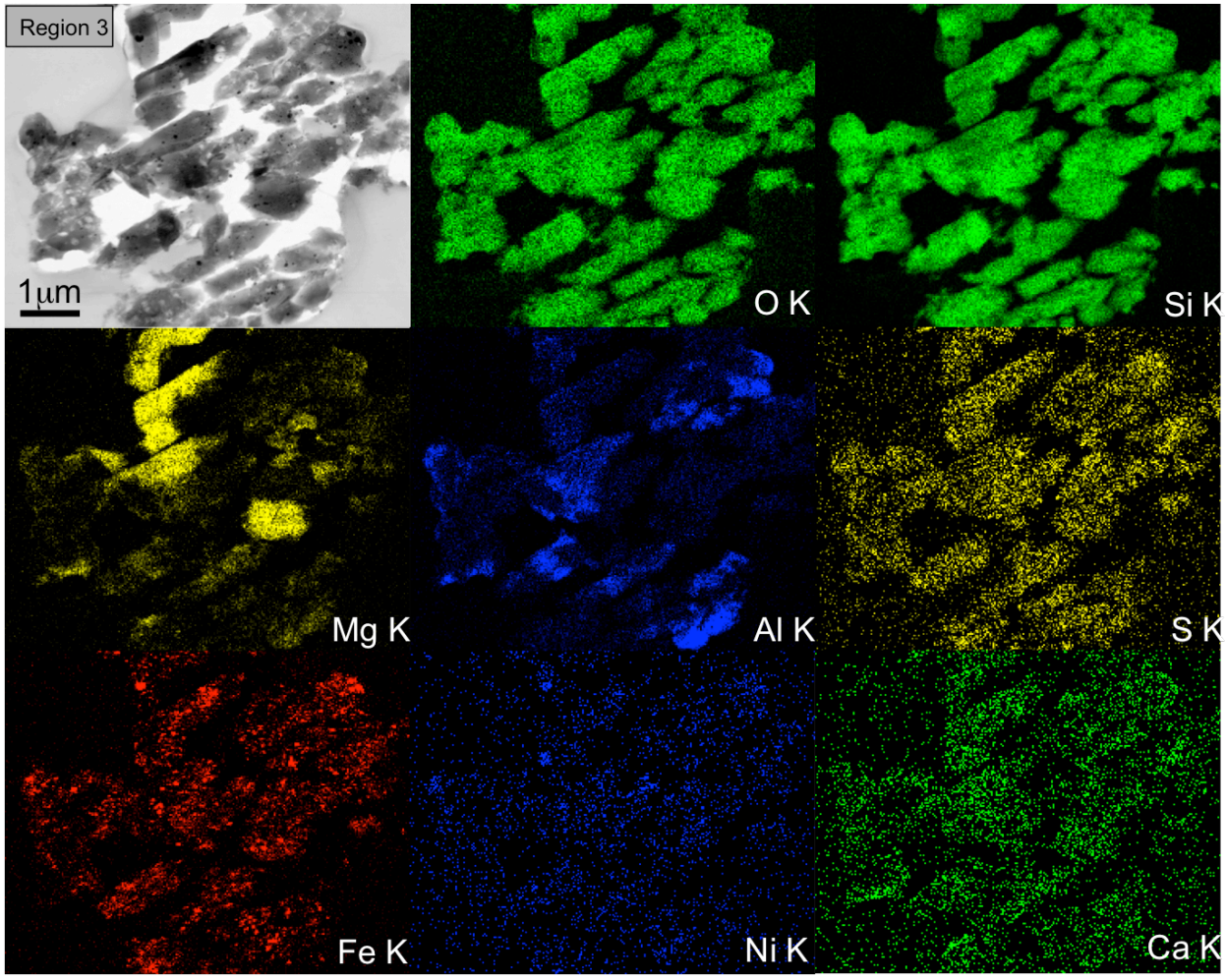

Fig. 5.4: TEM image and X-ray maps of C2049N,1 particle section.

Hydrated IDP results: Hydrated IDPs L208347 and L2071E35 were measured in

April 2012 using a 20KeV, 2.5nA Cs^+ primary beam and a 10µm spot size; IDPs L2079C35, L2083D46 and L2083E46 were measured in June 2015 using a 20KeV, 0.5nA Cs^+ primary beam and a 10µm spot size. A significant challenge in 3-oxygen isotope measurement of hydrated minerals via SIMS is the interference from $^{16}OH^-$ at mass $^{17}O^-$. Samples were mounted in Au foils that were pressed into 1" aluminum rounds (as described in the "sample preparation" section of this work), rather than in epoxy, in order to minimize outgassing of hydrogen bearing molecules in the sample chamber vacuum. In addition, a cold finger connected to an LN2 dewar was utilized to trap any excess hydrogen in the sample chamber. Finally, sufficient mass resolution to resolve the $^{17}O^-$ and $^{16}OH^-$ peak was achieved by appropriately adjusting the entrance and exit slits; for these analyses, a mass resolution of >9000 was used to completely separate the $^{17}O^-$ and $^{16}OH^-$ peaks. $^{16}O^-$ was measured on a Faraday cup (L'2 for the April 2012 analysis session, and C for the June 2015 session), $^{17}O^-$ was measured using the axial EM (both sessions), and $^{18}O^-$ was measured on electron multipliers. San Carlos Olivine, Burma Spinel, and Afrique magnetite were used to define the TF line.

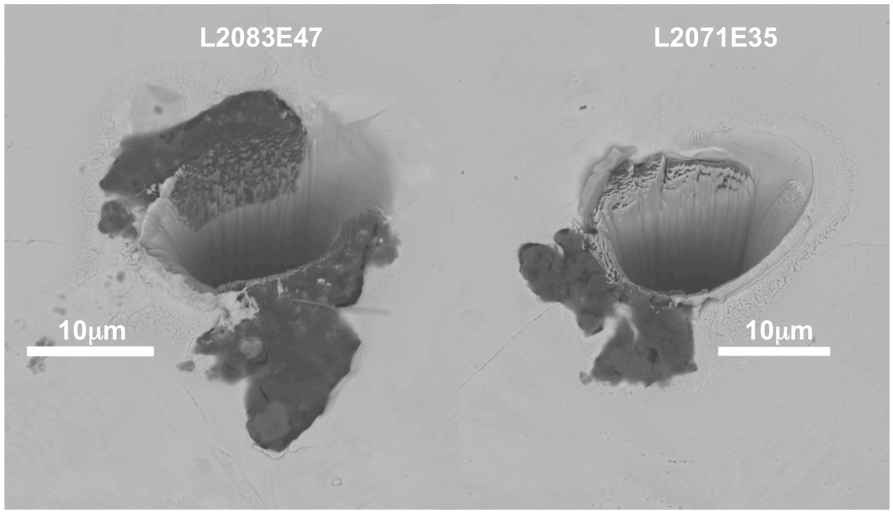

Figure 5.5: SEM images of IDPs E47 and E35 post-SIMS analysis.

Afrique magnetite (which was located on a separate standard mount) was chosen to correct for instrumental mass fractionation for IDPs E47 and E35 due to high the magnetite content of these particles. C35, E46 and D46 were corrected using San Carlos olivine grains that were pressed into the same foil as the IDPs. Oxygen isotope compositions for E35 and E47 were measured in four repeat analyses per particle. However, the combination of flattening of the IDPs onto a Au foil surface that hadn't been annealed, and use of a relatively high primary beam resulted in completely sputtering through each sample after the first 20 cycles.

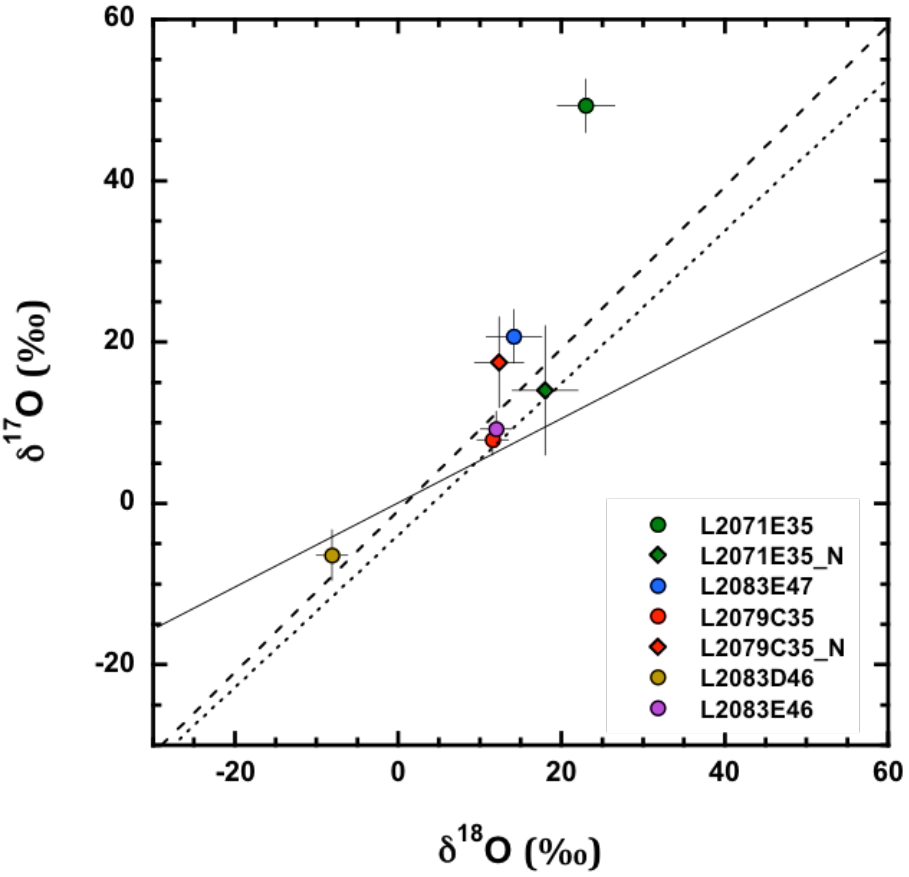

Fig. 5.6: Results of SIMS measurements of four hydrated IDPs and one anhydrous IDP. Error bars are 2 s.e.

	$\delta^{18}O$ (‰)	$\delta^{17}O$ (‰)	$\Delta^{17}O$ (‰)
L2083E47	14.2 ± 3.4	20.7 ± 3.3	13.4 ± 3.7
L2071E35	23.0 ± 3.5	49.3 ± 3.3	37.4 ± 3.8
L2079C35	11.6 ± 1.9	7.9 ± 1.9	1.8 ± 2.2
L2083D46	-8.1 ± 1.9	-6.4 ± 3.1	-2.1 ± 3.2
L2083E46	12.0 ± 1.9	9.2 ± 2.2	3.0 ± 2.4

Table 5.2: Oxygen isotope summary of five measured IDPs (four hydrated and one anhydrous). Errors are 2 s.e.

Results of SIMS measurements are shown in Figure 5.5 and Table 5.2. The large error bars for E35 and E47 are a consequence of using magnetite as a standard for particles that have heterogeneous magnetite and phyllosilicates compositions. NanoSIMS analyses of TEM sections of C35 and E35 are also plotted; the large error bars for these points are a result of low counting statistics inherent in the analysis of a 70nm thick slice of material.

Chapter 6: Discussion

The following discussion examines the implications of the results of the oxygen isotope measurements reported in this study for relationships between comet dust, anhydrous and hydrated interplanetary dust particles, and carbonaceous chondrites, as well as implications for models of comet formation and oxygen isotope heterogeneity in the solar system.

Comparisons with Stardust Terminal Particles: The measured O-isotope compositions of Wild 2 crater residues are broadly consistent with the results of single mineral grains extracted from aerogel (Fig. 6.1), though subtle differences are observed. Most of the crater residues plot slightly to the left of the slope 1 line that has been suggested to represent the mixing line of the original oxygen isotope reservoirs (Young and Russell 1998). In contrast, the compositions of Wild 2 particles extracted from aerogel appear shifted more towards the Carbonaceous Chondrite Anhydrous Minerals (CCAM) line. This difference may be the result of a measurement bias (either for the craters or aerogel-extracted particles), or it may represent a real difference in sample compositions. The mineralogy of aerogel-extracted particles has been interpreted as comet 81P/Wild 2 incorporating processed inner solar system material that was transported to the outer disk regions where comets are thought to have accreted, and oxygen isotope measurements of these particles have been thus far consistent with this interpretation. While the crater residue measurements do not specifically sample the fine-grained, matrix-like material, the isotope composition of such material should be at least partially preserved and mixed with the larger coarse-grained (> 1μm) refractory dust; the aerogel capture process, in contrast, preferentially

destroys and contaminates the submicron dust component. If synchrotron measurements of aerogel tracks are correct (Flynn et al. 2006), the majority of the mass (and therefore the oxygen isotope composition) of the crater residues, at least in the case of impact craters with complex morphologies, should reflect the fine-grained component of comet dust, and observed offset between the Wild-2 residues and the terminal particles may be due to isotopically distinct components.

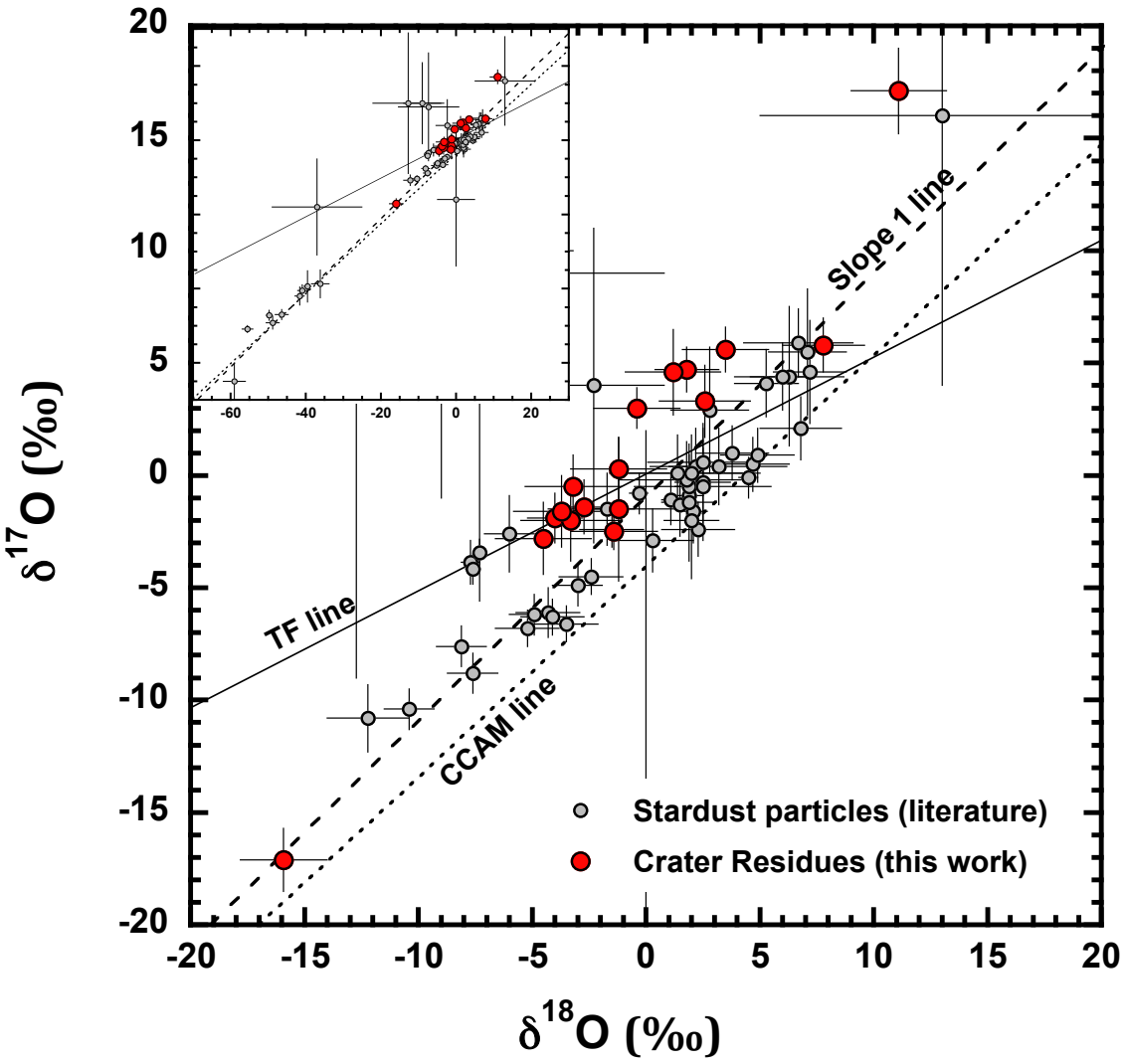

Fig: 6.1: O isotopes in Wild 2 crater residues compared to O isotopes in wild 2 particles extracted from aerogel. Lines plotted are the Terrestrial Fractionation (TF) line, Carbonaceous Chondrite Anhydrous Minerals (CCAM) line, and a slope 1 line (Young and Russell 1998). Large error bars are NanoSIMS measurements.

Anhydrous Interplanetary Dust Particles: The oxygen isotope compositions of Stardust impact crater residues are indistinguishable from those reported for chondritic porous interplanetary dust particles (Aleon et al. 2009; McKeegan 1987; Nakashima, Ushikubo, Zolensky, et al. 2012;

Starkey and Franchi 2013). In fact, the compositions of crater residues more closely match CP-IDPs than they do Stardust particles extracted from aerogel tracks, which suggests that the compositional difference between the Wild 2 crater residues and the particles recovered from aerogel tracks represents a sampling rather than a measurement bias. IDPs have compositional, spectral, and dynamic relations to cometary sources; the results of this study also indicate a strong isotopic link.

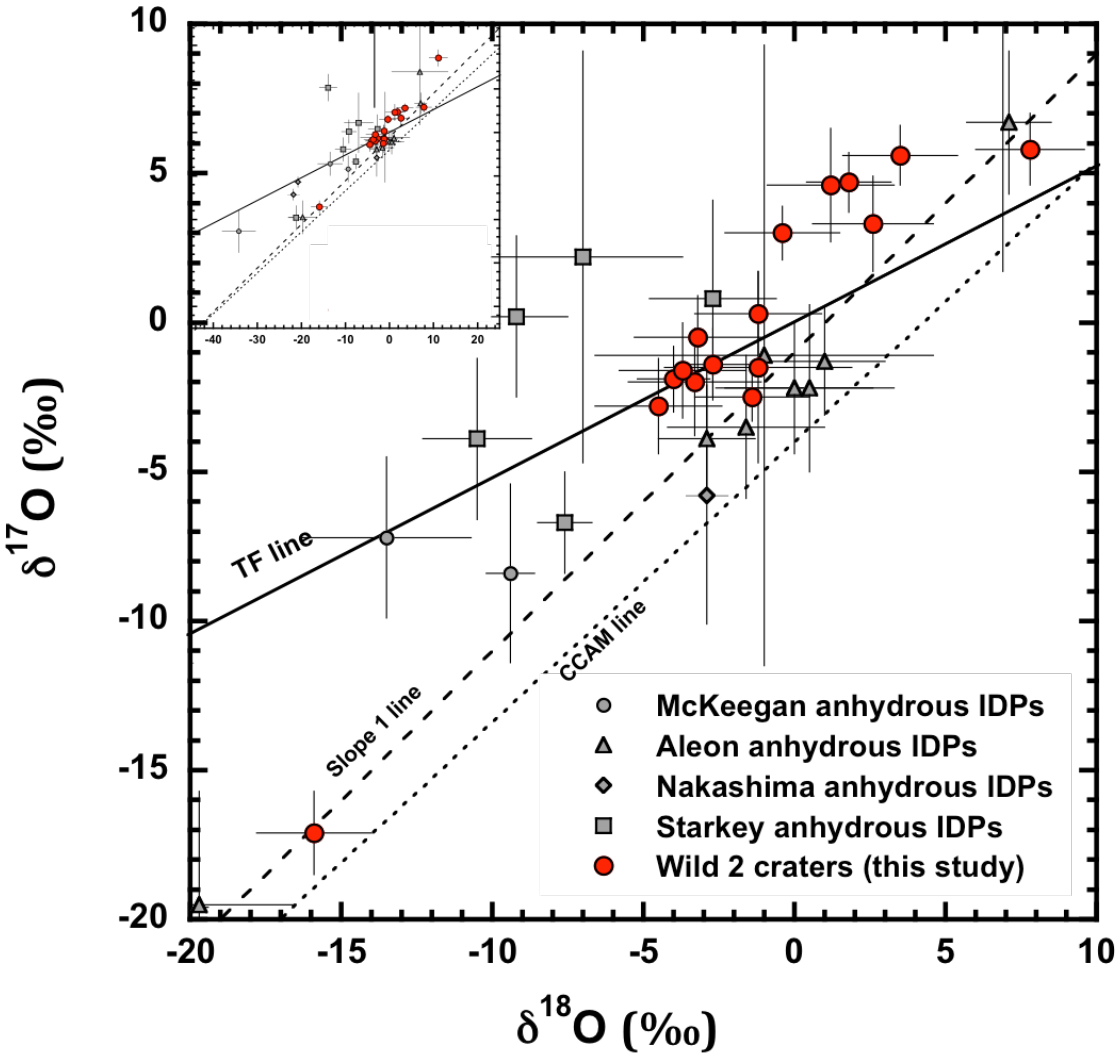

Fig: 6.2: O isotopes in Wild 2 crater residues compared to O isotopes in anhydrous IDPs.

Carbonaceous Chondrites: Oxygen isotope compositions of Wild 2 crater residues do not overlap (Fig. 6.4) with whole rock carbonaceous chondrite compositions in three isotope space (Schrader et al. 2011); in fact, they do not clearly overlap with bulk compositions of any meteorite group. Carbonaceous chondrite bulk compositions are affected by parent body

alteration (Clayton and Mayeda 1999); Wild 2 dust has not experienced such processing, which may account for the offset compositions relative to bulk carbonaceous chondrites. Reported isotope compositions for anhydrous mineral grains recovered from Orgueil and Ivuna CI chondrites (Leshin, Rubin, and McKeegan 1997) correlate strongly with Wild 2 aerogel-extracted particles (Fig. 6.3), and therefore have a similar association to Wild 2 crater residues, suggesting a genetic link between IDPs and carbonaceous chondrite components; yet none of our data lie within the range of bulk measurements of meteorite groups or planetary materials. Bulk compositions of Wild 2 dust may reflect primordial dust compositions prior to being subjected to parent body alteration. Perhaps some Jupiter family comets that do not suffer catastrophic disruption experience aqueous alteration and evolve into the parent bodies of CI and CM chondrites.

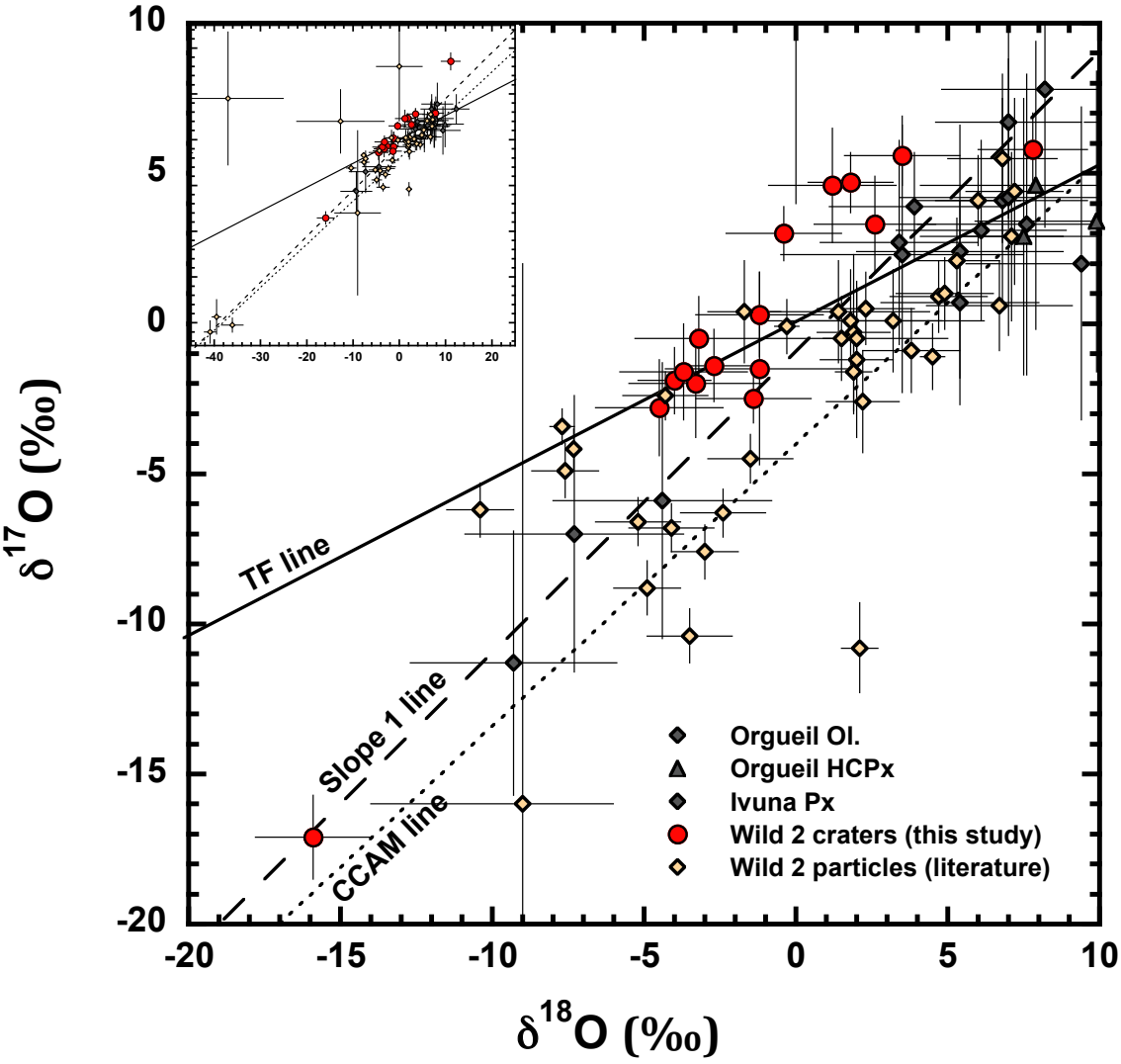

Fig: 6.3: Wild 2 crater O compositions compared to O compositions of anhydrous minerals in CI chondrites (Leshin, Rubin, and McKeegan 1997).

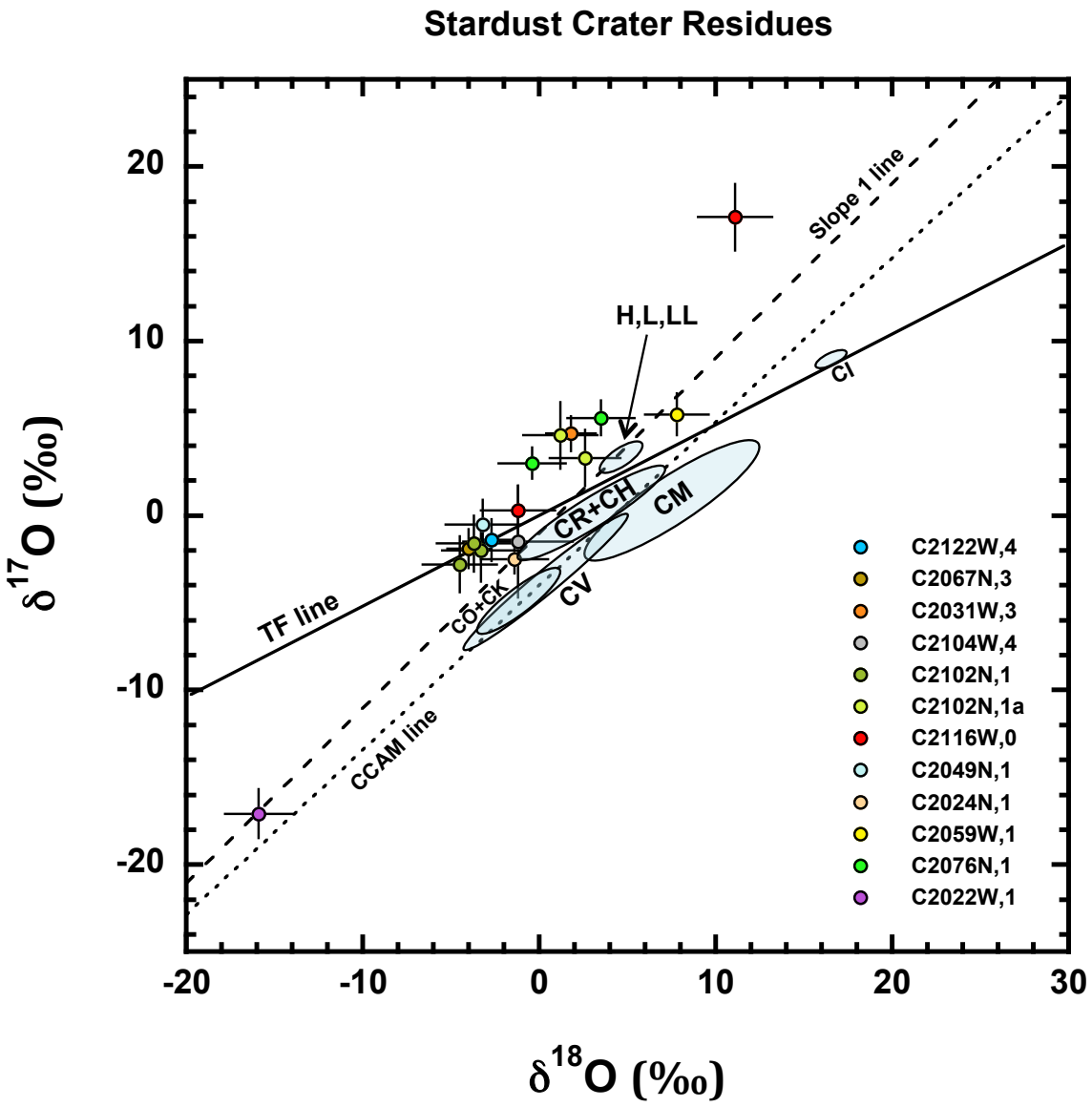

Fig: 6.4: O isotopes in Wild 2 crater residues compared to whole rock O isotope compositions of carbonaceous and ordinary chondrites.

Hydrated IDP results: E35 has a $\Delta^{17}O$ of +37‰, larger than those previously reported for IDPs, but comparable to the "Nugget" Fe-rich IDP reported in the thesis of McKeegan 1987 (McKeegan 1987). McKeegan observed that the large $^{17,18}O$ excesses in nugget were similar to those reported in deep-sea spherules by Clayton et al. (Clayton, Mayeda, and Brownlee

1986). Clayton attributed the enriched heavy oxygen of the spherules to oxidation upon atmospheric re-entry. L2071E35 does show evidence of strong atmospheric heating. Measured oxygen isotope compositions of air reported by Thiemens (Thiemens et al. 1995) are not as ^{17,18}O-enriched as this IDP, and even extremely heavy values for tropospheric ozone (Johnston and Thiemens 1997) do not account for E35's composition to the left of the slope 1 line. The oxygen isotope composition may possibly reflect a significant contribution of ^{17}O-rich material to this IDP; however, NanoSIMS analysis of a TEM slice of this particle did not reveal any ^{17}O hot spots.

The other IDPs exhibiting hydrated mineralogy all show modest to significant ^{17,18}O-enrichments. The most extreme enrichment in a non-atmospherically heated particle appears in L2083E47, which contained significant amounts of framboidal magnetite. Modest enrichments of ^{17}O and ^{18}O are also observed in IDPs C35 and E46. These results may reflect equilibrium isotope exchange with ^{17,18}O-enriched H_2O, in the case of the IDPs with phyllosilicates mineralogy, and complete assimilation of the ^{17,18}O-enrichment via oxidation, in the case of the magnetite framboids. Isotopically heavy H_2O has been associated with Fe phases in several studies. The extreme enrichments in Acfer 094 are associated with new-PCP (poorly characterized phases), which were mixtures of magnetite and pentlandite (Sakamoto et al. 2007). ^{17,18}O-enrichments have also been observed in Semarkona magnetite (Choi et al. 1998). The "Nugget" IDP has a Δ^{17}O of 30‰ IDP plots on a line of slope 1 (McKeegan 1987). The measured crater C2116W,0 was the only crater to exhibit a heterogeneous oxygen isotope composition, with X-ray maps showing an area with olivine/pyroxene composition adjacent to an area with Fe/Ni composition. One of the rastered analyses of this crater had a Δ^{17}O of +11‰. This data, taken together,

suggests that the heavy H_2O predicted to exist by self-shielding models is best preserved in Fe oxidation products.

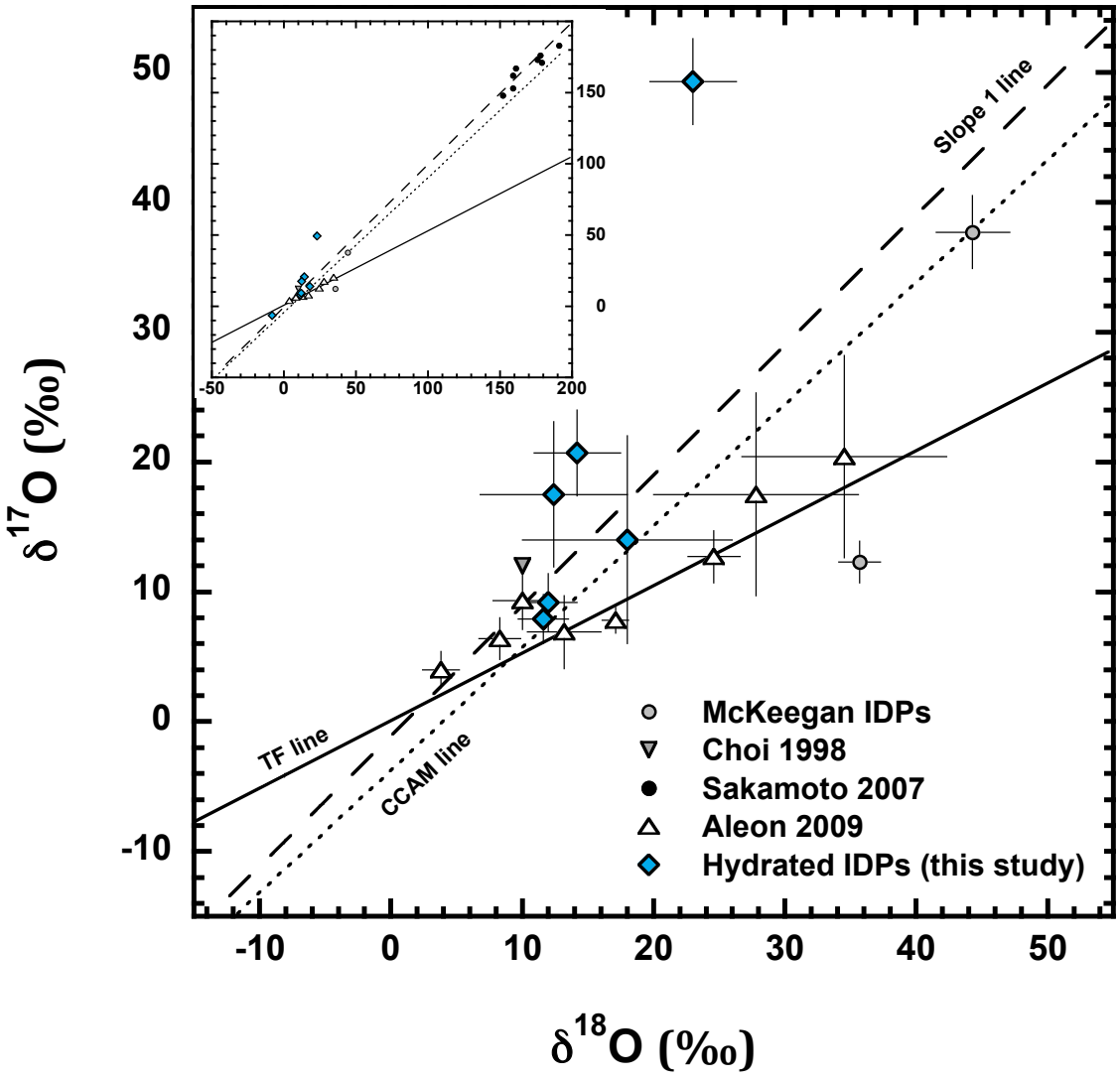

Fig: 6.5: Hydrated phases measured in meteorites and interplanetary dust particles.

The anhydrous IDP L2083D46 plots along the slope 1 line and is consistent with other measurements of other IDPs with anhydrous mineralogy (Aleon et al. 2009; McKeegan 1987; Nakashima, Ushikubo, Zolensky, et al. 2012; Starkey and Franchi 2013). This particle was

removed from the same L2083 collector as E47 and E46. Though it is not possible to definitively attribute these particles to a common parent body, the discovery of particles with hydrous and anhydrous mineralogy within such proximity hints at localized and heterogeneous parent body alteration.

Implications for Models of Comet Formation: Comets had been previously interpreted as being the most pristine remnants of our solar system, containing ices that are stable only at temperatures lower than ~30 K, and a large component of interstellar and presolar nebular dust (Greenberg and Hage 1990; Donn and Sears 1963). These interpretations were initially supported by observations of circumstellar dust and enstatite whiskers in CP-IDPs (Bradley, Brownlee, and Veblen 1983; Messenger et al. 2003) assuming that these objects were derived from comets. Early isotopic and chemical results from analyses of Wild 2 dust have thus far not supported that interpretation. Instead, aerogel-extracted particles were largely high temperature crystalline refractory minerals that are thought to have formed close to the sun, interacted with a ^{17}O,^{18}O-enriched gas, and then were transported to 30-50AU, where they were incorporated into comets. Don Brownlee has suggested that whereas asteroids accreted rapidly relative to mixing timescales, and therefore record local oxygen isotope heterogeneities, comets accreted slowly relative to mixing timescales in the early solar system, and therefore have oxygen isotope compositions that sample more global oxygen environments (Brownlee 2014). Two consequences of this model of comet formation are that the oxygen isotopes measured in Wild-2 dust and anhydrous interplanetary dust particles should reflect the variability in dust O-isotope compositions over the entire global accretion environment, and all of the dust should average to planetary compositions. While the results of this study confirm an average planetary oxygen

isotope composition, the variability of between measurements of individual craters is quite small, with most O-compositions showing <10‰ variability. SIMS measurements of anhydrous IDPs show a similarly constrained dispersion of O-isotope values. Carbonaceous chondrites, in contrast, show a wide range of oxygen isotope compositions amongst groups (though, admittedly, the scales between IDPs and Wild-2 dust and CCs are very different). This suggests that comet dust is either sampling a localized region of accretion, with pollution of ^{16}O-rich inner solar system refractory solids restricted to a few percent, or that most dust in the solar system, prior to parent body alteration, varied by less than 10-20‰ and was centered around planetary compositions.

Implications for models of Oxygen Isotope Heterogeneity:

Self-shielding models explain the oxygen isotope heterogeneity in the meteorite record as due to an exchange between a ^{16}O-rich primordial dust and a photochemically-produced ^{17}O/^{18}O-enriched reservoir (Yurimoto and Kuramoto 2004; Lyons and Young 2005). These models have assumed average composition of primordial dust to be ^{16}O-rich relative to planetary material. While ^{16}O-rich calcium-aluminum inclusions in meteorites are amongst the earliest formed solids recognized in meteorite samples, they are the result of condensation from a hot gas of solar composition (Grossman 1973), and thus are unlikely to represent the average primordial (initial) dust.

The initial budget of solids that ultimately formed the planets consisted of largely homogenized circumstellar dust; the site of this homogenization process may have occurred in the diffuse

interstellar medium, in molecular clouds, or in the solar nebula. Mayo Greenberg predicted that comet dust was primarily composed of preserved sub-micron interstellar grains with silicate cores, organic refractory inner mantles and icy coatings that protected the cores from destructive processes such as sputtering, grain-grain collisions and shocks in the diffuse interstellar medium (Greenberg 1985; Greenberg and Hage 1990); this dust would form weakly adhering, porous aggregates in a "bird nest" structure. Indeed, a major motivation of the Stardust (and hence the mission name) was to collect this refuge of preserved interstellar dust. However, it is clear from the results of analyses of Wild 2 samples that, despite preferential destruction of the submicron component during aerogel capture (Floss et al. 2013), presolar grains with large isotope anomalies make up less than 0.1% of the mass encountered by the Stardust collector. What is less apparent is the degree to which Wild 2 dust preserves presolar material. Models have predicted that interstellar grains should be destroyed in 2-4x10^8 years by supernova shocks, which is much faster than the rate at which new stars inject dust into the ISM (Jones et al. 1994); therefore, if the models are correct, dust survives ISM processes due to protective icy/organic mantles, or it is efficiently reformed by poorly understood processes. The destruction and redeposition of dust in the ISM would likely erase definitive presolar/circumstellar isotopic signatures, and perhaps provide a homogenized baseline oxygen isotope composition for the solids that accreted in the early solar nebula. Glasses Embedded with Metals and Sulfides (GEMS) that are commonly observed in anhydrous interplanetary dust particles exhibit features that have been linked to interstellar origins (Bradley and Dai 2004; Bradley 2013); however, Keller and Messenger maintain that GEMS are the result of late stage, non-equilibrium condensation from a gas that had previously condensed Mg-rich silicates (Keller and Messenger 2011, 2013), and that GEMS were preserved in IDPs but destroyed by parent body processes in

meteorites (Keller and Messenger 2012). Although GEMS are not conclusively observed in Wild 2 dust, they may have been present and destroyed in the aerogel capture process (or similar features may have been produced by hypervelocity aerogel capture). Despite the controversy regarding the origins of GEMS grains, isotopically anomalous presolar grains are better preserved in anhydrous IDPs than they are in meteorites, accounting for as much as 1.5% of total particle mass (Busemann et al. 2009). If homogenization processes occur in the ISM that erase the isotopic signatures of circumstellar condensates, this homogenized dust should be well-preserved in IDPs and cometary material.

Definitively recognizing such dust in Wild 2 samples and IDPs is complicated by evidence of large-scale radial mixing and the pollution of the outer solar system comet forming regions by material processed in the inner disk. Had the O-isotope compositions of the Stardust crater residues exhibited large negative average $\Delta^{17}O$, the result would likely have been interpreted as evidence for the ^{16}O-rich primordial dust predicted by self-shielding models (Clayton 2002b; Lyons and Young 2005; Yurimoto and Kuramoto 2004). However, that was not what is found; and so the nature and origin of the fine-grained component remains unknown. One possible scenario is that early inner disk processing erased initial ^{16}O-rich compositions of presolar, molecular cloud dust by destruction and recondensation, or via high temperature gas-solid equilibrium isotope exchange with a $^{17}O/^{18}O$ enriched gas. This processed material was then transported to comet forming regions along with high temperature refractory minerals, where it slowly accreted with local ice and 0.1-1% isotopically anomalous presolar (i.e. circumstellar) grains. I view this as unlikely based on mineralogical evidence of CP-IDPs which, as discussed above, are linked to comets. It is more likely that amorphous fine-grained comet dust is

composed of primordial, ISM or molecular cloud condensed material that accreted locally, along with ices, molecular cloud organic material and surviving circumstellar presolar grains into comet parent bodies. This would imply that the average O-isotopic composition of primordial dust is similar to that of planetary solids, and thus if CO self-shielding is the source of the oxygen isotope heterogeneity in the solar system, it minimally affected the compositions of most silicate dust. Because the silicon in the Sun originally derives from accreted dust, we can infer by mass-balance that the dust contributed ~25% of the Sun's oxygen inventory, whereas ~75% was accreted as gas (Krot et al. 2010). Therefore a consequence of a planetary composition of primordial dust is that the initial accreted gas was more ^{16}O-rich on average than the current oxygen isotope composition of the Sun. At least one chondrule isotopically lighter than the current composition of Sun has been measured (Kobayashi, Imai, and Yurimoto 2003) and may represent interaction with/condensation from this early extreme ^{16}O-rich gas. Anhydrous components of comet dust did not interact with ^{17,18}O-enriched water, nor were they affected by high temperature exchange with the ^{16}O-rich gas. The possibility that most solids in the outer solar system retain their primordial oxygen isotope compositions, and that this composition is similar to the terrestrial value, may be the most significant finding of Wild 2 dust oxygen isotope measurements.

Future directions: Stratospheric collection of interplanetary dust particles will continue to be an important source of comet dust. In particular, timing IDP collections with the Earth's interception of known dust streams (Messenger 2002), such as the 26P/Grigg-Skjellerup dust stream (Busemann et al. 2009) will provide opportunities to examine compositional and isotopic diversity amongst JFCs. However, future comet sample return missions will present the best

opportunity to resolve outstanding issues. Stardust collections were biased in favor of robust, coarse-grained refractory components, and interplanetary dust particles are possibly biased in favor of particles with longer residence times in the stratosphere. In some respects, these sample biases are complementary; however, both collection mechanisms only sample solid dust. Future missions could be designed to avoid sample biases by collecting several grams to a kilogram of comet ices and volatiles, in addition to solids, cryogenically stowing them, and returning them to Earth. Collection of comet dust samples should occur at low or zero encounter velocities in order to resolve questions unanswered by investigations of Stardust samples (e.g. ratio of fine-grained to coarse-grained dust, amorphous to crystalline ratio, presence of GEMS grains). Most critically, a $^{17}O/^{18}O$-rich composition for comet H_2O ice would be compelling validation of self-shielding models, even if primordial dust can never be unambiguously identified, especially if it is found to be in disequilibrium with ices derived from CO.

Chapter 7: Concluding Remarks

I. The oxygen isotope composition of Wild 2 dust is indistinguishable from the compositions of chondritic porous interplanetary dust particles (CP-IDPs). Oxygen isotope compositions have long been used as a tool for classification of meteorite groups. Based on the results of these O-isotope measurements of Wild 2 dust, along with other evidence linking CP-IDPs to comets, including high contributions of Jupiter Family comets to the zodiacal cloud dust, the high concentrations of molecular cloud organic material, higher concentrations of isotopically anomalous presolar grains than are found in meteorites, porosities that are consistent with estimates for JFC porosities, resemblance of large cluster IDPs to COSIMA images of dust from Comet 67P/Churyumov-Gerisemenko, and petrographic features not observed in meteorites, it can be concluded that comets are the parent bodies of CP-IDPs.

II. Comet dust is not, on average, ^{16}O-rich relative to planetary materials; the oxygen isotope heterogeneity in the comet dust is 10-20‰, centered around planetary compositions.

III. The ^{16}O-rich dust that is observed in Wild 2 samples is associated with large (>1μm) crystalline grains of refractory mineralogy, and is present in concentrations of several percent. This dust is not native to comet forming/accretion regions, but has been transported from the inner solar system via outward radial migration.

IV. Anhydrous dust in comets did not interact with H_2O; therefore the oxygen isotope compositions of Wild 2 dust and of CP-IDPs are the primordial dust compositions. This implies that present planetary oxygen isotope compositions of dust are largely inherited from primordial dust (i.e. dust that has not experienced processing on a parent body), and that ^{16}O-rich inclusions represent exchange with ^{16}O-rich solar composition gas rather than a primordial dust composition. CO self-shielding did not significantly affect dust compositions, and probably occurred in molecular clouds rather than at the inner solar nebula disk surface.

V. Evidence for interaction with heavy H_2O is most prominent in Fe phases (Wild 2 craters, hydrated IDPs, Semarkona magnetite, Acfer 094 simplectite).

VI. IDPs with phyllosilicate mineralogy show evidence of slight interaction with the heavy H_2O reservoir, but effects are subtle. The source of hydrated IDPs is still unknown, but may sample similar parent bodies as CM/CI chondrites. High carbon hydrated IDPs may be aqueously altered CP-IDP dust; there may be a link between CI/CM chondrite parent bodies and comets.

VII. Oxygen isotope compositions of hypervelocity impactors are retained in the resulting crater residues, and can be successfully measured by SIMS if matrix and mass-dependent fractionation effects are calibrated against laboratory-produced standard mineral crater residues.

Appendix A: EDS Spectra and X-Ray maps for Stardust Craters

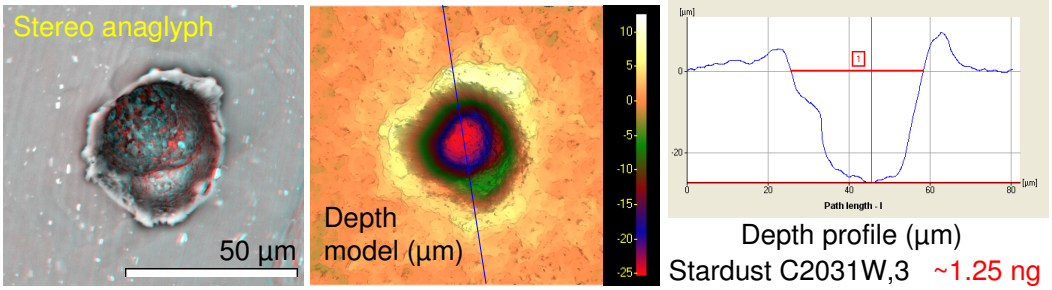

Depth profile (µm)
Stardust C2031W,3 ~1.25 ng

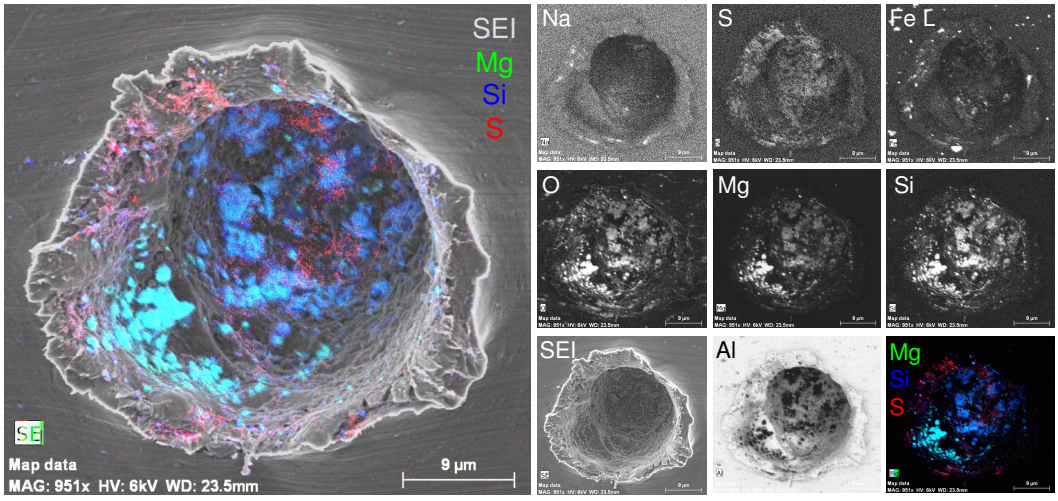

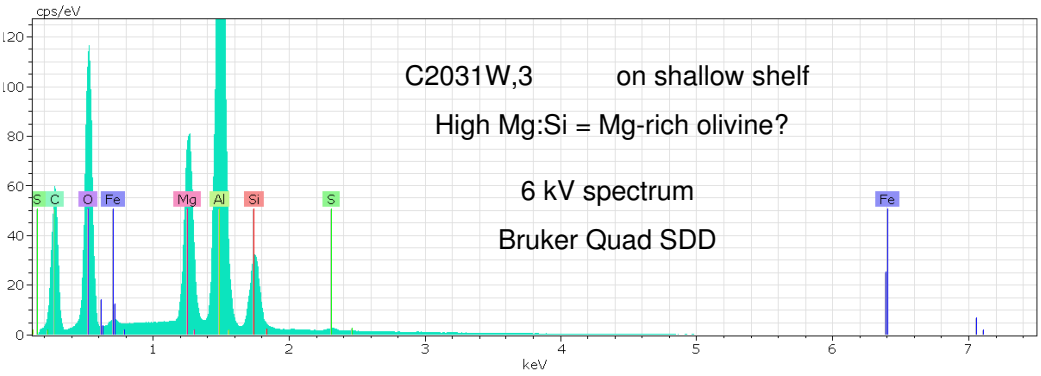

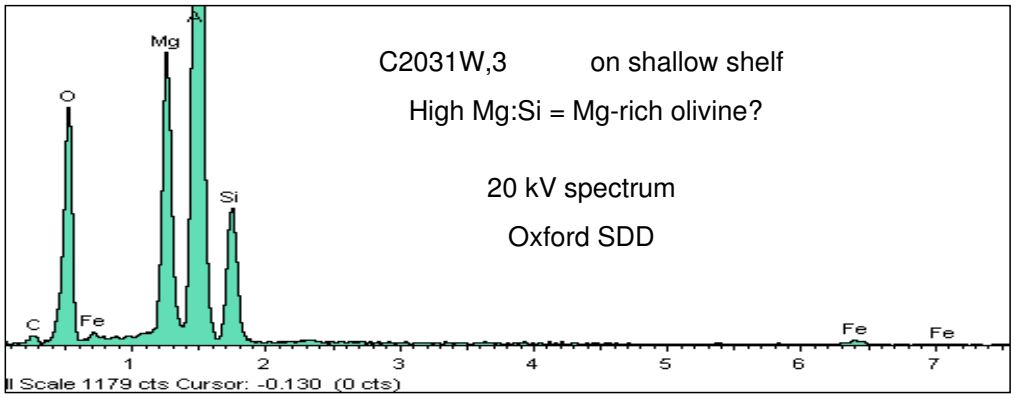

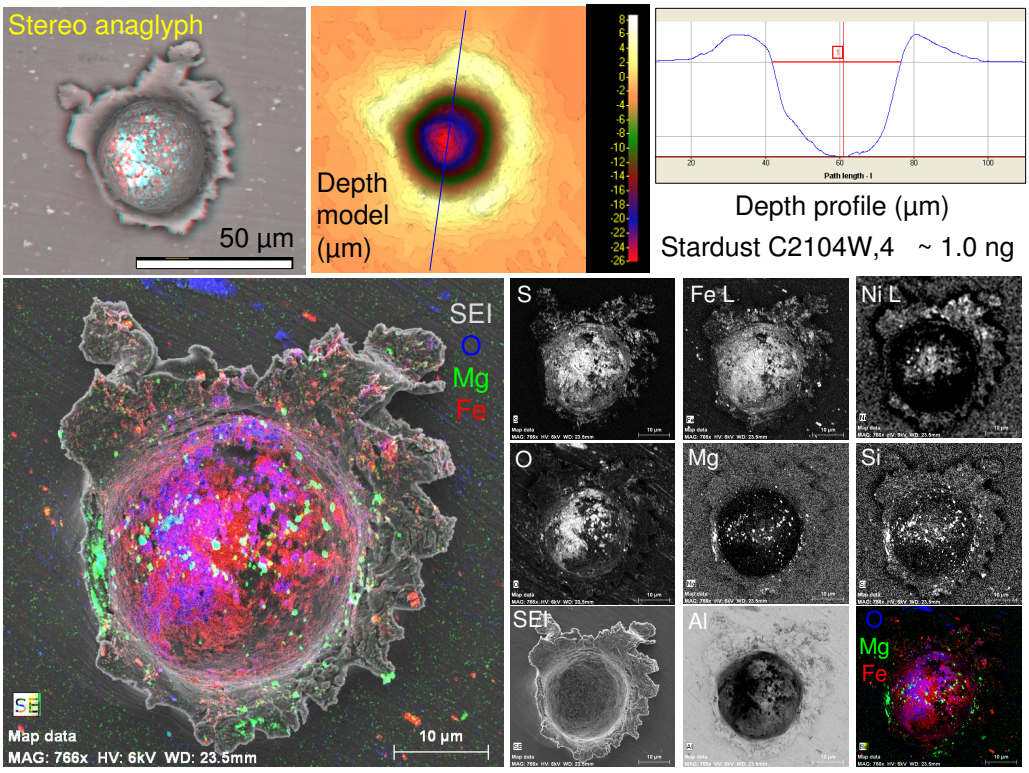
Stereo anaglyph
50 µm
Depth model (µm)
Depth profile (µm)
Stardust C2104W,4 ~ 1.0 ng
SEI
O
Mg
Fe
Map data
MAG: 766x HV: 6kV WD: 23.5mm
10 µm
S
Fe L
Ni L
O
Mg
Si
SEI
Al
O
Mg
Fe

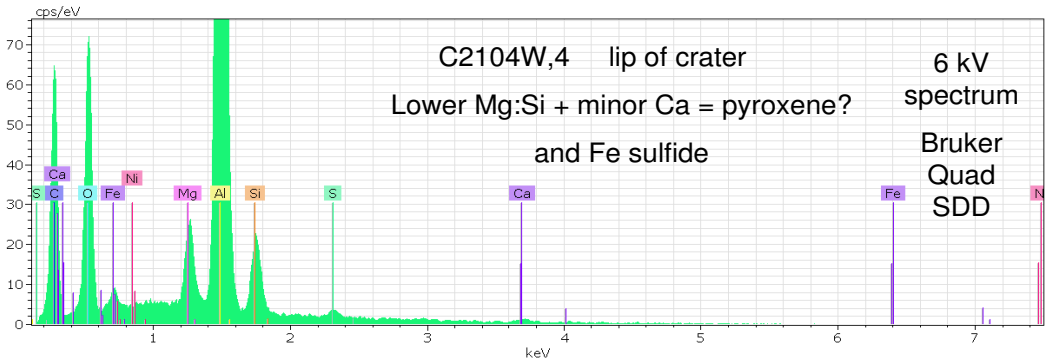
cps/eV
C2104W,4 lip of crater
Lower Mg:Si + minor Ca = pyroxene?
and Fe sulfide
6 kV spectrum
Bruker Quad SDD
keV

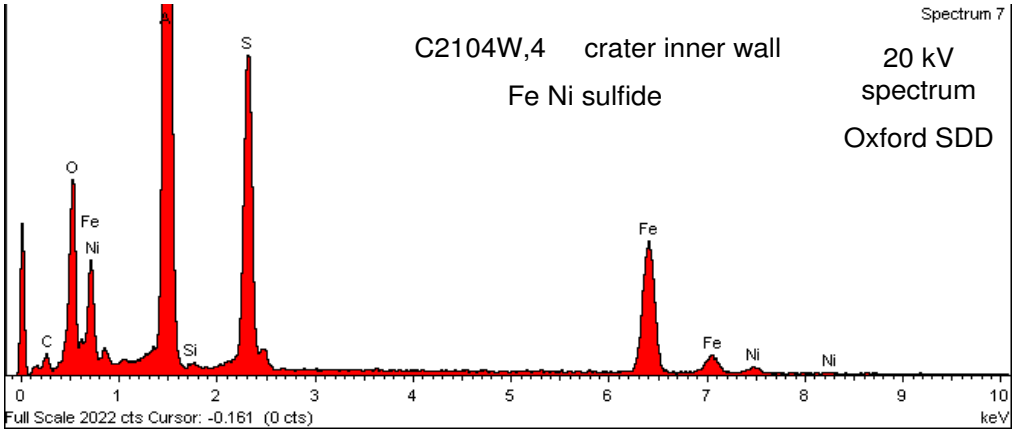
Spectrum 7
C2104W,4 crater inner wall
Fe Ni sulfide
20 kV spectrum
Oxford SDD
Full Scale 2022 cts Cursor: -0.161 (0 cts)
keV

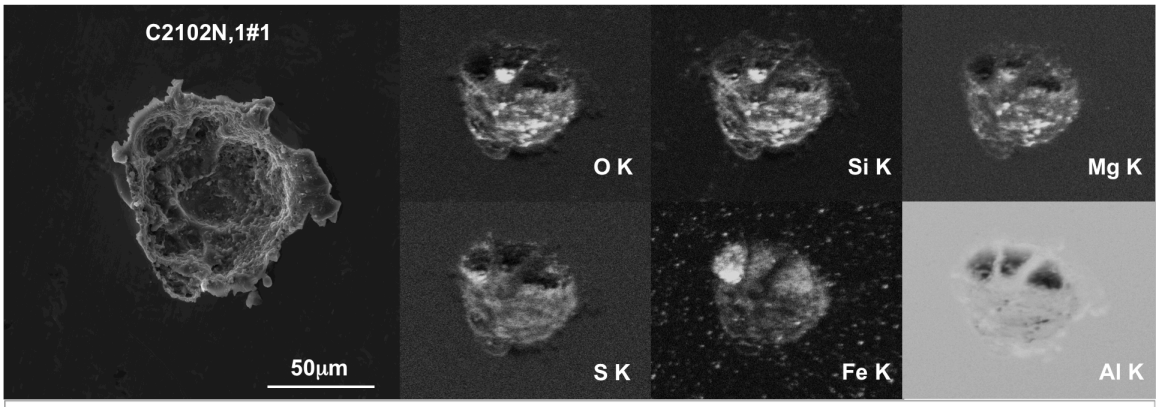

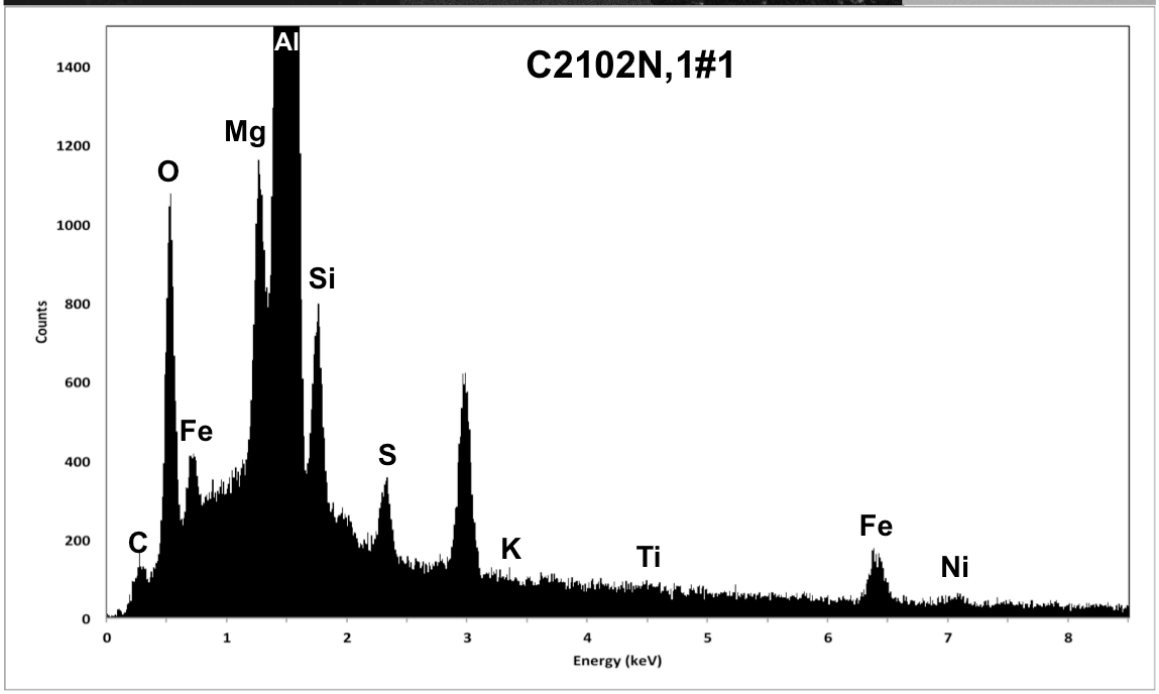

Element	Weight %	Mole %	Error %	Net Int.	K Ratio	Z	R	A	F
Mg O	2.88	6.76	6.96	687.96	0.0147	0.9797	1.01	0.5666	1.0211
Al 2O3	91.17	84.69	4.16	22345.96	0.4746	0.9435	1.017	0.6977	1.0022
Si O2	3.52	5.54	8.2	482.53	0.0102	0.9643	1.0236	0.4287	1.0028
S O3	1.32	1.56	11.28	182.06	0.0049	0.9444	1.0356	0.6505	1.0061
K 2O	0.04	0.04	59.6	11.88	0.0004	0.8941	1.0512	0.8782	1.0182
Ca O	0.03	0.04	60.64	5.64	0.0002	0.9104	1.0558	0.9199	1.0244
Ti O2	0.08	0.1	57.43	13.76	0.0006	0.8252	1.0639	0.9705	1.0475
Fe O	0.86	1.14	12.08	111.48	0.0091	0.8116	1.0751	1.0061	1.1161
Ni O	0.1	0.13	58.01	10.36	0.0011	0.8188	1.0771	1.0096	1.175

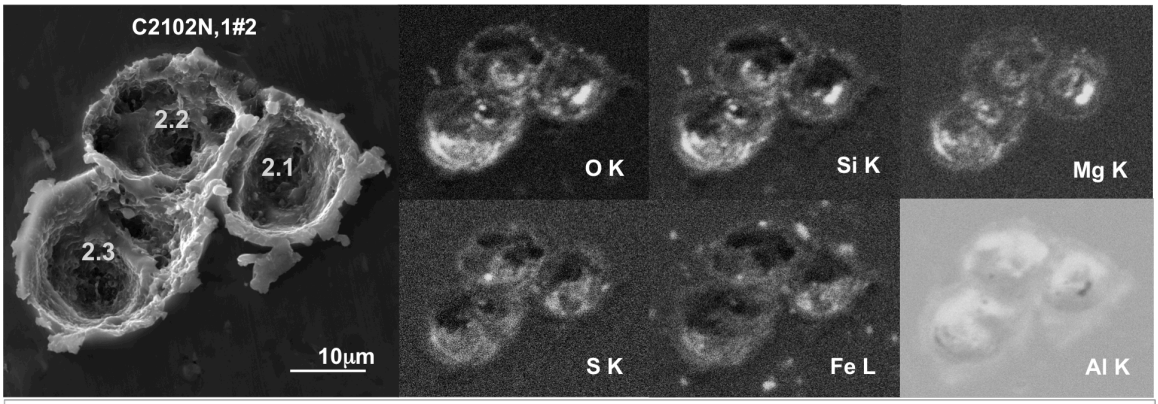

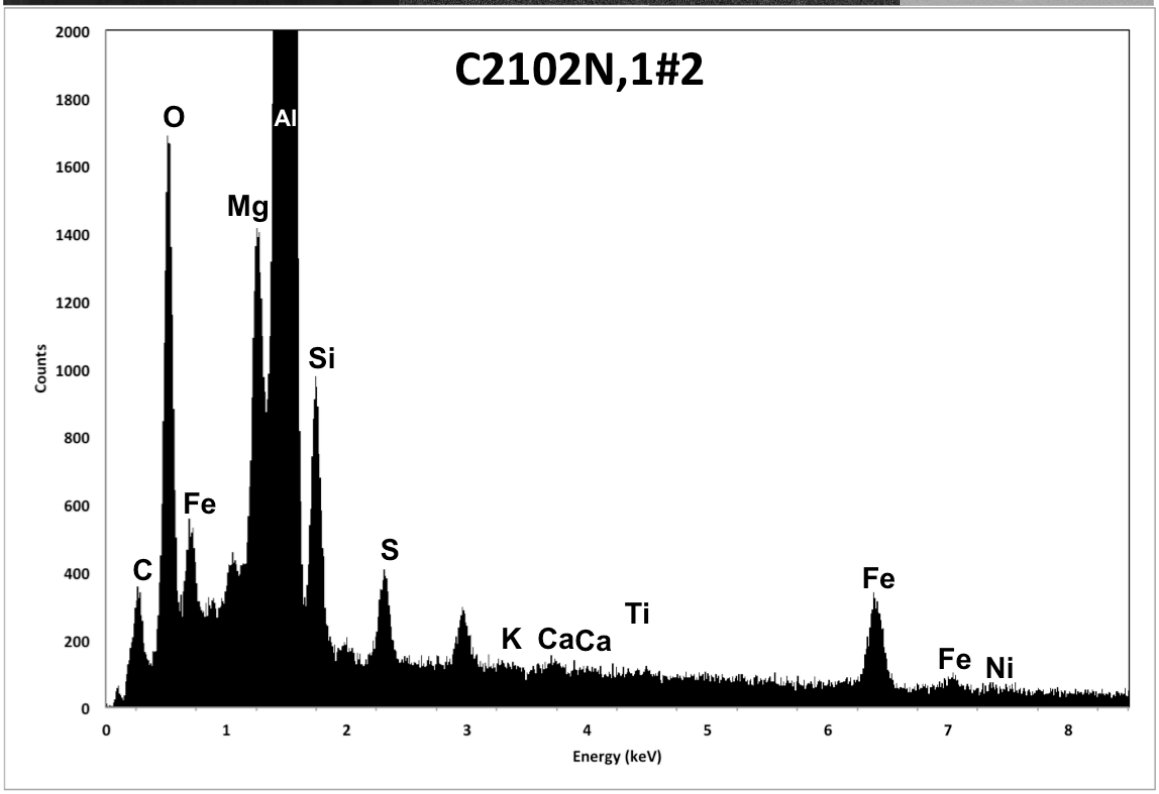

Element	Weight %	Mole %	Error %	Net Int.	K Ratio	Z	R	A	F
C O2	13.49	25.05	13.12	33.35	0.0091	1.0967	0.959	0.1413	1
Na 2O	0.8	1.05	12.2	38.42	0.0034	0.9542	1.0056	0.3718	1.0096
Mg O	2.54	5.16	6.92	184.67	0.0129	0.9706	1.013	0.5363	1.0178
Al 2O3	78.26	62.71	4.37	5958.61	0.4144	0.9347	1.0198	0.6734	1.0022
Si O2	2.37	3.23	8.18	111.41	0.0077	0.9552	1.0263	0.4554	1.003
S O3	0.8	0.81	10.1	37.03	0.0032	0.9355	1.0382	0.6801	1.0066
Ca O	0.12	0.18	21.47	8.76	0.0012	0.9017	1.058	0.9344	1.0267
Ti O2	0.16	0.17	20.86	8.6	0.0013	0.8173	1.066	0.979	1.0518
Fe O	1.3	1.48	6.06	54.25	0.0145	0.8038	1.0768	1.0091	1.1184
Ni O	0.15	0.17	40.1	5.11	0.0018	0.8109	1.0786	1.0109	1.1768

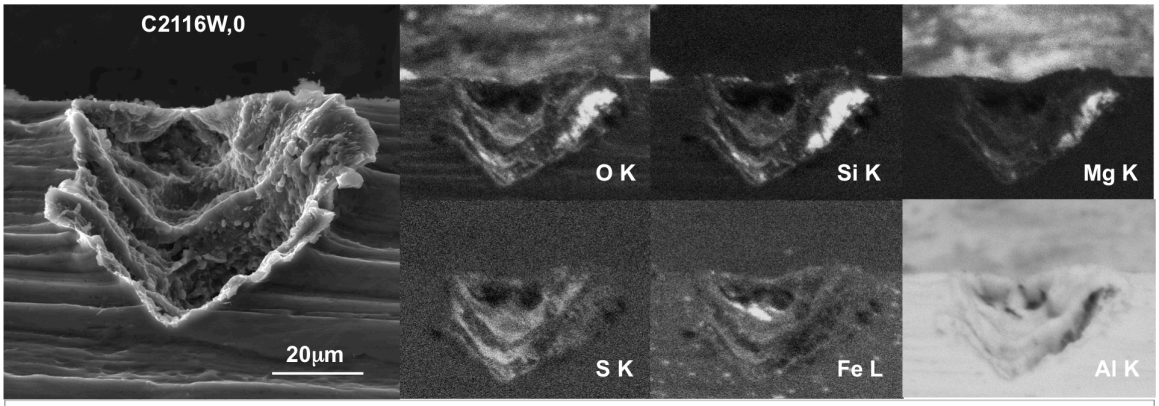

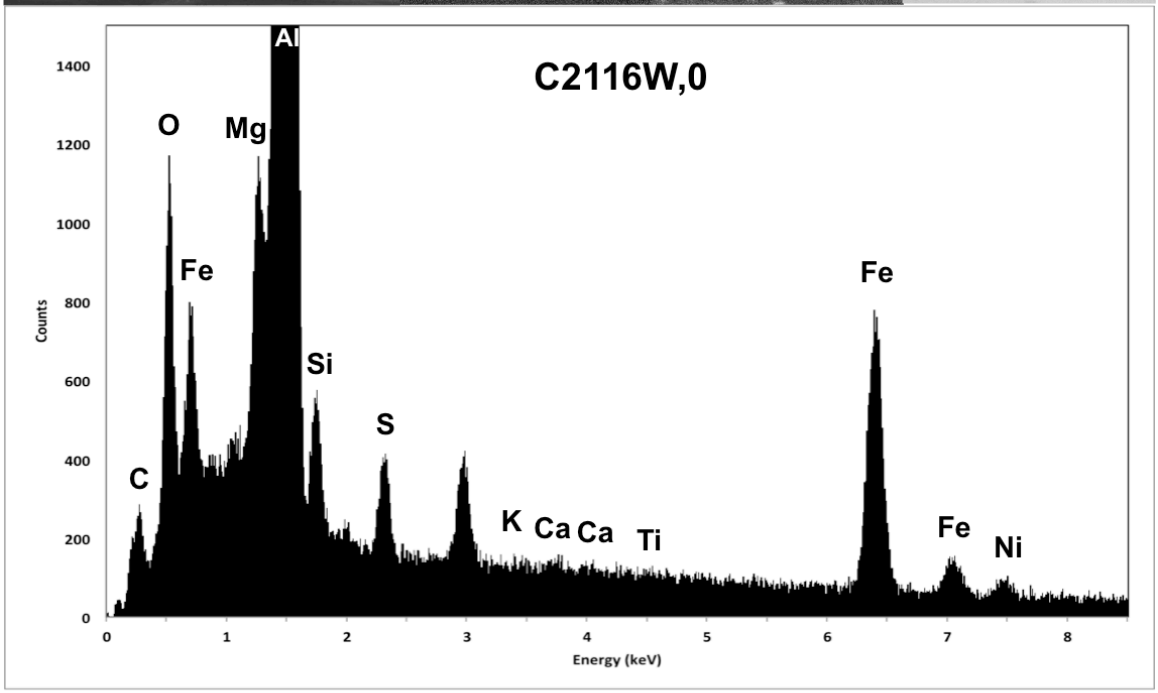

Element	Weight %	Mole %	Error %	Net Int.	K Ratio	Z	R	A	F
C O2	9.44	18.52	14.32	29.14	0.0061	1.1024	0.9562	0.138	1
Na 2O	0.68	0.94	12.48	41.03	0.0028	0.9596	1.0032	0.3658	1.0095
Mg O	1.78	3.82	7.32	163.48	0.0089	0.9761	1.0106	0.5294	1.018
Al 2O3	82.66	69.99	4.37	8037.27	0.4342	0.94	1.0176	0.6722	1.0021
Si O2	1.17	1.68	9.29	68.29	0.0037	0.9607	1.0241	0.4428	1.0031
S O3	0.68	0.73	10.05	39.88	0.0027	0.941	1.0362	0.6713	1.0069
Ca O	0.07	0.11	49.33	6.53	0.0007	0.9071	1.0562	0.9304	1.0288
Ti O2	0.11	0.12	37.33	7.28	0.0009	0.8222	1.0643	0.9767	1.0568
Fe O	3.14	3.77	3.84	165.51	0.0344	0.8087	1.0755	1.0083	1.1045
Ni O	0.28	0.32	25.87	11.71	0.0032	0.8159	1.0774	1.0083	1.1535

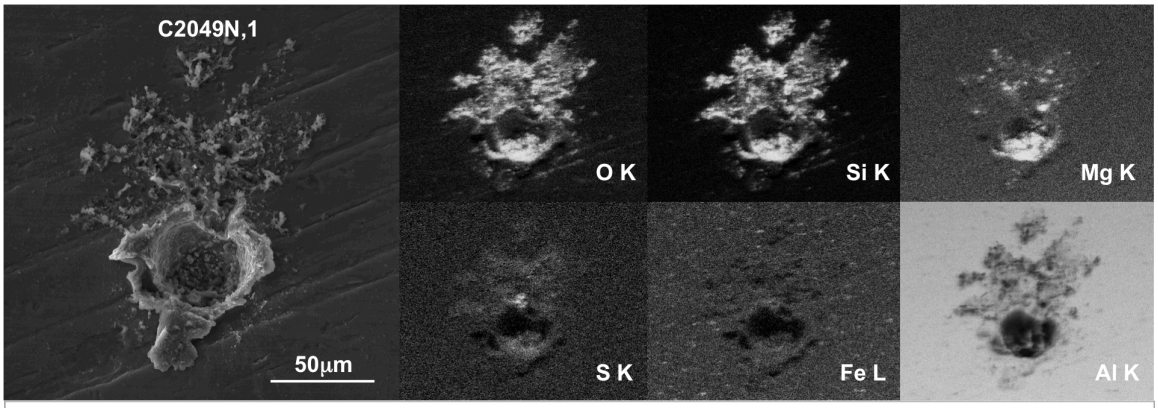

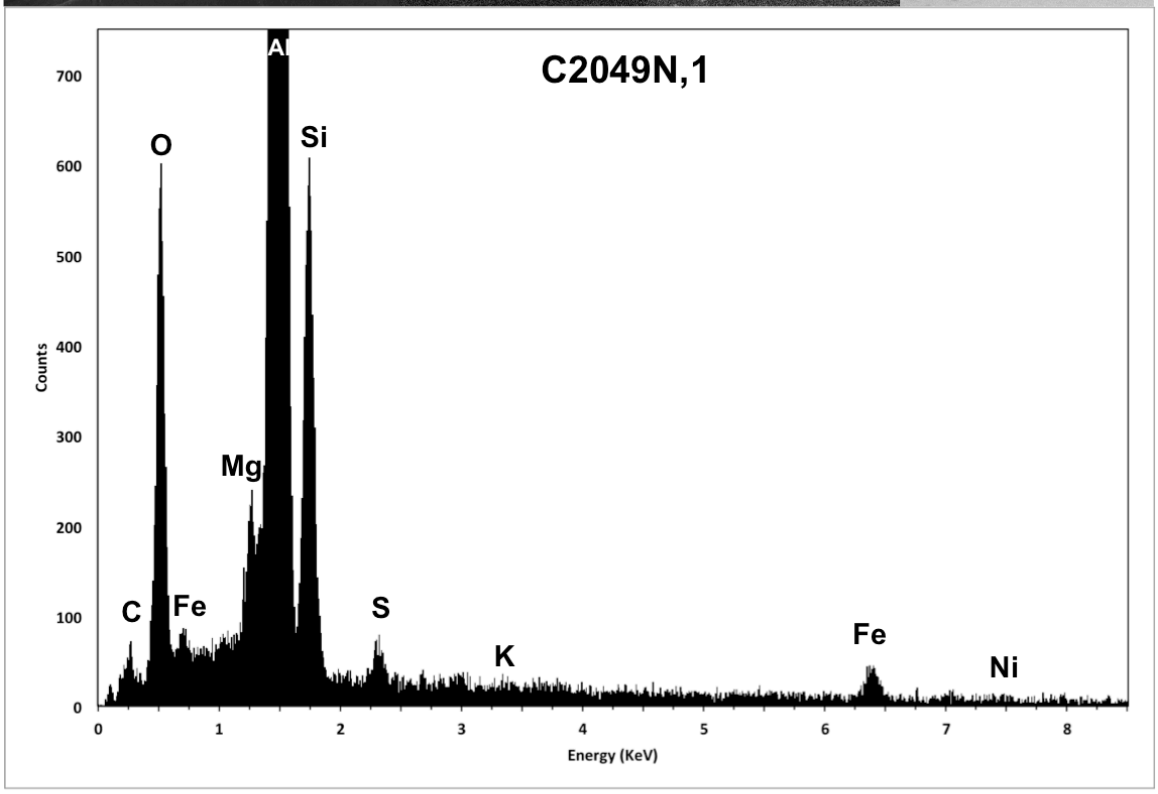

Element	Weight %	Mole %	Error %	Net Int.	K Ratio	Z	R	A	F
C O2	12.01	21.99	15.29	12.13	0.0077	1.0964	0.9589	0.1385	1
Na 2O	0.68	0.88	16.37	13.68	0.0028	0.954	1.0055	0.3745	1.0095
Mg O	2.75	5.5	7.5	83.8	0.0136	0.9703	1.0129	0.5403	1.0176
Al 2O3	74.95	59.23	4.45	2387.81	0.3874	0.9344	1.0197	0.6756	1.0028
Si O2	7.71	10.34	7.58	154.27	0.0248	0.955	1.0262	0.466	1.0029
S O3	0.66	0.67	14.91	12.76	0.0026	0.9352	1.0381	0.6739	1.0064
Ca O	0.08	0.11	59.08	2.23	0.0007	0.9015	1.0579	0.932	1.0258
Ti O2	0.06	0.06	59.7	1.26	0.0004	0.817	1.0659	0.9777	1.0503
Fe O	0.94	1.06	11.79	16.46	0.0103	0.8035	1.0768	1.0088	1.121
Ni O	0.16	0.17	58.34	2.2	0.0018	0.8107	1.0786	1.0111	1.1805

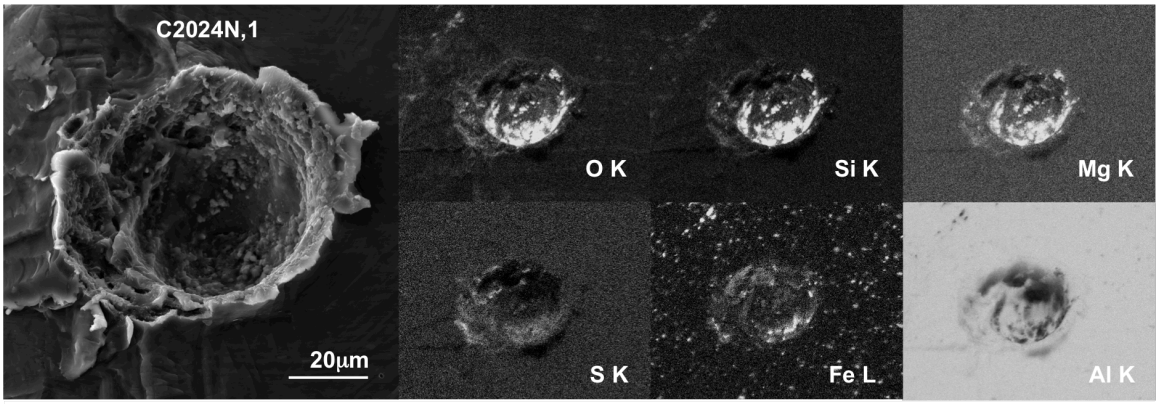

C2024N,1

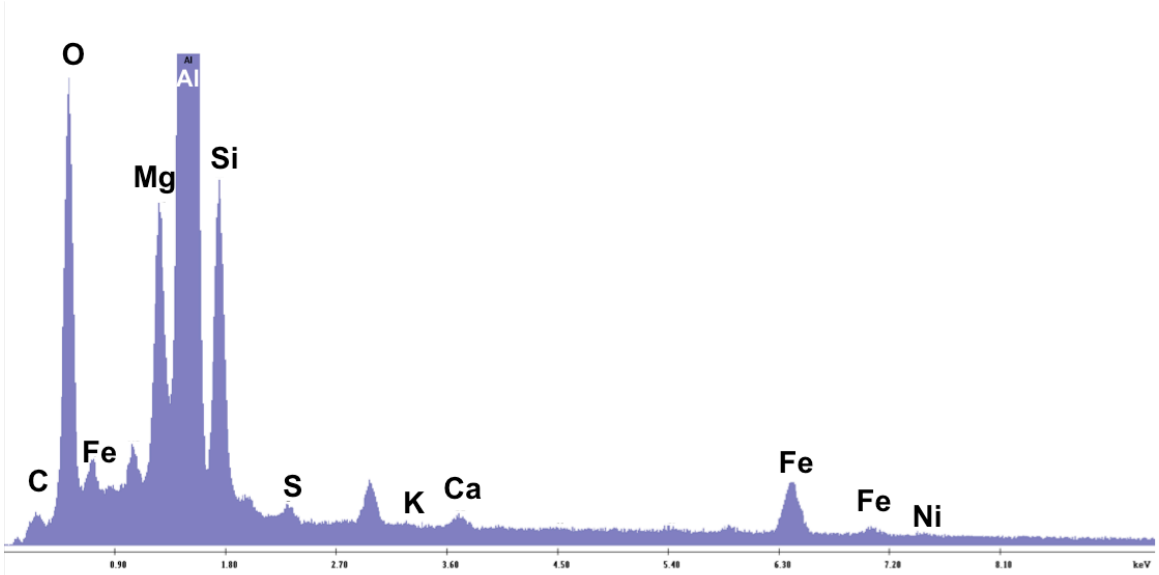

Element	Weight %	Mole %	Error %	Net Int.	K Ratio	Z	R	A	F
C O2	8.68	16.18	99.99	27.32	0.0054	1.1005	0.957	0.1367	1
Na 2O	1.65	2.18	8.9	105.62	0.0067	0.9578	1.0039	0.375	1.0092
Mg O	4.03	8.2	6.35	382.04	0.0194	0.9742	1.0113	0.5326	1.0166
Al 2O3	76.01	61.15	4.5	7447.87	0.376	0.9382	1.0182	0.6577	1.0027
Si O2	6.55	8.95	6.97	405.22	0.0203	0.9589	1.0248	0.4559	1.003
S O3	0.61	0.63	12.33	36.83	0.0023	0.9391	1.0367	0.6685	1.0067
K 2O	0.04	0.04	45.36	5.32	0.0004	0.889	1.0522	0.8901	1.0203
Ca O	0.19	0.27	18.05	17.39	0.0017	0.9053	1.0567	0.9293	1.0268
Cr 2O3	0.23	0.13	9.75	14.61	0.0021	0.812	1.0713	0.998	1.0901
Fe O	1.81	2.07	4.38	98.99	0.0192	0.807	1.0759	1.0077	1.1116
Ni O	0.19	0.21	31.14	8.46	0.0022	0.8142	1.0778	1.0095	1.1658

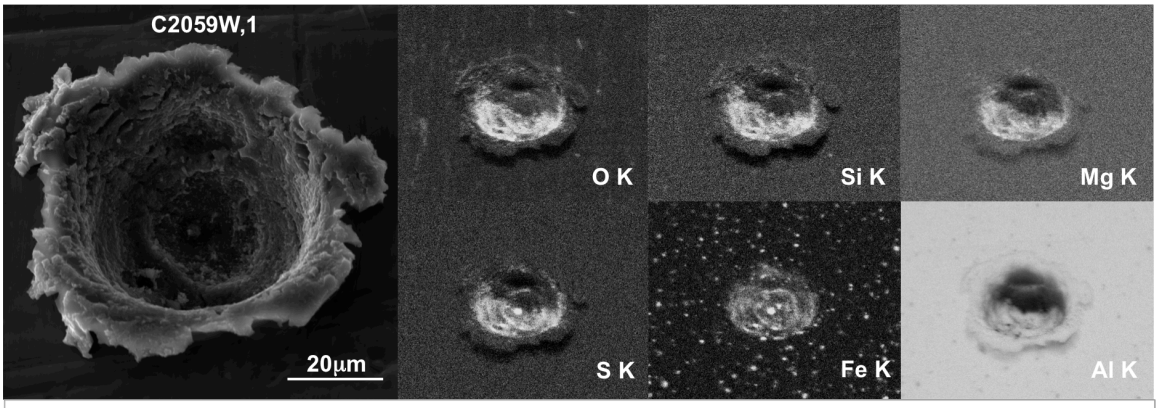

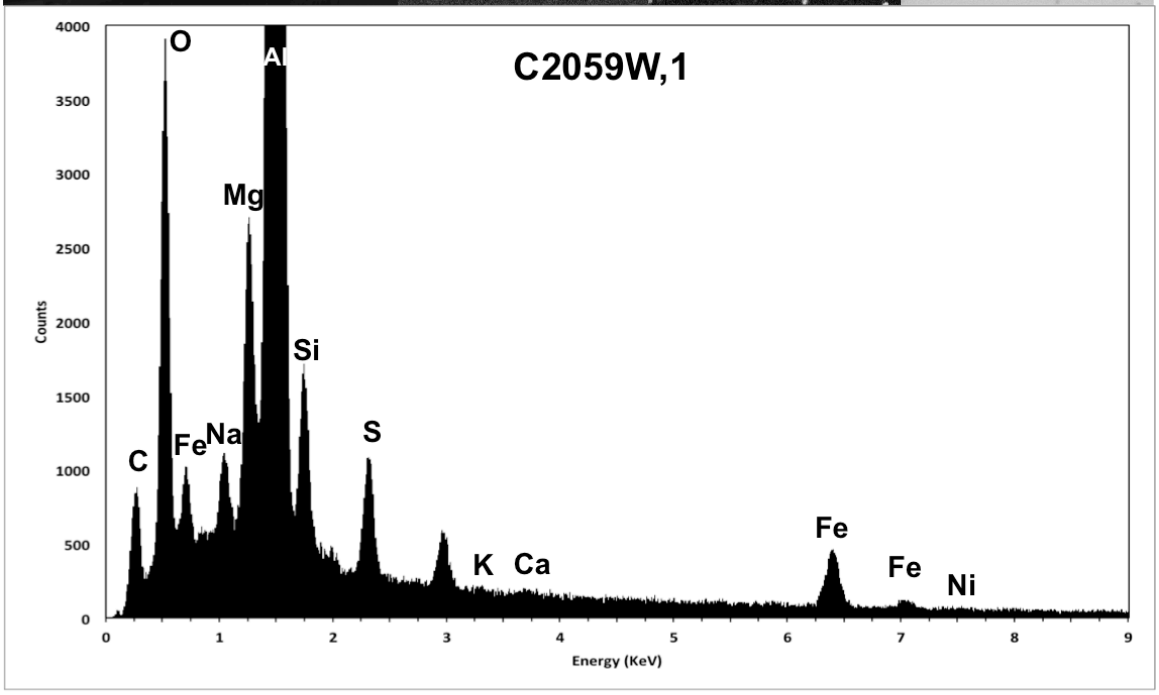

Element	Weight %	Mole %	Error %	Net Int.	K Ratio	Z	R	A	F
C O2	23.08	38.47	57.89	134.02	0.0174	1.0886	0.9622	0.1533	1
Na 2O	1.94	2.3	8.97	196.98	0.0083	0.9468	1.0083	0.3616	1.0083
Mg O	2.97	5.4	6.72	448.51	0.015	0.963	1.0156	0.5171	1.0151
Al 2O3	66.32	47.7	4.56	10595.31	0.3532	0.9273	1.0224	0.6527	1.0024
Si O2	2.69	3.28	7.17	289.74	0.0096	0.9477	1.0288	0.4828	1.0033
S O3	1.75	1.6	5.58	182.57	0.0077	0.928	1.0405	0.7051	1.0068
K 2O	0.04	0.03	41.6	9.06	0.0005	0.8785	1.0556	0.9084	1.0204
Ca O	0.04	0.06	56.13	6.77	0.0004	0.8945	1.06	0.9437	1.0274
Cr 2O3	0.06	0.03	49.74	6.15	0.0006	0.8022	1.074	1.0035	1.0921
Fe O	1.1	1.12	5.69	100.14	0.0128	0.7972	1.0783	1.0113	1.1236

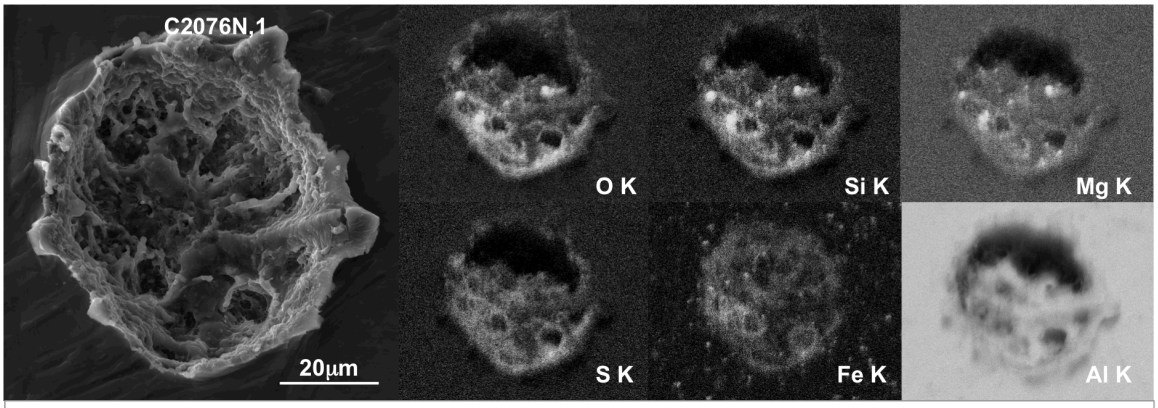

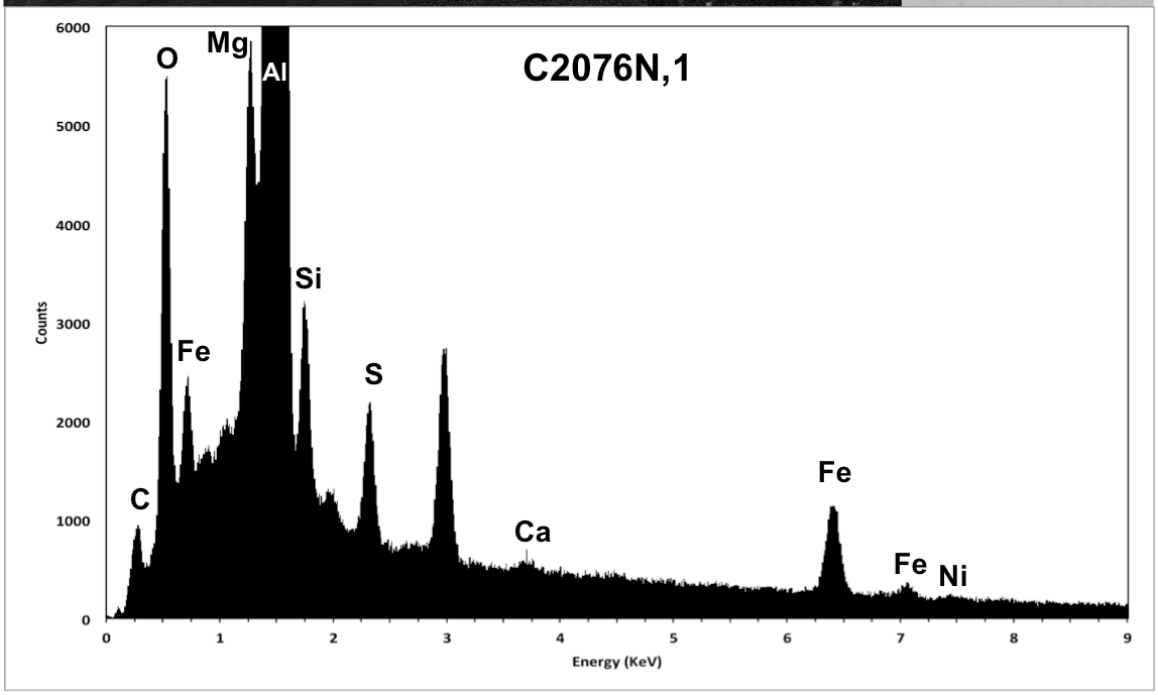

Element	Weight %	Mole %	Error %	Net Int.	K Ratio	Z	R	A	F
C O2	8.58	16.7	15.87	62.68	0.0056	1.1028	0.956	0.1371	1
Na 2O	1.3	1.79	8.67	188.54	0.0055	0.9599	1.0031	0.3682	1.0091
Mg O	2.46	5.22	6.42	534.65	0.0124	0.9764	1.0105	0.5274	1.0169
Al 2O3	80.82	67.85	4.39	18508.61	0.4269	0.9404	1.0175	0.6648	1.0021
Si O2	2.04	2.9	7.27	284.33	0.0065	0.9611	1.024	0.4451	1.0029
S O3	1.28	1.37	5.7	178.94	0.0052	0.9413	1.036	0.6712	1.0062
K 2O	0.03	0.03	37.12	8.8	0.0003	0.8911	1.0516	0.89	1.0185
Ca O	0.07	0.11	26.51	14.95	0.0007	0.9074	1.0561	0.9293	1.0245
Ti O2	0.07	0.07	34.29	10.98	0.0006	0.8225	1.0642	0.9761	1.0475
Cr 2O3	0.04	0.02	54.71	5.71	0.0004	0.814	1.0708	0.9981	1.08
Fe O	3.31	3.94	8.34	91.56	0.0114	0.8294	1.1329	0.3353	0.9972

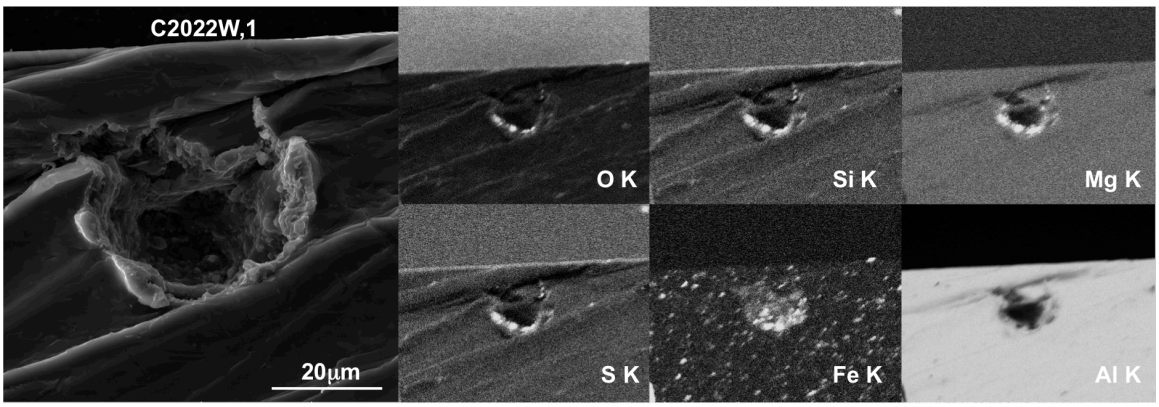

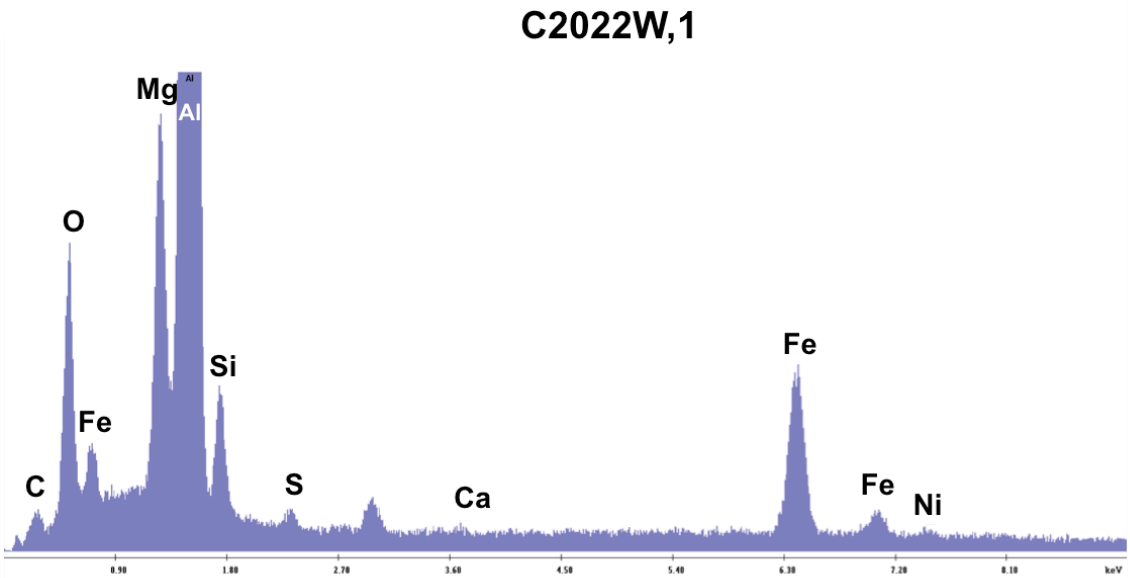

Element	Weight %	Mole %	Error %	Net Int.	K Ratio	Z	R	A	F
C O2	9.18	17.17	16.04	15.51	0.0062	1.1046	0.9542	0.1403	1
Na 2O	0.74	0.98	13.23	23.33	0.003	0.9618	1.0015	0.3539	1.0082
Mg O	4.79	9.78	6.91	229.18	0.0235	0.9783	1.009	0.5147	1.0146
Al 2O3	76.39	61.66	4.79	3782.38	0.3859	0.9422	1.016	0.6358	1.0022
Si O2	2.46	3.38	8.69	78.08	0.0079	0.963	1.0226	0.4465	1.0029
S O3	0.42	0.43	18.04	13.17	0.0017	0.9433	1.0347	0.6717	1.0066
Ca O	0.11	0.16	39.96	5.24	0.0011	0.9094	1.055	0.9308	1.0264
Ti O2	0.22	0.23	16.91	7.99	0.0018	0.8243	1.0632	0.9768	1.0507
Cr 2O3	0.45	0.25	9.62	14.65	0.0043	0.8158	1.0699	0.9982	1.0819
Fe O	4.56	5.23	10.36	28.59	0.0157	0.8309	1.131	0.3359	0.9972
Ni O	0.67	0.74	12	15.73	0.0082	0.8182	1.0766	1.0062	1.183

Appendix B: Cosmic Dust Catalog, Vol. 18 Images and EDS Spectra for Interplanetary Dust Particles

L2083 E47

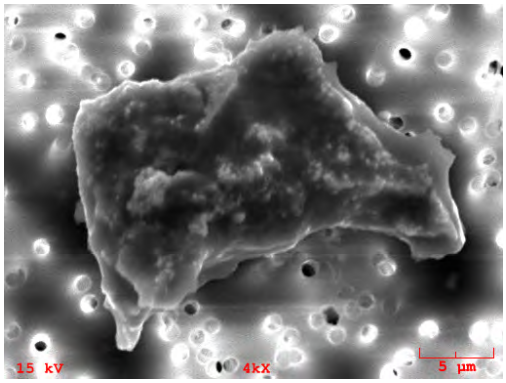

Particle Size: 23x15
Shape: Irregular
Transparency: Opaque
Color: Black
Luster: Submetallic
Particle Type: C - Cosmic
Comments:

Particle EDS Spectra

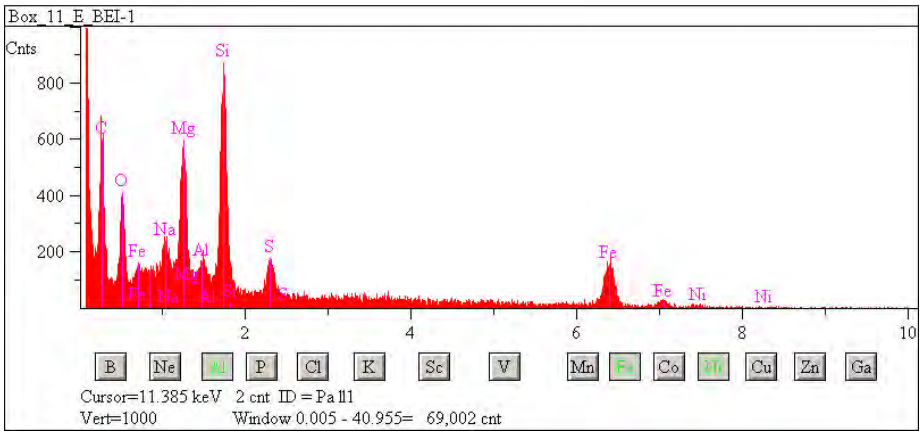

L2071 E35

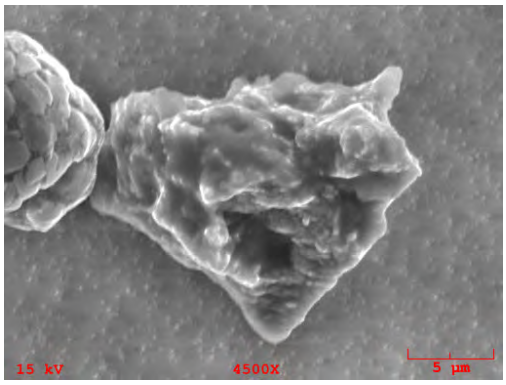

Particle Size: 20x17
Shape: Irregular
Transparency: Opaque
Color: Black
Luster: Submetallic to Dull
Particle Type: C - Cosmic
Comments:

Particle EDS Spectra

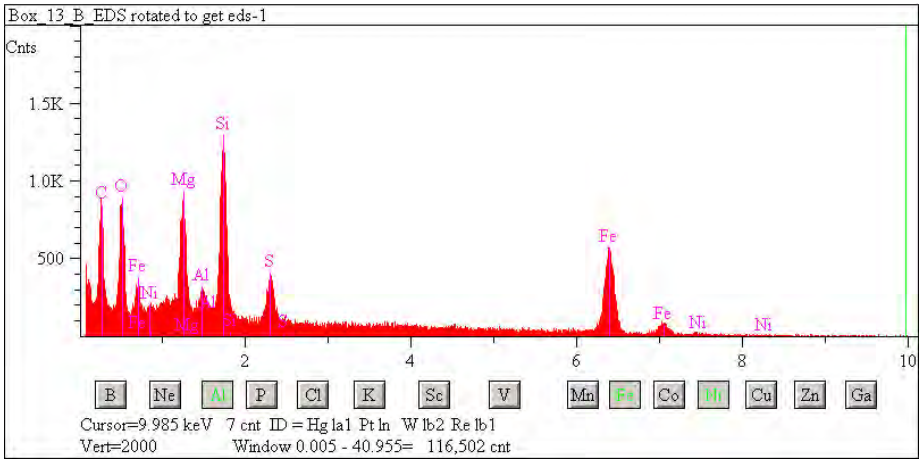

L2079 C35

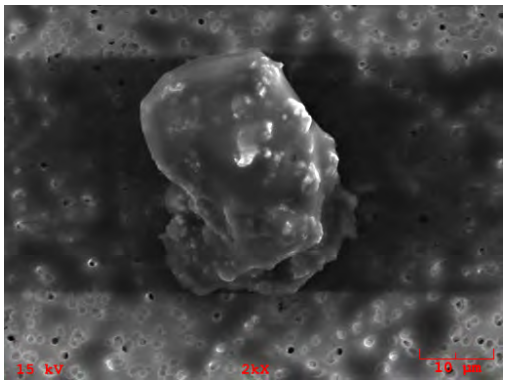

Particle Size: 30x20

Shape: Irregular

Transparency: Opaque

Color: Black, Brown

Luster: Subvitreous

Particle Type: C - Cosmic

Comments:

Particle EDS Spectra

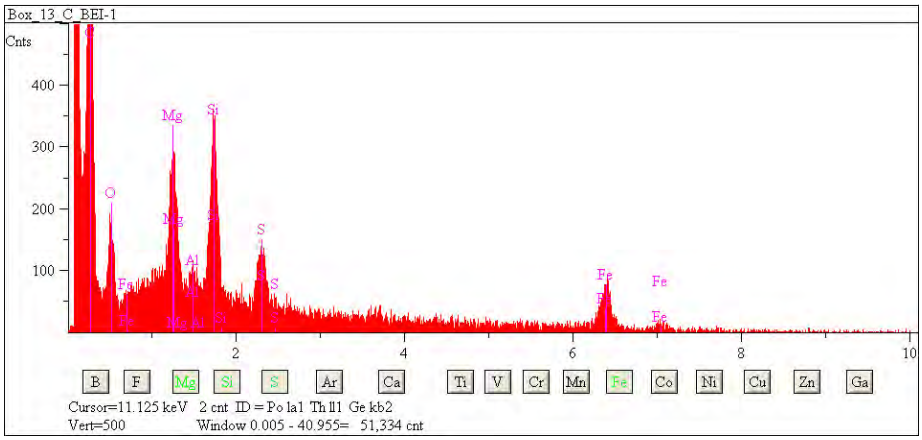

L2083 D46

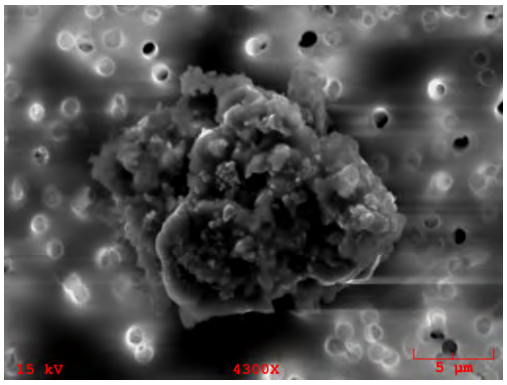

Particle Size: 18x15

Shape: Irregular

Transparency: Opaque

Color: Black

Luster: Subvitreous to Dull

Particle Type: C - Cosmic

Comments:

Particle EDS Spectra

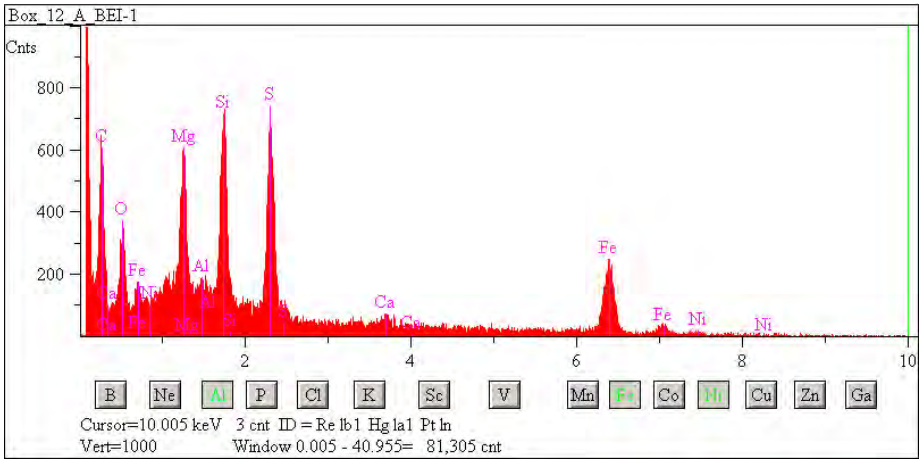

L2083 E46

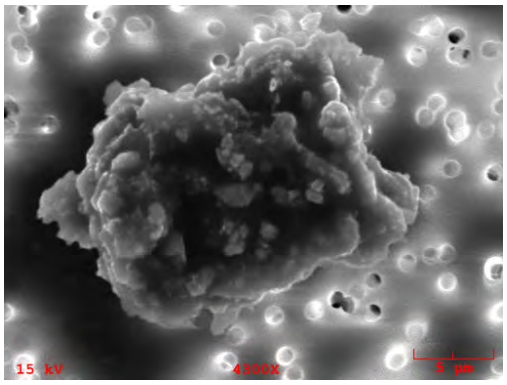

Particle Size: 23x16
Shape: Irregular
Transparency: Opaque
Color: Black
Luster: Submetallic
Particle Type: C - Cosmic
Comments:

Particle EDS Spectra

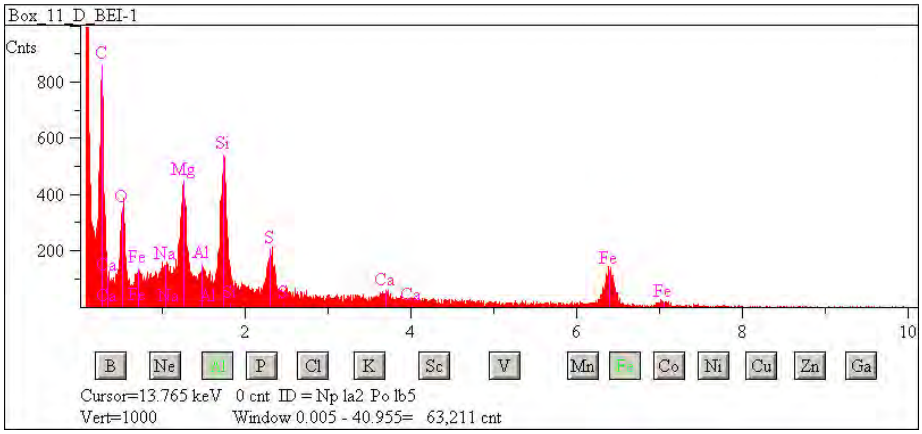

Bibliography:

Aleon, J., C. Engrand, L. A. Leshin, and K. D. McKeegan. 2009. 'Oxygen isotopic composition of chondritic interplanetary dust particles: A genetic link between carbonaceous chondrites and comets', *Geochimica et Cosmochimica Acta*, 73: 4558-75.

Altwegg, K., H. Balsiger, A. Bar-Nun, J. J. Berthelier, A. Bieler, P. Bochsler, C. Briois, U. Calmonte, M. Combi, J. De Keyser, P. Eberhardt, B. Fiethe, S. Fuselier, S. Gasc, T. I. Gombosi, K. C. Hansen, M. Hassig, A. Jackel, E. Kopp, A. Korth, L. Leroy, U. Mall, B. Marty, O. Mousis, E. Neefs, T. Owen, H. Reme, M. Rubin, T. Semon, C. Y. Tzou, H. Waite, and P. Wurz. 2015. '67P/Churyumov-Gerasimenko, a Jupiter family comet with a high D/H ratio', *Science*, 347.

Berger, E. L., T. J. Zega, L. P. Keller, and D. S. Lauretta. 2011. 'Evidence for aqueous activity on comet 81P/Wild 2 from sulfide mineral assemblages in Stardust samples and CI chondrites', *Geochimica et Cosmochimica Acta*, 75: 3501-13.

Bradley, J. 2010. 'The Astromineralogy of Interplanetary Dust Particles', *Astromineralogy, Second Edition*, 815: 259-76.

Bradley, J. P., and D. E. Brownlee. 1991. 'An Interplanetary Dust Particle Linked Directly to Type-Cm Meteorites and an Asteroidal Origin', *Science*, 251: 549-52.

Bradley, J.P. 1991. 'Physical and mineralogical properties of anhydrous interplanetary dust particles in the analytical electron microscope.' in A.C. Levasseur-Regourd and H. Hasegawa (eds.), *Origin and evolution of interplanetary dust* (Kluwer Academic Publishers).

Bradley, John P. 2013. 'How and where did GEMS form?', *Geochimica et Cosmochimica Acta*,

107: 336-40.

Bradley, John P., Donald E. Brownlee, and D. R. Veblen. 1983. 'Pyroxene whiskers and platelets in interplanetary dust: Evidence for vapour phase growth', *Nature*, 310: 473-77.

Bradley, JP, and ZR Dai. 2004. 'Mechanism of formation of glass with embedded metal and sulfides', *The Astrophysical Journal*, 617: 650.

Brownlee, D. 2014. 'The Stardust Mission: Analyzing Samples from the Edge of the Solar System', *Annual Review of Earth and Planetary Sciences, Vol 42*, 42: 179-205.

Brownlee, D. E. 1985a. 'COSMIC DUST - COLLECTION AND RESEARCH', *Annual Review of Earth and Planetary Sciences*, 13: 147-73.

Brownlee, D. E., D. J. Joswiak, D. J. Schlutter, R. O. Pepin, J. P. Bradley, and S. G. Love. 1995. 'Identification of individual cometary IDPs by thermally stepped He release', *LPSC*, XXVI: 183-84.

Brownlee, DE. 2005. 'Comets', *Meteorites, Comets and Planets: Treatise on Geochemistry, Volume 1. Edited by AM Davis. Executive Editors: HD Holland and KK Turekian. ISBN 0-08-044720-1. Published by Elsevier BV, Amsterdam, The Netherlands, 2005, p. 663*, 1: 663.

Brownlee, Donald E. 1985b. 'Cosmic dust: collection and research', *Ann Rev. Earth Planet. Sci.*, 13: 147-73.

Burchell, M. J., M. J. Cole, S. F. Lascelles, M. A. Khan, C. Barthet, S. A. Wilson, D. B. Cairns, and S. P. Armes. 1999. 'Acceleration of conducting polymer-coated latex particles as projectiles in hypervelocity impact experiments', *Journal of Physics D-Applied Physics*, 32: 1719-28.

Burchell, M. J., N. J. Foster, A. T. Kearsley, and J. A. Creighton. 2008. 'Identification of mineral

impactors in hypervelocity impact craters in aluminum by Raman spectroscopy of residues', *Meteoritics & Planetary Science*, 43: 135-42.

Busemann, Henner, Ann N Nguyen, George D Cody, Peter Hoppe, AL David Kilcoyne, Rhonda M Stroud, Thomas J Zega, and Larry R Nittler. 2009. 'Ultra-primitive interplanetary dust particles from the comet 26P/Grigg–Skjellerup dust stream collection', *Earth and Planetary Science Letters*, 288: 44-57.

Choi, B. G., K. D. McKeegan, A. N. Krot, and J. T. Wasson. 1998. 'Extreme oxygen-isotope compositions in magnetite from unequilibrated ordinary chondrites', *Nature*, 392: 577-79.

Ciesla, FJ, and SB Charnley. 2006. 'The physics and chemistry of nebular evolution', *Meteorites and the early solar system II*, 943: 209-30.

Clayton, D. D. 1988. 'Isotopic anomalies: Chemical memory of galactic evolution', *Astrophysical Journal*, 334: 191-95.

Clayton, R. N. 2002a. 'Photochemical self-shielding in the solar nebula', *Lunar Planet. Sci.*, XXXIII: #1326 (CD-ROM).

———. 2002b. 'Self-shielding in the solar nebula', *Nature*, 415: 860-61.

Clayton, R. N., T. K. Mayeda, and D. E. Brownlee. 1986. 'Oxygen Isotopes in Deep-Sea Spherules', *Earth and Planetary Science Letters*, 79: 235-40.

Clayton, Robert N. 1993. 'Oxygen isotopes in meteorites', *Annual Review of Earth and Planetary Sciences*, 21: 115-49.

Clayton, Robert N., L. Grossman, and Toshiko K. Mayeda. 1973. 'A component of primitive nuclear composition in carbonaceous meteorites', *Science*, 182: 485-88.

Clayton, Robert N., and Toshiko K. Mayeda. 1977. 'Correlated oxygen and magnesium isotope anomalies in Allende inclusions, I: Oxygen', *Geophysical Research Letters*, 4: 295-98.

———. 1999. 'Oxygen isotope studies of carbonaceous chondrites', *Geochimica et Cosmochimica Acta*, 63: 2089-104.

Davis, A. M., and K. D. McKeegan. 2014. '1.11 - Short-Lived Radionuclides and Early Solar System Chronology A2 - Holland, Heinrich D.' in Karl K. Turekian (ed.), *Treatise on Geochemistry (Second Edition)* (Elsevier: Oxford).

De Bergh, C, H Boehnhardt, MA Barucci, M Lazzarin, S Fornasier, J Romon-Martin, GP Tozzi, A Doressoundiram, and E Dotto. 2004. 'Aqueous altered silicates at the surface of two Plutinos?', *Astronomy & Astrophysics*, 416: 791-98.

Donn, B., and G. W. Sears. 1963. 'Planets and Comets - Role of Crystal Growth in Their Formation', *Science*, 140: 1209-&.

Fahey, A. J., J. N. Goswami, K. D. McKeegan, and E. K. Zinner. 1987. '^{16}O Excesses in Murchison and Murray Hibonites - a Case against a Late Supernova Injection Origin of Isotopic Anomalies in O, Mg, Ca, and Ti', *Astrophysical Journal*, 323: L91-L95.

Floss, Christine, Frank J Stadermann, Anton T Kearsley, Mark J Burchell, and WJ Ong. 2013. 'The abundance of presolar grains in comet 81P/Wild 2', *The Astrophysical Journal*, 763: 140.

Flynn, G. J., P. Bleuet, J. Borg, J. P. Bradley, F. E. Brenker, S. Brennan, J. Bridges, D. E. Brownlee, E. S. Bullock, M. Burghammer, B. C. Clark, Z. R. Dai, C. P. Daghlian, Z. Djouadi, S. Fakra, T. Ferroir, C. Floss, I. A. Franchi, Z. Gainsforth, J. P. Gallien, P. Gillet, P. G. Grant, G. A. Graham, S. F. Green, F. Grossemy, P. R. Heck, G. F. Herzog, P. Hoppe, F. Horz, J. Huth, K. Ignatyev, H. A. Ishii, K. Janssens, D. Joswiak, A. T. Kearsley, H. Khodja, A. Lanzirotti, J. Leitner, L. Lemelle, H. Leroux, K. Luening, G. J. MacPherson, K. K. Marhas, M. A. Marcus, G. Matrajt, T. Nakamura, K. Nakamura-

Messenger, T. Nakano, M. Newville, D. A. Papanastassiou, P. Pianetta, W. Rao, C. Riekel, F. J. M. Rietmeijer, D. Rost, C. S. Schwandt, T. H. See, J. Sheffield-Parker, A. Simionovici, I. Sitnitsky, C. J. Snead, F. J. Stadermann, T. Stephan, R. M. Stroud, J. Susini, Y. Suzuki, S. R. Sutton, S. Taylor, N. Teslich, D. Troadec, P. Tsou, A. Tsuchiyama, K. Uesugi, B. Vekemans, E. P. Vicenzi, L. Vincze, A. J. Westphal, P. Wozniakiewicz, E. Zinner, and M. E. Zolensky. 2006. 'Elemental compositions of comet 81P/Wild 2 samples collected by Stardust', *Science*, 314: 1731-35.

Flynn, G. J., L. P. Keller, M. Feser, S. Wirick, and C. Jacobsen. 2003. 'The origin of organic matter in the solar system: Evidence from the interplanetary dust particles', *Geochimica et Cosmochimica Acta*, 67: 4791-806.

Fornasier, S., C. Lantz, M. A. Barucci, and M. Lazzarin. 2014. 'Aqueous alteration on main belt primitive asteroids: Results from visible spectroscopy', *Icarus*, 233: 163-78.

Gladman, B. J., F. Migliorini, A. Morbidelli, V. Zappala, P. Michel, A. Cellino, C. Froeschle, H. F. Levison, M. Bailey, and M. Duncan. 1997. 'Dynamical lifetimes of objects injected into asteroid belt resonances', *Science*, 277: 197-201.

Greenberg, J Mayo, and JI Hage. 1990. 'From interstellar dust to comets-A unification of observational constraints', *The Astrophysical Journal*, 361: 260-74.

Greenberg, J. M. 1985. 'The Chemical and Physical Evolution of Interstellar Dust', *Physica Scripta*, T11: 14-26.

Grossman, Lawrence. 1973. 'Refractory trace elements in Ca-Al-rich inclusions in the Allende meteorite', *Geochimica et Cosmochimica Acta*, 37: 1119-40.

Horz, F., R. Bastien, J. Borg, J. P. Bradley, J. C. Bridges, D. E. Brownlee, M. J. Burchell, M. F. Chi, M. J. Cintala, Z. R. Dai, Z. Djouadi, G. Dominguez, T. E. Economou, S. A. J. Fairey,

C. Floss, I. A. Franchi, G. A. Graham, S. F. Green, P. Heck, P. Hoppe, J. Huth, H. Ishii, A. T. Kearsley, J. Kissel, J. Leitner, H. Leroux, K. Marhas, K. Messenger, C. S. Schwandt, T. H. See, C. Snead, F. J. Stadermann, T. Stephan, R. Stroud, N. Teslich, J. M. Trigo-Rodriguez, A. J. Tuzzolino, D. Troadec, P. Tsou, J. Warren, A. Westphal, P. Wozniakiewicz, I. Wright, and E. Zinner. 2006. 'Impact features on Stardust: Implications for comet 81P/Wild 2 dust', *Science*, 314: 1716-19.

Jewitt, D., and J. Luu. 1993. 'Discovery of the Candidate Kuiper Belt Object 1992 Qb(1)', *Nature*, 362: 730-32.

Johnston, J. C., and M. H. Thiemens. 1997. 'The isotopic composition of tropospheric ozone in three environments', *Journal of Geophysical Research-Atmospheres*, 102: 25395-404.

Jones, A. P., A. G. G. M. Tielens, D. J. Hollenbach, and C. F. Mckee. 1994. 'Grain Destruction in Shocks in the Interstellar-Medium', *Astrophysical Journal*, 433: 797-810.

Kearsley, A. T., J. Borg, G. A. Graham, M. J. Burchell, M. J. Cole, H. Leroux, J. C. Bridges, F. Horz, P. J. Wozniakiewicz, P. A. Bland, J. P. Bradley, Z. R. Dai, N. Teslich, T. See, P. Hoppe, P. R. Heck, J. Huth, F. J. Stadermann, C. Floss, K. Marhas, T. Stephan, and J. Leitner. 2008. 'Dust from comet Wild 2: Interpreting particle size, shape, structure, and composition from impact features on the Stardust aluminum foils', *Meteoritics & Planetary Science*, 43: 41-73.

Kearsley, A. T., M. J. Burchell, F. Horz, M. J. Cole, and C. S. Schwandt. 2006. 'Laboratory simulation of impacts on aluminum foils of the Stardust spacecraft: Calibration of dust particle size from comet Wild-2', *Meteoritics & Planetary Science*, 41: 167-80.

Kearsley, A. T., M. J. Burchell, P. Wozniakiewicz, M. J. Cole, G. A. Graham, R. J. Chater, Z. Dai, N. Teslich, F. Horz, and C. Schwandt. 2006. 'Calibration for Stardust craters in

aluminum foil: Interpretation of cometary particle properties by comparison with laboratory impacts of mineral, polymer, and glass grains', *Meteoritics & Planetary Science*, 41: A92-A92.

Kearsley, A. T., G. A. Graham, M. J. Burchell, M. J. Cole, Z. R. Dai, N. Teslich, J. P. Bradley, R. Chater, P. A. Wozniakiewicz, J. Spratt, and G. Jones. 2007. 'Analytical scanning and transmission electron microscopy of laboratory impacts on Stardust aluminum foils: Interpreting impact crater morphology and the composition of impact residues', *Meteoritics & Planetary Science*, 42: 191-210.

Keller, L.P., K.L. Thomas, and D.S. McKay. 1992. 'An interplanetary dust particle with link to CI chondrites', *GCA*, 56: 1409-12.

Keller, Lindsay P, and S Messenger. 2012. 'Formation and processing of amorphous silicates in primitive carbonaceous chondrites and cometary dust'.

Keller, Lindsay P, and Scott Messenger. 2011. 'On the origins of GEMS grains', *Geochimica et Cosmochimica Acta*, 75: 5336-65.

———. 2013. 'On the origins of GEMS grains: A reply', *Geochimica et Cosmochimica Acta*, 107: 341-44.

Keller, LP, KL Thomas, and DS McKay. 1993. 'Carbon abundances, major element chemistry, and mineralogy of hydrated interplanetary dust particles'.

Kita, N. T., T. Ushikubo, B. Fu, and J. W. Valley. 2009. 'High precision SIMS oxygen isotope analysis and the effect of sample topography', *Chemical Geology*, 264: 43-57.

Kobayashi, Sachio, Hajime Imai, and Hisayoshi Yurimoto. 2003. 'New extreme 16O-rich reservoir in the early solar system', *Geochemical Journal*, 37: 663-69.

Krot, A. N., K. Nagashima, F. J. Ciesla, B. S. Meyer, I. D. Hutcheon, A. M. Davis, G. R. Huss,

and E. R. D. Scott. 2010. 'Oxygen Isotopic Composition of the Sun and Mean Oxygen Isotopic Composition of the Protosolar Silicate Dust: Evidence from Refractory Inclusions', *Astrophysical Journal*, 713: 1159-66.

Leitner, J., T. Stephan, A. T. Kearsley, F. Hoerz, G. J. Flynn, and S. A. Sandford. 2008. 'TOF-SIMS analysis of crater residues from Wild 2 cometary particles on Stardust aluminum foil', *Meteoritics & Planetary Science*, 43: 161-85.

Leroux, H., R. M. Stroud, Z. R. Dai, G. A. Graham, D. Troadec, J. P. Bradley, N. Teslich, J. Borg, A. T. Kearsley, and F. Hoerz. 2008. 'Transmission electron microscopy of cometary residues from micron-sized craters in the Stardust Al foils', *Meteoritics & Planetary Science*, 43: 143-60.

Leshin, Laurie A., Alan E. Rubin, and Kevin D. McKeegan. 1997. 'The oxygen isotopic composition of olivine and pyroxene from CI chondrites', *Geochimica et Cosmochimica Acta*, 61: 835-45.

Lisse, C. M., J. VanCleve, A. C. Adams, M. F. A'Hearn, Y. R. Fernandez, T. L. Farnham, L. Armus, C. J. Grillmair, J. Ingalls, M. J. S. Belton, O. Groussin, L. A. McFadden, K. J. Meech, P. H. Schultz, B. C. Clark, L. M. Feaga, and J. M. Sunshine. 2006. 'Spitzer spectral observations of the Deep Impact ejecta', *Science*, 313: 635-40.

Lodders, K. 2003. 'Solar system abundances and condensation temperatures of the elements', *Astrophysical Journal*, 591: 1220-47.

Luu, J. X., and D. C. Jewitt. 2002. 'Kuiper belt objects: Relics from the accretion disk of the sun', *Annual Review of Astronomy and Astrophysics*, 40: 63-101.

Lyons, J. R., and E. D. Young. 2005. 'CO self-shielding as the origin of oxygen isotope anomalies in the early solar nebula', *Nature*, 435: 317-20.

Lyons, Louis. 1991. *A practical guide to data analysis for physical science students* (Cambridge University Press: Cambridge England ; New York).

McKeegan, K. D., J. Aleon, J. Bradley, D. Brownlee, H. Busemann, A. Butterworth, M. Chaussidon, S. Fallon, C. Floss, J. Gilmour, M. Gounelle, G. Graham, Y. B. Guan, P. R. Heck, P. Hoppe, I. D. Hutcheon, J. Huth, H. Ishii, M. Ito, S. B. Jacobsen, A. Kearsley, L. A. Leshin, M. C. Liu, I. Lyon, K. Marhas, B. Marty, G. Matrajt, A. Meibom, S. Messenger, S. Mostefaoui, S. Mukhopadhyay, K. Nakamura-Messenger, L. Nittler, R. Palma, R. O. Pepin, D. A. Papanastassiou, F. Robert, D. Schlutter, C. J. Snead, F. J. Stadermann, R. Stroud, P. Tsou, A. Westphal, E. D. Young, K. Ziegler, L. Zimmermann, and E. Zinner. 2006. 'Isotopic compositions of cometary matter returned by Stardust', *Science*, 314: 1724-28.

McKeegan, K. D., A. P. A. Kallio, V. S. Heber, G. Jarzebinski, P. H. Mao, C. D. Coath, T. Kunihiro, R. C. Wiens, J. E. Nordholt, R. W. Moses, D. B. Reisenfeld, A. J. G. Jurewicz, and D. S. Burnett. 2011. 'The Oxygen Isotopic Composition of the Sun Inferred from Captured Solar Wind', *Science*, 332: 1528-32.

McKeegan, Kevin D. 1987. 'Ion microprobe measurements of H, C, O, Mg, and Si isotopic abundances in individual interplanetary dust particles', Ph. D., Washington University.

McKeegan, Kevin D., Robert M. Walker, and Ernst Zinner. 1985. 'Ion microprobe isotopic measurements of individual interplanetary dust particles', *Geochimica et Cosmochimica Acta*, 49: 1971-87.

Messenger, S. 2002. 'Opportunities for the stratospheric collection of dust from short-period comets', *Meteoritics & Planetary Science*, 37: 1491-505.

Messenger, S., L. P. Keller, F. J. Stadermann, R. M. Walker, and E. Zinner. 2003. 'Samples of

stars beyond the solar system: Silicate grains in interplanetary dust', *Science*, 300: 105-08.

Meyer, B. S., L. R. Nittler, A. N. Nguyen, and S. Messenger. 2008. 'Nucleosynthesis and chemical evolution of oxygen.' in G. J. MacPherson, D. W. Mittlefehldt, J. H. Jones and S. B. Simon (eds.), *Oxygen in the Solar System*.

Nakamura, K, S Messenger, and LP Keller. 2005. 'TEM and NanoSIMS Study of Hydrated/Anhydrous Phase Mixed IDPs: Cometary or Asteroidal Origin?'.

Nakamura, T., T. Noguchi, A. Tsuchiyama, T. Ushikubo, N. T. Kita, J. W. Valley, M. E. Zolensky, Y. Kakazu, K. Sakamoto, E. Mashio, K. Uesugi, and T. Nakano. 2008. 'Chondrulelike objects in short-period comet 81P/Wild 2', *Science*, 321: 1664-67.

Nakamura-Messenger, K., L. P. Keller, S. J. Clemett, S. Messenger, and M. Ito. 2011. 'Nanometer-scale anatomy of entire Stardust tracks', *Meteoritics & Planetary Science*, 46: 1033-51.

Nakamura-Messenger, Keiko, Simon J Clemett, Scott Messenger, and Lindsay P Keller. 2011. 'Experimental aqueous alteration of cometary dust', *Meteoritics & Planetary Science*, 46: 843-56.

Nakashima, D., T. Ushikubo, D. J. Joswiak, D. E. Brownlee, G. Matrajt, M. K. Weisberg, M. E. Zolensky, and N. T. Kita. 2012. 'Oxygen isotopes in crystalline silicates of comet Wild 2: A comparison of oxygen isotope systematics between Wild 2 particles and chondritic materials', *Earth and Planetary Science Letters*, 357: 355-65.

Nakashima, D., T. Ushikubo, M. E. Zolensky, and N. T. Kita. 2012. 'High precision oxygen three-isotope analyses of anhydrous chondritic interplanetary dust particles', *Meteoritics & Planetary Science*, 47: 197-208.

Nesvorny, D., and P. Jenniskens. 2010. 'Cometary Origin of the Zodiacal Cloud and Antarctic

Micrometeorites', *Meteoritics & Planetary Science*, 45: A151-A51.

Ogliore, R. C., K. Nagashima, G. R. Huss, A. J. Westphal, Z. Gainsforth, and A. L. Butterworth. 2015. 'Oxygen isotopic composition of coarse- and fine-grained material from comet 81P/Wild 2', *Geochimica et Cosmochimica Acta*, 166: 74-91.

Oort, Jan Hendrik. 1950. 'The structure of the cloud of comets surrounding the Solar System and a hypothesis concerning its origin', *Bulletin of the Astronomical Institutes of the Netherlands*, 11: 91-110.

Rietmeijer, F. J. M. 1991. 'Aqueous Alteration In 5 Chondritic Porous Interplanetary Dust Particles', *Earth and Planetary Science Letters*, 102: 148-57.

———. 1996. 'CM-like interplanetary dust particles in lower stratosphere during 1989 October and 1991 June July', *Meteoritics & Planetary Science*, 31: 278-88.

Sakamoto, N., Y. Seto, S. Itoh, K. Kuramoto, K. Fujino, K. Nagashima, A. N. Krot, and H. Yurimoto. 2007. 'Remnants of the early solar system water enriched in heavy oxygen isotopes', *Science*, 317: 231-33.

Schrader, D. L., I. A. Franchi, H. C. Connolly, R. C. Greenwood, D. S. Lauretta, and J. M. Gibson. 2011. 'The formation and alteration of the Renazzo-like carbonaceous chondrites I: Implications of bulk-oxygen isotopic composition', *Geochimica et Cosmochimica Acta*, 75: 308-25.

Slodzian, G. 1980. 'Micronalayzers using secondary ion emission.' in A. Septier (ed.), *Advances in Electronics and Electron Physics* (Acad. Press).

Snead, CJ, KD McKeegan, S Messenger, and K Nakamura-Messenger. 2012. 'Mineralogy and oxygen isotope compositions of two C-rich hydrated interplanetary dust particles'.

Starkey, Natalie A., and Ian A. Franchi. 2013. 'Insight into the silicate and organic reservoirs of

the comet forming region', *Geochimica et Cosmochimica Acta*, 105: 73-91.

Takir, D., and J. P. Emery. 2012. 'Outer Main Belt asteroids: Identification and distribution of four 3-mu m spectral groups', *Icarus*, 219: 641-54.

Team, R Development Core. 2013. "R: A Language and Environment for Statistical Computing." In, edited by R Foundation for Statistical Computing. R Foundation for Statistical Computing, Vienna, Austria.

Thiemens, M. H. 1992. 'Mass-Independent Isotopic Fractionations and Their Applications', *Isotope Effects in Gas-Phase Chemistry*, 502: 138-54.

Thiemens, M. H., T. Jackson, E. C. Zipf, P. W. Erdman, and C. Vanegmond. 1995. 'Carbon-Dioxide and Oxygen-Isotope Anomalies in the Mesosphere and Stratosphere', *Science*, 270: 969-72.

Thiemens, M.H. 1996. 'Mass-independent isotopic effects in chondrites: the role of chemical processes.' in R. H. Hewins, R. H. Jones and E. R. D. Scott (eds.), *Chondrules and the protoplanetary disk* (Cambridge University Press: New York).

Thiemens, Mark H., and J. E. Heidenreich. 1983. 'The mass independent fractionation of oxygen: A novel isotope effect and its possible cosmochemical implications', *Science*, 219: 1073-75.

Thomas, K. L., G. E. Blanford, L. P. Keller, W. Klöck, and D. McKay. 1993. 'Carbon abundance and silicate mineralogy of anhydrous interplanetary dust particles', *GCA*, 57: 1551-66.

Thomas, K.L., L. P. Keller, G. E. Blandford, and D. S. Mc Kay. 1992. 'High carbon contents in IDPs : Hydrated particles from cometary sources?', *Meteoritics*, 27: 296-97.

Timmes, F. X., S. E. Woosley, and T. A. Weaver. 1995. 'Galactic Chemical Evolution - Hydrogen through Zinc', *Astrophysical Journal Supplement Series*, 98: 617-58.

Tomeoka, K., N. Tomioka, and I. Ohnishi. 2008. 'Silicate minerals and Si-O glass in comet Wild 2 samples: Transmission electron microscopy', *Meteoritics & Planetary Science*, 43: 273-84.

Trujillo, C. A., D. C. Jewitt, and J. X. Luu. 2001. 'Properties of the trans-neptunian belt: Statistics from the Canada-France-Hawaii Telescope Survey', *Astronomical Journal*, 122: 457-73.

Wang, Z. K., L. J. Ci, L. Chen, S. Nayak, P. M. Ajayan, and N. Koratkar. 2007. 'Polarity-dependent electrochemically controlled transport of water through carbon nanotube membranes', *Nano Letters*, 7: 697-702.

Weissman, P. R. 1996a. 'The Oort cloud', *Completing the Inventory of the Solar System*, 107: 265-88.

———. 1996b. 'Star passages through the Oort cloud', *Earth Moon and Planets*, 72: 25-30.

Young, E. D., and S. S. Russell. 1998. 'Oxygen reservoirs in the early solar nebula inferred from an Allende CAI', *Science*, 282: 452-55.

Yurimoto, H., and K. Kuramoto. 2004. 'Molecular cloud origin for the oxygen isotope heterogeneity in the solar system', *Science*, 305: 1763-66.

Zolensky, M. E., T. J. Zega, H. Yano, S. Wirick, A. J. Westphal, M. K. Weisberg, I. Weber, J. L. Warren, M. A. Velbel, A. Tsuchiyama, P. Tsou, A. Toppani, N. Tomioka, K. Tomeoka, N. Teslich, M. Taheri, J. Susini, R. Stroud, T. Stephan, F. J. Stadermann, C. J. Snead, S. B. Simon, A. Simionovici, T. H. See, F. Robert, F. J. M. Rietmeijer, W. Rao, M. C. Perronnet, D. A. Papanastassiou, K. Okudaira, K. Ohsumi, I. Ohnishi, K. Nakamura-Messenger, T. Nakamura, S. Mostefaoui, T. Mikouchi, A. Meibom, G. Matrajt, M. A. Marcus, H. Leroux, L. Lemelle, L. Le, A. Lanzirotti, F. Langenhorst, A. N. Krot, L. P.

Keller, A. T. Kearsley, D. Joswiak, D. Jacob, H. Ishii, R. Harvey, K. Hagiya, L. Grossman, J. N. Grossman, G. A. Graham, M. Gounelle, P. Gillet, M. J. Genge, G. Flynn, T. Ferroir, S. Fallon, D. S. Ebel, Z. R. Dai, P. Cordier, B. Clark, M. F. Chi, A. L. Butterworth, D. E. Brownlee, J. C. Bridges, S. Brennan, A. Brearley, J. P. Bradley, P. Bleuet, P. A. Bland, and R. Bastien. 2006. 'Report - Mineralogy and petrology of comet 81P/Wild 2 nucleus samples', *Science*, 314: 1735-39.

Zook, Herbert A. 2001. 'Spacecraft Measurements of the Cosmic Dust Flux.' in Bernhard Peucker-Ehrenbrink and Birger Schmitz (eds.), *Accretion of Extraterrestrial Matter Throughout Earth's History* (Springer US: Boston, MA).